Key factors in improving the synthesis and properties of visible-light activated g-C_3N_4 for photocatalytic hydrogen production and organic pollutant decomposition

Amir H. Navidpour[1], Derek Hao[2,*], Xiaowei Li[3], Donghao Li[4], Zhenguo Huang[1], John L. Zhou[1,*]

[1]Centre for Green Technology, School of Civil and Environmental Engineering, University of Technology Sydney, 15 Broadway, Ultimo, NSW 2007, Australia

[2]School of Science, RMIT University, Melbourne, VIC 3000, Australia

[3]School of Environmental and Chemical Engineering, Key Laboratory of Organic Compound Pollution Control, Ministry of Education, Shanghai University, Shanghai 200444, China

[4]Department of Chemistry, Yanbian University, Park Road 977, Yanji, 133002, Jilin Province, China

Corresponding authors:
Prof John Zhou, junliang.zhou@uts.edu.au
Dr. Derek Hao, haoqiangderek@gmail.com

Graphical abstract

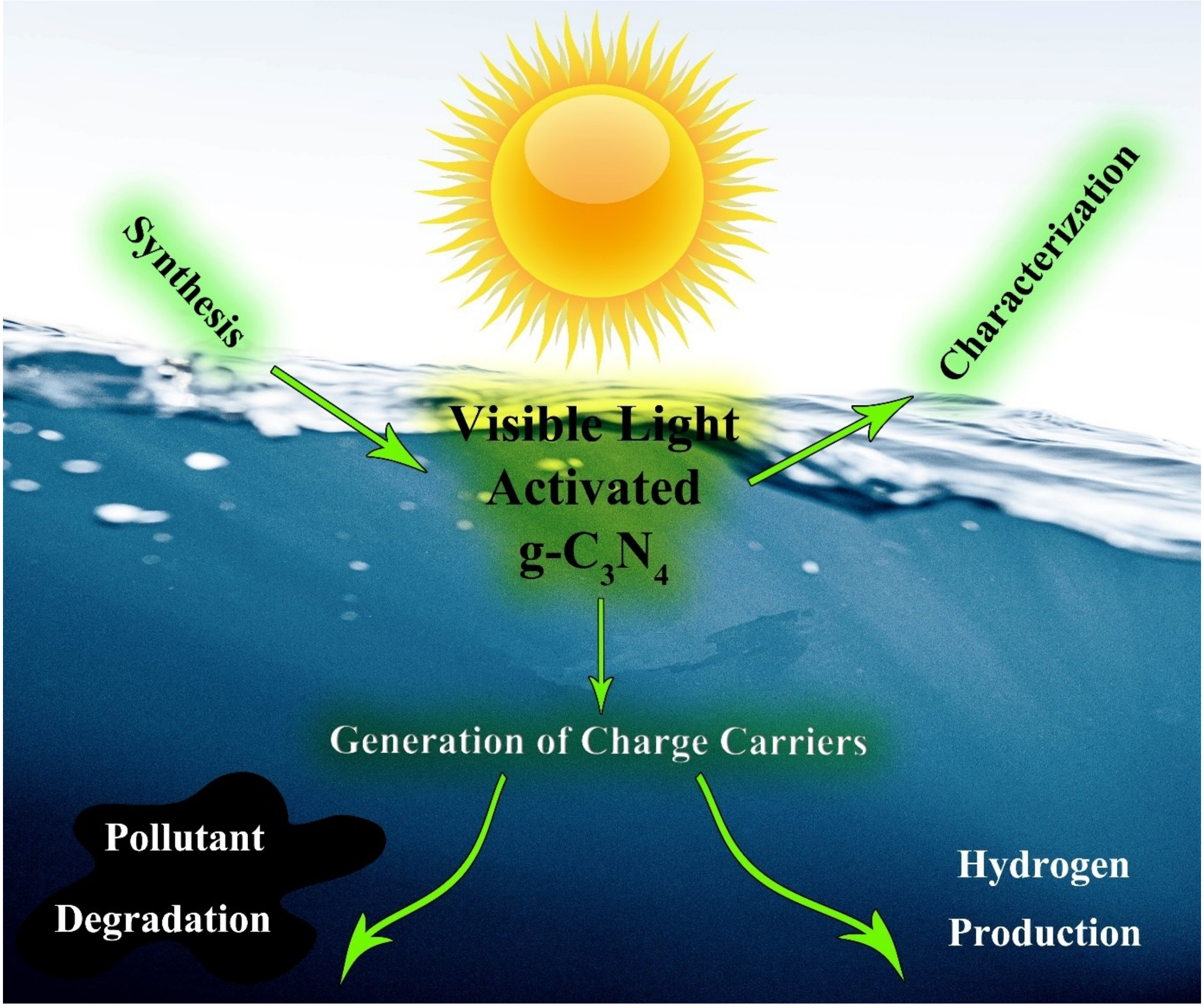

Abstract

Of current interest is visible-light activated g-C_3N_4, owing to its unique physicochemical properties for the photocatalytic H_2 production and pollutant remediation. In this research, the synthetic procedures, physicochemical properties, and major approaches to overcome the intrinsic drawbacks of g-C_3N_4 are reviewed. Of different synthesis procedures for GCN, thermal polymerization is recommended with advantages such as simplicity, economic, and high yield. Element doping, as a facile method, can modify g-C_3N_4 structure and improve its performance in the photocatalytic evolution of H_2 which is significantly increased from 208 μmol h^{-1} g^{-1} for bare g-C_3N_4 to 5128 μmol h^{-1} g^{-1} for P-doped g-C_3N_4. Ammonium salts can be effectively used for the synthesis of g-C_3N_4 nanosheets and element doping simultaneously. Vacancy defect plays an important role in the improvement of the photocatalytic activity. Compared to custom photocatalysis and electrocatalysis, photoelectrocatalysis is highly promising for pollutant decontamination due to the effective separation of charge carriers.

Keywords: Element doping; g-C_3N_4; Photocatalytic H_2 production; Photoelectrocatalysis; Pollutant remediation

1. Introduction

The generation of renewable green energy such as hydrogen as a promising alternative source of energy is of worldwide interest to support human sustainable development.[1] Photocatalytic hydrogen production, with marginal adverse effects on the environment,[2] has gained extensive attention due to its potential applications in future.[3] Thermodynamically, the overall water splitting into H_2 and O_2 is considered an uphill endothermic reaction (ΔG° = 237 kJ mol^{-1}), whereas a driving force for redox reactions is provided by sunlight irradiation in photocatalytic reactions.[4] Notably, the photogenerated holes and electrons on a semiconductor-based photocatalyst can initiate oxygen evolution reaction (OER) and hydrogen evolution reaction (HER), respectively, through the equations (1) and (2):[5]

$$2H_2O + 4h^+ \rightarrow O_2 + 4H^+ \quad (1)$$

$$2H^+ + 2e^- \rightarrow H_2 \quad (2)$$

The schematic illustration of photocatalytic water splitting is shown in Figure 1. To evaluate the respective mechanisms of OER and HER, sacrificial agents are usually used.[4] Sacrificial agents could highly affect the photocatalytic HER where methanol, sodium sulfide/sodium sulfite, and triethanolamine (TEA or TEOA) are the most frequently used sacrificial agents for oxide, sulfide, and carbon semiconductors, consecutively.[2] Notably, the photocatalytic OER or HER half-reactions (equations (1) and (2)) could proceed much easier than photocatalytic overall water splitting due to their considerably smaller ΔG than 273 kJ mol^{-1} (for overall water splitting).[4] In addition to the energy issues, water availability and water pollution are another serious problem as people living in arid regions may be forced to reduce daily water intake and water use in agriculture, reducing their domestic food production.[6] Wastewater treatment has been extensively used for the removal of organic pollutants, however, persistent organic pollutants (POPs) and emerging organic pollutants (e.g. antibiotics, endocrine disrupting chemicals) could remain in the treated effluent, due to the limited efficiency of current treatment technologies.[7, 8] The adverse effects of environmental pollution are challenging the entire world. For example, long-term exposure to antibiotic residues could support the development of antibiotic resistance genes (ARGs) which present another dimension to the pollution problem.[9]

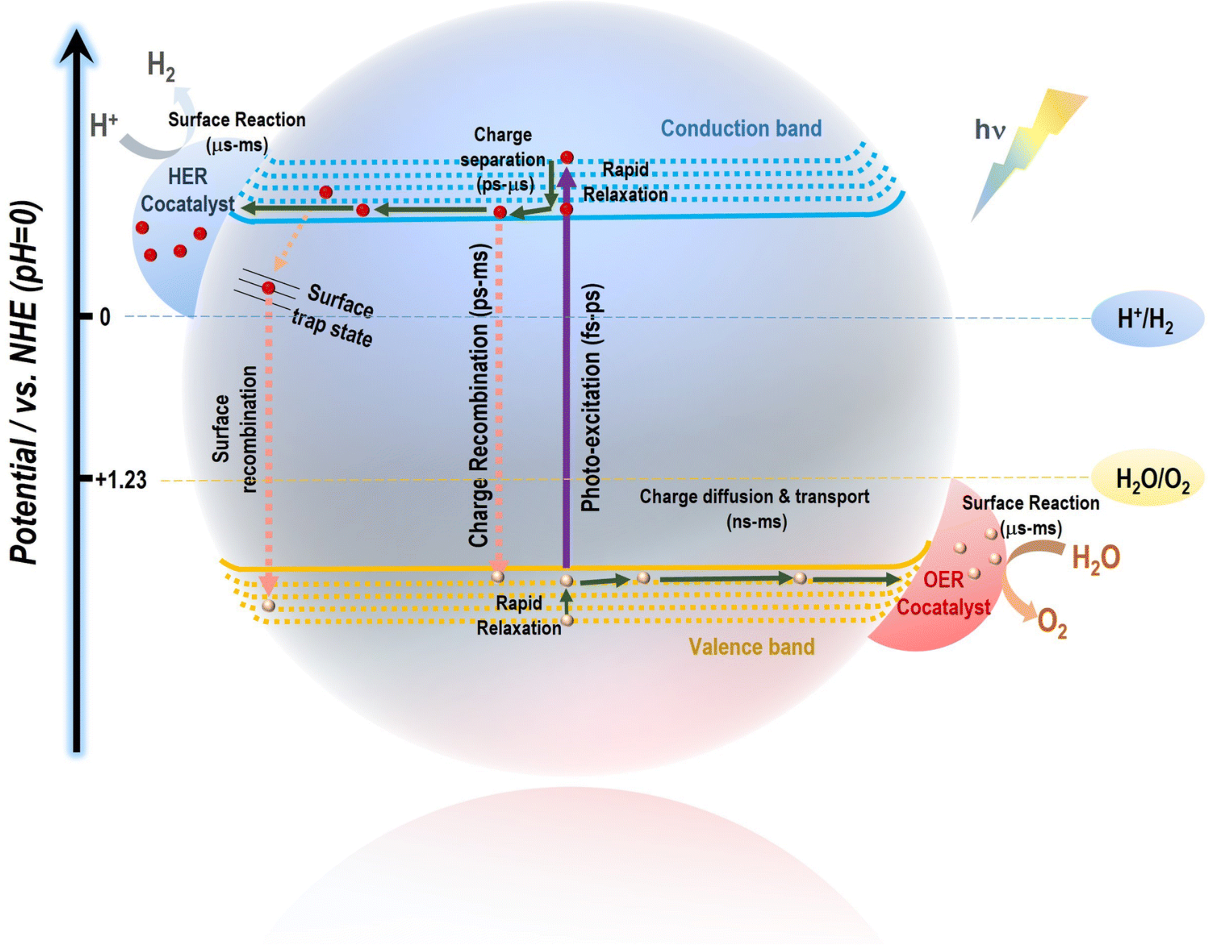

Figure 1. Schematic illustration of photocatalytic water splitting using a semiconductor-based material. Reproduced with permission from Ref. [10] Copyright 2022 The Royal Society of Chemistry (https://pubs.rsc.org/en/Content/ArticleLanding/2022/CS/D2CS90098J).

Different methods have been used for the removal of organic pollutants including membrane processes (e.g. nanofiltration, forward osmosis, reverse osmosis), sonochemical degradation, advanced oxidation processes (AOPs), adsorption, micellar-enhanced ultrafiltration (MEUF), electrochemical oxidation (EO), precipitation, coagulation, biodegradation, and ion exchange. Adsorption, coagulation, flocculation, and membrane processes typically concentrate and transfer pollutants from one phase to another.[11] AOPs include various techniques such as ozonation, persulfate-based oxidation, electrolysis, photolysis, sonolysis Fenton-based processes, and photocatalysis.[12, 13] Hydroxyl radicals ($^{\bullet}OH$) are extremely highly reactive radicals which can be generated by primary oxidants (such as ozone or hydrogen peroxide), and are capable of oxidizing various organic pollutants.[14] Notably, they could attack organic pollutants through four general mechanisms: transfer of electrons, abstraction of hydrogens, radical combination, and radical addition.[15] AOPs are universal technologies which can be used for degradation of organic pollutants (even complete mineralization).[16] However, it is also of high importance to consider the toxicity of degradation by-products or intermediates, some of which could be even more toxic than the original pollutant.[17] Overall, semiconductor photocatalysis relies on four steps as follows:[18]

a) Absorption of photons to create charge carriers,

b) Separation of charge carriers,

c) Transfer of charge carriers to the surface of photocatalyst, and

d) Redox reactions initiated by charge carriers.

Surface reactions could happen only if the oxidation potentials are more negative than the potential of valence band (VB) or the reduction potentials are more positive than the potential of conduction band (CB) in oxidation and reduction processes, respectively.[19] Although photocatalysis is well-known as an efficient process for water and wastewater treatment, several key points should be considered to facilitate its practical applications. Importantly, semiconductor particles cannot be easily recycled after wastewater treatment. Another key point is that 3-6% of the solar irradiation is in the ultraviolet spectrum;[20] yet TiO_2, the most common semiconductor material, has negligible visible-light adsorption.[18] TiO_2,[13, 21] ZnO,[22] SnO_2,[23] and Zn_2SnO_4[24, 25] are among metal-based semiconductors used for photocatalytic applications, but they all have wide band gap energies (>3.0 eV), restricting their visible light harvest.

Taking advantages of their lower band gap energies than TiO_2, ZnO, and SnO_2, some other metal-based semiconductors such as α-Fe_2O_3,[26] Ag_3PO_4,[27] CdS,[28] Ag_2S,[29] $BiVO_4$,[30] MoS_2,[31] $ZnFe_2O_4$[32, 33] and Ag_3VO_4[34] have been used for photocatalytic applications under visible light exposure. However, there are still some drawbacks for α-Fe_2O_3 (low diffusion length of holes, high recombination rate of charge carriers, and poor conductivity),[35] Ag_3PO_4 (low photostability and fast recombination of charge carries)[27], MoS_2 (high recombination rate of charge carriers, poor conductivity, and low stability),[31] CdS (photocorrosion in pure water and fast recombination of charge carries),[36] Ag_2S (fast recombination of charge carries),[37] $ZnFe_2O_4$ (leaching, agglomeration, fast recombination of charge carries, and high photocorrosion rate),[38] $BiVO_4$ (low photon efficiency and poor electron mobility),[39] and Ag_3VO_4 (instability and fast recombination of charge carries).[34] Considering the energy conversion domain, using stable and cost-effective semiconductors with suitable band gap energies for practical photocatalytic water splitting is a major difficulty.[40, 41] Metal-free photocatalysts are substantial alternatives to metal-based semiconducting materials. Some metal-free photocatalysts have shown a superior photocatalytic (PC) performance than metal-based counterparts.[42] Owing to its optical, structural, and electronic properties, graphene is one of the most important carbon-based materials.[43] Graphitic carbon nitride, abbreviated as GCN or g-C_3N_4, is another burgeoning and promising carbon-based metal-free material owing to its unique advantages including facile synthesis using inexpensive precursors, high physicochemical stability, suitable band gap energy, abundance, and eco-friendly nature.[44, 45] As a polymeric material, it takes advantage of its controllable morphology, size, pore structure, thickness, and easy synthetic procedure.[46]

Compared with TiO_2 and ZnO, g-C_3N_4 possesses a more negative CB level that makes it a suitable candidate for reduction reactions. Regarding the overall photocatalytic water splitting, the bottom of the CB level and the top of the VB level of the used semiconductor must be respectively negative and positive enough to facilitate reduction and oxidation reactions.[5] Overall, with a low band gap energy of 2.7 eV, GCN is considered a promising photocatalytic material for development of solar energy.[46] Although individual photocatalysts generally provide weak photocatalytic activity for H_2 generation under visible light irradiation, a combination of GCN with a metal co-catalyst and a sacrificial agent (hole scavenger) could provide high photoactivity.[47] In addition to photocatalytic water splitting, GCN has been widely used for photocatalytic CO_2 reduction.[48] Apart from its potential applications for solar fuel production via photocatalytic water splitting and CO_2 reduction,[49] GCN-driven “gold rush” is considered a novel and hotspot field which has received wide attention in environmental remediation.[50] Up to now, GCN has been used for the degradation of various types of organic pollutants from different industries such as textile, plastic, pharmaceutical, and agriculture (pesticides and insecticides), as summarized in Table 1.

Table 1. Applications of g-C_3N_4 composites in the photocatalytic degradation of organic pollutants under visible light.

Application	**Photocatalyst**	**Pollutant**	**Illumination source**	**Photocatalytic activity**	**Reference**
Textile	g-C_3N_4/$CuWO_4$ nanocomposite	Methylene blue (MB)	250 W High pressure mercury lamp	~ 97% (t = 3 h)	[51]
Textile	g-C_3N_4/Bi_2WO_6 composite	Methyl orange (MO)	500 W Xenon lamp	~ 100% (t = 3 h)	[52]
Textile	g-C_3N_4	Rhodamine B (RhB)	300 W Xenon lamp	~ 68% (t = 50 min)	[53]
Plastic	Pd/g-C_3N_4	Bisphenol A	350 W Xenon lamp	~ 100% (t = 6 h)	[54]
Plastic	g-C_3N_4/$BiVO_4$ heterostructure	Phenol	500 W Halogen lamp	~ 50.2% (t = 2 h)	[55]
Pharmaceutical	g-C_3N_4 (1.5 wt%)/Hap composite	Tetracycline (TC)	300 W Xenon arc lamp	~ 100% (t = 15 min)	[56]
Pharmaceutical	Ag/TiO_2/g-C_3N_4 nanocomposite	Amoxicillin	300 W Xenon lamp	$k = 0.0614\ min^{-1}$	[57]
Agriculture	Cu-doped ZnO/ g-C_3N_4	Atrazine	Visible radiation (400-700 nm)	~ 90% (t = 3 h)	[58]
Agriculture	g-C_3N_4/N-doped CeO_2 composite	Diuron	1500 W Xenon lamp	~ 46% (t = 2 h)	[59]

Carbon nitrides mainly include carbon and nitrogen and can be obtained from carbon materials (through substitution of C atoms by N atoms). GCN is a polymeric metal-free n-type semiconductor material that has received attention owing to its unique structural, electrical, physicochemical, and optical properties. Notably, GCN is the most stable polymorph of carbon nitrides in the ambient atmosphere.[60, 61] Overall, there are seven allotropes of C_3N_4 including alpha, beta, cubic, pseudocubic, g-h-triazine, g-o-triazine, and g-h-heptazine with space groups of $P3_1c$ (159), P3 (143), I-43d (220), P–42m (111), P-6m2 (187), P2mm (25), and $Cmc2_1$ (36), respectively.[62] GCN has a stacked two-dimensional (2D) layered structure where single layers of nitrogen heteroatom-substituted nanosheets of graphite are bound only by weak van der Waals forces. These single layers of nitrogen heteroatom-substituted nanosheets of graphite are formed by sp^2 hybridization of nitrogen and carbon atoms.[19] Real g-C_3N_4 possesses a tiny amount of hydrogen which presents as primary/secondary amine groups on the terminating edges.[61] The probable multiple surface functionalities on g-C_3N_4 are illustrated in Figure 2(a).

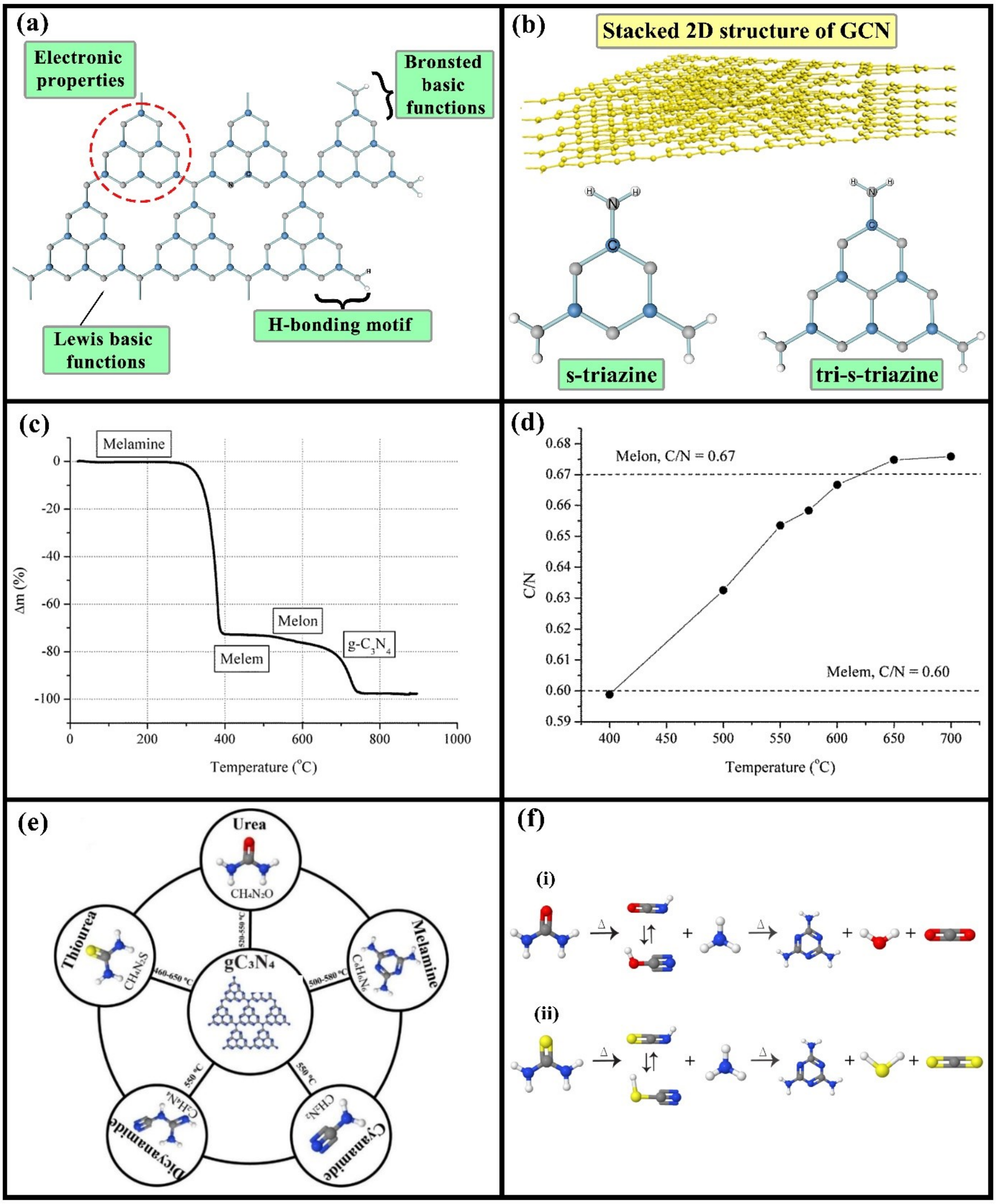

Figure 2. (a) Probable multiple functionalities of g-C_3N_4. Redrawn from Ref. [60] Copyright 2008 The Royal Society of Chemistry (https://pubs.rsc.org/en/content/articlelanding/2008/jm/b800274f). (b) The stacked 2D structure of g-C_3N_4 and its primary building blocks. Redrawn from Ref. [19] Copyright 2017 Elsevier. (c) Thermogravimetric curve of annealing of melamine. Reprinted with permission

from Ref. [63] Copyright 2017 Elsevier. (d) Molar ratios of C/N for condensation of melamine products at different temperatures from 400 °C to 700 °C. Reprinted with permission from Ref. [63] Copyright 2017 Elsevier. (e) Common precursors and corresponding calcination temperatures used to synthesize GCN (hydrogen, carbon, oxygen, nitrogen, and sulfur atoms are represented by white, gray, red, blue, and yellow balls). Reprinted with permission from Ref. [64] Copyright 2022 MDPI. This article is an open access article distributed under the terms and conditions of the Creative Commons Attribution (CC BY) license (https://creativecommons.org/licenses/by/4.0/). (f) The conversion mechanism of (i) urea and (ii) thiourea to melamine at high temperatures (hydrogen, carbon, oxygen, nitrogen, and sulfur atoms are represented by white, gray, red, blue, and yellow balls). Reprinted with permission from Ref. [64] Copyright 2022 MDPI. This article is an open access article distributed under the terms and conditions of the Creative Commons Attribution (CC BY) license (https://creativecommons.org/licenses/by/4.0/).

The incomplete condensation of precursors could result in the existence of hydrogen and creation of some surface defects including the Lewis-base character which can promote the relocalization of electrons on the surface, consequently improving the catalytic activity.[61] GCN, which could take advantages of the availability of hydrogen and nitrogen, has unique electron-rich properties, basic surface functionalities, good electronic band structures, and high thermal/hydrothermal (physicochemical) stability.[61, 65] Its particular surface properties, induced by nitrogen, enables g-C_3N_4 as more promising than other carbon nanomaterials.[65] Generally, two different condensation states (i.e. building blocks) are considered as its primary building blocks: triazine (ring of C_3N_3) with periodic arrays of single carbon vacancies and tri-s-triazine rings (heptazine: triring of C_6N_7) with larger periodic vacancies in the lattice. Heptazine rings are connected through planar tertiary amino groups.[19] The stacked 2D structure of g-C_3N_4 and its primary building blocks are shown in Figure 2(b). Tri-s-triazine is considered the most accepted structural unit under ambient conditions[66, 67] since tri-s-triazine-based g-C_3N_4 is energetically more stable than triazine-based g-C_3N_4.[19] The high condensation and tri-s-triazine ring structure are responsible for the high stability of g-C_3N_4 concerning thermal and chemical attacks.[68]

This study aims to critically review the principles and advances in the synthesis of g-C_3N_4, and to suggest potential approaches to improve its photocatalytic activity. In addition, photoelectrocatalysis is reviewed as a more promising technology than photocatalysis for the decontamination of organic pollutants over GCN-based materials.

2. Methods of g-C_3N_4 synthesis

Various methods including chemical vapor deposition (CVD), physical vapor deposition (PVD), solid-state reaction, thermal annealing/condensation, sonochemical, and solvothermal have been used for the synthesis of GCN. Thermal condensation suffers from its low yield (approximately 6%) that originates from the higher polymerization temperature of g-C_3N_4 than the sublimation point of reagents, resulting in their loss prior to the occurrence of reaction.[46] However, its simplicity, absence of impurities (during synthesis), low cost, and convenience[65] have introduced this method as the most efficient and widely-used for the synthesis of GCN.[46, 63] Thus, this method is discussed in detail.

2.1. Thermal condensation

Reactive nitrogen-rich and oxygen-free compounds that possess pre-bonded C-N core structures (such as heptazine and triazine derivatives) are the most common precursors in chemical routs.[61] g-C_3N_4 catalysts are usually produced by thermal condensation of organic compounds (such as urea, thiourea, cyanamide, dicyanamide, and melamine) as the most attractive method owing to the use of earth-abundant and cheap precursors and the simplicity of synthetic process.[69] Thermal polymerization synthesis of GCN includes poly-addition and poly-condensation.[70] Wang et al. synthesized GCN using cyanamide as the precursor,[71] although it should be noted that cyanamide is explosive and expensive. Generally, the synthesis of g-C_3N_4 using cyanamide and dicyanamide (as its derivative) is hard to operate and expensive.[61] It has been shown that using precursors containing other elements, in addition to H, N and C, could facilitate the process of thermal condensation and results in the structural alterations.[72] To overcome these obstacles, different guanidine compounds such as guanidine carbonate,[73] guanidine thiocyanate,[74] and guanidine hydrochloride (as an inexpensive, widely available, and environmentally-friendly precursor)[72] have been used for the synthesis of g-C_3N_4. However, GCN synthesized by melamine showed a higher photocatalytic activity than that synthesized by guanidine carbonate for the degradation of MO.[73] The presence of oxygen atoms in urea could facilitate the condensation of GCN and boost its stability.[64] The thermogravimetric curve of annealing of melamine and the molar ratio of C/N for condensation of melamine products at different temperatures are shown in Figures 2(c) and 2(d), respectively. As shown in Figure 2(c), the first and the highest reduction of mass, approximately 70%, occurs between 280 and 400 °C. This remarkable decrease of mass was attributed to the sublimation and condensation of melamine which is accompanied by the elimination of ammonium and formation of melem ($C_6N_{10}H_6$) as a by-product. Noteworthy, melam could be formed at temperatures above 300 °C, typically 400-500 °C. At temperatures higher than 500 °C, melon ($C_6N_9H_3$) could be produced due to the polymerization of melem. The polymerization of melon to the GCN planar structure could occur at temperatures higher than 600 °C. However, GCN is unstable at high temperatures, resulting in the formation of some volatile decomposition products.[63] Common precursors and corresponding calcination temperatures used to synthesize GCN are shown in Figure 2(e). As evident, melamine could be generated from either thiourea, urea, dicyanamide or cyanamide, where its conversion to melem and melon could lead to the production of g-C_3N_4 by polymerization of tri-s-triazine ring structure.[64] The conversion mechanism of thiourea and urea into melamine is shown schematically in Figure 2(f).

2.1.1. Effect of different precursors on photocatalysis

Xin et al. synthesized g-C_3N_4 from the pyrolysis of cyanamide, melamine, and dicyandiamide precursors for the photocatalytic degradation of MB under visible light irradiation. Using different precursors did not significantly affect the morphology and texture of GCN in their research. GCN synthesized by dicyandiamide showed the highest photocatalytic efficiency owing to its high C/N ratio (0.685), good crystal structure, and moderate degree of condensation. They concluded that increasing C/N ratio and degree of condensation could improve the photocatalytic activity.[75] Zhang et al. synthesized GCN by the pyrolysis of melamine, dicyandiamide, urea and thiourea precursors (550 °C, 3 h, and heating rate of 10 °C/min) for the photocatalytic removal of NO under visible-light irradiation. The band gap energies of g-C_3N_4 were 2.51, 2.56, 2.58, and 2.88 eV by using thiourea, melamine, dicyandiamide, and urea, respectively. The minimum and maximum photo-absorption values in the visible-light region were obtained by g-C_3N_4 synthesized by urea and thiourea, respectively.[76] The preparation method of g-C_3N_4 affects its photo-absorption ability. Thus, the type of precursor and condensation temperature that result in the formation of different local structures, defects, and packing (degree of condensation) are among factors which affect the photo-absorption ability of g-C_3N_4.[68] Notably, due to its aromatic structure, melamine itself has a strong absorption edge and could significantly absorb UV irradiation.[63] The g-C_3N_4 synthesized by thiourea, dicyandiamide, melamine and urea achieved BET surface areas of 23, 18, 14, and 153 m^2/g; pore volumes of 0.14, 0.09, 0.06, and 0.40 cm^3/g; and apparent rate constants of 0.310, 0.079, 0.298, and 0.384 min^{-1} for the photocatalytic degradation of NO respectively. The results clarify the key role of oxygen and sulfur heteroatoms in enlarging the pore volume and enhancing the specific surface area. Notably, they all showed very similar thermal stabilities (<550 °C, <563 °C, <575 °C, and <530 °C, consecutively).[76] Although the synthetic efficiency (yield) of GCN using different precursors is remarkably different, it has rarely been reported. Alwin et al. have measured the yield of GCN synthesized by different precursors at different annealing conditions. Notably, both annealing conditions and type of precursors significantly affected the yield of GCN though at varying degrees. It should be noted that increasing the temperature, time, and rate of annealing decreased the yield of GCN. However, the effect of annealing rate was not considerable. Furthermore, the yields of GCN using melamine, thiourea, and dicyanamide precursors were 26%, 11%, and 53%, respectively, signifying the moderate production efficiency of GCN using melamine.[77] It should be noted that the yield of GCN by using urea is much lower than that by using melamine[78], dicyanamide,[79] and guanidine hydrochloride.[79]

The high content of mesopores and micropores in GCN synthesized using urea and thiourea was responsible for the formation of interconnected porous networks. Although the thermal stability of g-C_3N_4 synthesized by different precursors did not vary significantly, the highest and the lowest amount were attributed by using melamine and urea, respectively. Notably, different thermal stability is attributed to different packing between the layers and/or different degree of condensation during the polymerization process. Although using urea resulted in the production of g-C_3N_4 with the lowest photo-absorption ability, it yielded the highest photocatalytic activity attributed to the large pore volume and high specific surface area. It was concluded that the photocatalytic activity of g-C_3N_4 strongly depends on its specific surface area, degree of condensation, pore volume, and band gap energy.[76]

The higher the order of condensation, the stronger the conjugative effect is observed as a result of the formation of defects in packing and local structures.[80] Notably, most of active materials are slightly disordered, which means that grain boundaries, structural defects, stacking defects, and surface termination are inherent features of catalysts.[68] Wu et al. suggested that the formation of defect-free GCN is inevitable due to the various intermediates evolved during synthesis (such as cyanuric acid, ammelide, biuret, and ammeline). Although some intermediates could improve the separation/transfer of charge carries, others may serve as recombination centers of photo-induced e^-/h^+ pairs.[81] It has been shown that urea could result in the formation of thin crinkly paper-folded sheets of g-C_3N_4, while thiourea could result in the formation of thick crinkly paper-folded sheets of g-C_3N_4.[80] Owing to their excessive oxygen and sulfur contents that result in the formation of some gases (including H_2S, CO_2, NH_3, and H_2O) during the polymerization process, favoring the formation of porous structures and expansion of packing layers, both urea and thiourea could be effectively used to synthesize GCN with high specific surface area and large pore volume.[76, 82] Noteworthy, NH_3 and CO_2 gases could evolve during the thermal treatment process at low temperatures (< 200 °C) and high temperatures, respectively.[65] The production of gas bubbles during calcination might be considered as the main reason for the large surface area of g-C_3N_4 synthesized by thiourea. Owing to this feature, thiourea has been used as the bubble template for the synthesis of nanoporous g-C_3N_4 by dicyandiamide-thiourea mixtures.[83]

2.1.2. Effect of synthesis temperature

Mo et al. synthesized g-C_3N_4 by thermal condensation process (heating rate of 2 °C min^{-1}, 2 h) using melamine as the precursor and evaluated the effect of different temperatures (450, 500, 550, 600, and 650 °C) on the photocatalytic degradation of MB under visible light irradiation. The XRD patterns of GCN synthesized at different temperatures are shown in Figure 3(a), clarifying the formation of g-C_3N_4 at temperatures higher than 500 °C. Notably, g-C_3N_4 was completely decomposed at 700 °C. The additional peaks at 450 °C are attributed to the melem derivatives (as a result of the low polycondensation of intermediate melamine).[84]

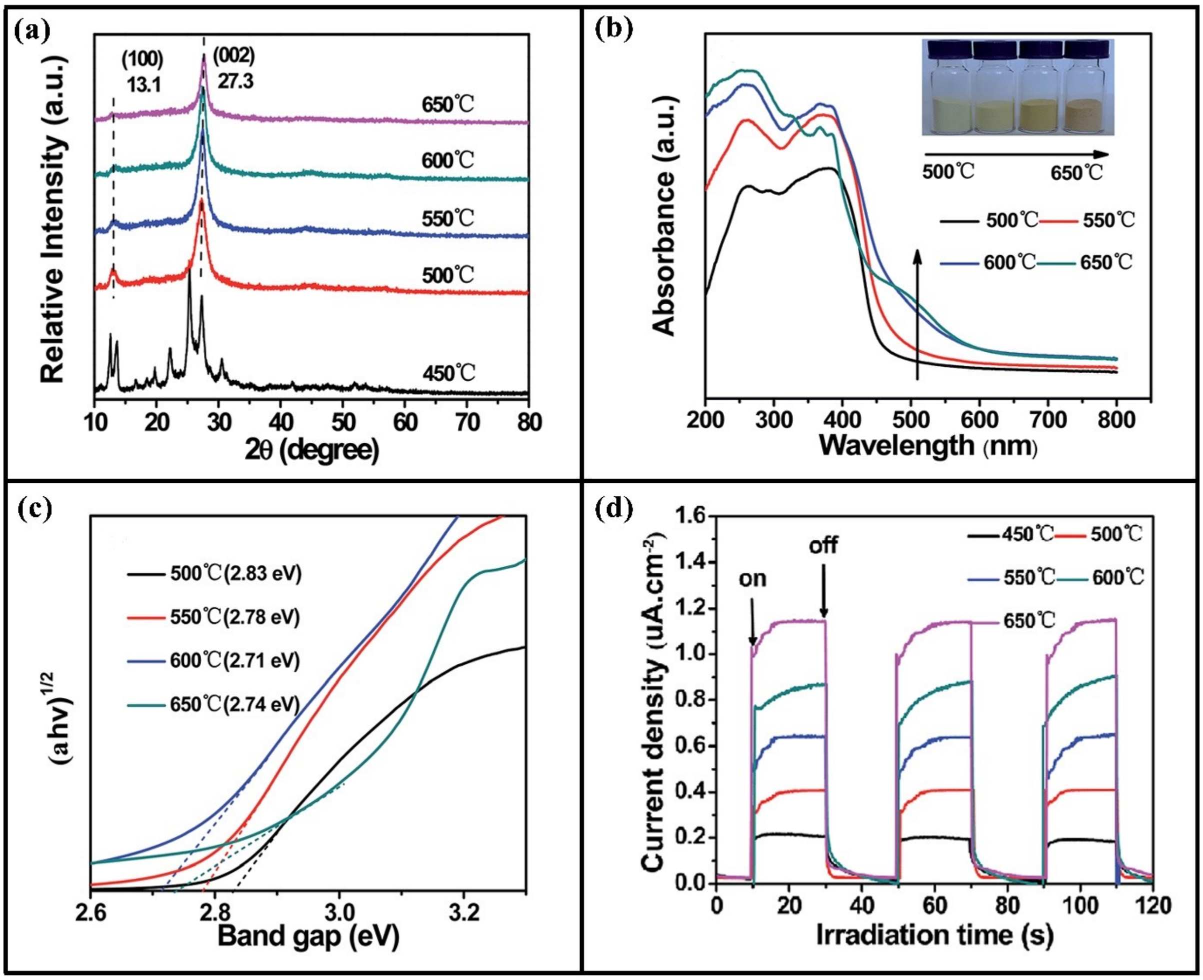

Figure 3. (a) XRD pattern of GCN samples produced at 500, 550, 600, and 650 °C. Reproduced with permission from Ref. [84] Copyright 2015 The Royal Society of Chemistry (https://pubs.rsc.org/en/content/articlelanding/2015/ra/c5ra19586a). (b) Photo-absorption ability of GCN samples produced at 500, 550, 600, and 650 °C. Reproduced with permission from Ref. [84] Copyright 2015 The Royal Society of Chemistry (https://pubs.rsc.org/en/content/articlelanding/2015/ra/c5ra19586a). (c) Band gap energy of GCN samples produced at 500, 550, 600, and 650 °C. Reproduced with permission from Ref. [84] Copyright 2015 The Royal Society of Chemistry

(https://pubs.rsc.org/en/content/articlelanding/2015/ra/c5ra19586a). (d) Photocurrent response of GCN samples produced at 500, 550, 600, and 650 °C. Reproduced with permission from Ref. [84] Copyright 2015 The Royal Society of Chemistry (https://pubs.rsc.org/en/content/articlelanding/2015/ra/c5ra19586a).

Although a lumpy morphology was observed for g-C_3N_4 synthesized at 500 °C, it became slacking by increasing the temperature, gradually resulting in the increase of specific surface area. Noteworthy, few pores were developed on the surface at 600 °C, and many pores were fused by increasing the temperature up to 650 °C. BET results also confirmed the higher specific surface area of g-C_3N_4 (6.6 times) synthesized at 650 °C than that synthesized at 500 °C. The photo-absorption ability of g-C_3N_4 synthesized at 500, 550, 600, and 650 °C is shown in Figure 3(b). Increasing the temperature from 500 to 650 °C resulted in the enhancement of absorption in the visible-light region. This redshift could be caused by the enhancement of π-plane conjugation degree and/or polymerization degree, significantly affecting the visible-light absorption.[84] The same trend was also reported by Praus et al. for the condensation of melamine products at different temperatures from 400 °C to 700 °C,[63] and Yan et al. for the condensation of melamine products at 500, 520, 550, and 580 °C.[85] The band gap energies of GCN synthesized at different temperatures are shown in Figure 3(c). Increasing the calcination temperature from 500 to 550 and 600 °C resulted in the reduction of band gap energy from 2.83 to 2.78, and 2.71 eV, respectively. Further increase of the calcination temperature up to 650 °C led to the increase of band gap energy dedicated to the quantum confinement effect due to the formation of a fluffier structure than that obtained at 600 °C. Notably, the photoluminescence (PL) intensity of GCN samples deceased by increasing the temperature where the lowest recombination rate of photo-generated e^-/h^+ pairs was achieved at 650 °C.[84] The same trend was also reported by Praus et al. for the condensation of melamine products at different temperatures from 400 °C to 700 °C.[63] The transient photocurrent response of g-C_3N_4 samples synthesized at 500, 550, 600, and 650 °C is compared in Figure 3(d), where the photocurrent response increased by increasing the temperature which was in good agreement with the results obtained from PL spectra. In summary, increasing the calcination temperature could improve both separation and transfer of photo-generated e^-/h^- pairs.[84]

Yousefzadeh et al. concluded that increasing the calcination temperature could enhance C/N molar ratio,[86] which was also suggested by Yan et al. for the condensation of melamine products at 500, 520, 550, and 580 °C.[85] Although the stoichiometric ratio of C/N for g-C_3N_4 is 0.75, the highest obtained ratio of C/N was 0.71 (at 650 °C). This mismatch accompanied by the presence of hydrogen indicates the incomplete condensation of melamine and existence of some amino groups in the formed melons (even at high temperatures).[86] Notably, elemental analysis confirmed the presence of hydrogen in all melamine condensation products at different temperatures from 400 °C to 700 °C (Table 2).

Table 2. Elemental analysis and empirical composition of g-$C_xN_yH_z$. Reprinted with permission from Ref. [63] Copyright 2017 Elsevier.

Temperature (°C)	**C (wt. %)**	**N (wt. %)**	**H (wt. %)**	**x**	**y**	**z**
400	33.0	64.3	2.7	5.5	9.2	5.4
450	34.5	63.5	2.0	5.7	9.1	3.9
550	35.4	63.1	1.5	5.9	9.0	2.9
575	35.6	63.0	1.4	5.9	9.0	2.9
600	35.9	62.8	1.3	6.0	9.0	2.5
650	36.2	62.6	1.1	6.0	8.9	2.2
700	36.3	62.6	1.1	6.0	8.9	2.2

Melem could be formed at a temperature of 400 °C. Deamination could be responsible for the decrease of hydrogen content at temperatures of 450 to 500 °C, resulting in the formation of a mixture of melon and melem. Melon is the main component of the melamine condensation in the range of 550 to 575 °C. Further decrease of hydrogen at higher temperatures could be devoted to the formation of polymerized melon and deamination. The high content of hydrogen signifies the formation of melon-like $C_xN_yH_z$ sheets, with $–NH_2$ and –NH groups, instead of C_3N_4 sheets. The molar ratios of C/N for condensation of melamine products at different temperatures from 400 °C to 700 °C are shown in Figure 2(d). Notably, the theoretical molar ratios of C/N for melon, melem, and melam are 0.67, 0.60, and 0.54, respectively. The theoretical molar ratio of C/N for g-C_3N_4 is 0.75 that was much higher than the maximum value of C/N molar ratio for condensation of melamine products at different temperatures from 400 °C to 700 °C (as shown in Figure 2(d)), clarifying the incomplete condensation of amino groups of melon. Overall, the formation of g-$C_3N_{4.5}H$ or $C_6N_9H_2$ is more probable than the formation of g-C_3N_4 (even at high temperatures).[63]

3. Different morphologies of g-C_3N_4

3.1. Bulk g-C_3N_4

As previously discussed, bulk g-C_3N_4 can be easily produced by thermal condensation of different precursors (e.g. melamine, urea, thiourea, dicyandiamide, and cyanamide) between 400 and 600 °C. Overall, urea is considered an excellent precursor for the synthesis of flaky GCN, providing high porosity and specific surface area. In general, the less the heating rate, the higher is the porosity of g-C_3N_4. It has been shown that crystallinity and specific surface area could enhance, marginally, by increasing the annealing temperature.[65]

3.2. Three-dimensional g-C_3N_4 nanostructures

Three dimensional (3D) nanostructures are usually produced by nanoscale building blocks, and have received remarkable attention due to their unique properties (a combination of straightforward molecular transport and high surface area).[65] Recently, Yuan et al. synthesized 3D porous thermally exfoliated g-C_3N_4 nanosheets for the photocatalytic degradation of organic dyes. To prepare 3D porous g-C_3N_4, the as-synthesized g-C_3N_4 has been mixed and stirred with concentrated H_2SO_4 for its intercalation. After freeze drying and calcination, the light-yellow 3D porous g-C_3N_4 has formed. The formation of such a nanostructure significantly increased the specific surface area from 12.0 (for bulk GCN) to 54.3 m^2/g (for 3D-porous GCN) due to the porousification properties of H_2SO_4. The photoluminescence spectrum of 3D-porous g-C_3N_4 showed a drastic reduction of the emission intensity compared with that of bulk g-C_3N_4 that clarifies the promising potential of 3D structures for photocatalytic purposes (as confirmed by the photocatalytic degradation of RhB).[87]

3.3. Two-dimensional g-C_3N_4 nanostructures

As stated previously, GCN has a graphitic layer structure (the same as graphene) with weak van der Waals interactions between its layers.[88] In general, the host layers of the layered materials, including g-C_3N_4, are composed of energetic ionic bonds and/or strong covalent bonds stacked with each other by electrostatic force with interlayer oppositely charged ions and/or weak van der Waals force, providing the possibility of using various chemical and physical processes to ruin such weak interlayer interactions for fabrication of sole sheets with a few or single host layers called nanosheets. An important tip to synthesize g-C_3N_4 nanosheets is that significantly weakening the interlayer van der Waals interactions should coincide with maintaining the hydrogen bonding host layers.[89, 90] Overall, there are two major strategies to produce 2D GCN nanosheets including top-down and bottom-up approaches.[65] Notably, liquid exfoliation (using ultrasonication), high-shear mixing and ball milling, chemical exfoliation, thermal oxidation exfoliation, and gas bubble templating are major methods used in the top-down category.

3.3.1. Liquid exfoliation

Liquid-Phase Exfoliation (LPE) is one of the most straightforward and effective methods to weaken the van der Waals interactions.[91] Two major methods have been used for exfoliation of 2D materials including cavitation, which occurs in sonication, and shear forces employed in both high-shear mixing and micro fluidization (under high shear rate).[92] The ultrasound-assisted method has been widely used for exfoliation of various layered materials such as MoS_2,[93] $MoSe_2$,[94] BN,[95] WS_2,[96] graphene,[97] and g-C_3N_4.[41, 90, 98] In this process, the sonication power that generates cavitation bubbles induces chemical and/or physical changes in the layered material. Rarefactions and compressions, originated from propagation of the ultrasonic waves through the medium, exert low-pressure and high-pressure to pull and push molecules. During rarefaction, formation and growing of microbubbles occurs. Their collapse, followed by reaching to an unstable state, could generate strong shockwaves (with high temperature, pressure, and speed) which produce normal and shear forces on 2D materials[90, 92]. It has been stated that minimizing the energy of exfoliation can maximize the concentration of dispersed particles.[99] Thus, the solvent plays an important role in the ultrasonic exfoliation method. Noteworthy, similar surface energy of the layered material and the solvent is more favorable.[90] Zhang et al. concluded that ultrathin g-C_3N_4 nanosheets can be easily produced by a green route from liquid exfoliation of bulk g-C_3N_4 in water.[89] Owing to the presence of NH_x groups in the structure of g-C_3N_4, originated from the polycondensation of precursors containing nitrogen and carbon, the interlayer block of GCN could be easily swelled and/or intercalated by polar solvents including ethanol, methanol, water, formamide, and DMF (*N,N*-dimethylformamide). Notably, water exhibited the highest efficiency owing to its highest polarity (among these polar solvents) and appropriate surface energy.[90] In another research, Zhang et al. dispersed ultrathin negatively charged g-C_3N_4 nanosheets (with a zeta potential of around -30.3 mV) in water with the concentration of around 0.15 mg mL^{-1}.[89] Hernandez et al. generated graphene using liquid exfoliation of graphite. High exfoliation efficiency could be provided by minimizing the enthalpy of mixing which depends on the balance of solvent and graphene surface energies. The enthalpy of mixing (per unit volume) could be calculated by equation (3):[100]

$$\frac{\Delta H_{mix}}{V_{mix}} \approx \frac{2}{T_{flake}} (\delta_G - \delta_{sol})^2 \emptyset \qquad (3)$$

where δ_i is the square root of surface energy, $\emptyset$ is the volume fraction of graphene, ΔH_{mix} is the enthalpy of mixing, and T_{flake} is the thickness of a graphene sheet. The energy (per unit area) spent on peeling two flakes apart by overwhelming the van der Waals forces is considered the surface energy of graphite. Hence, the minimal enthalpy of mixing could be achieved by using solvents whose surface energies match graphene. It has been proposed that efficient solvents could be characterized by surface tensions in the range of 40-50 mJ m^{-2} (while the surface energy of graphite is ~70-80 mJ m^{-2}).[100] Notably, equation (3) has also been used by Dong et al.[90] and Zhang et al.[89], suggesting water as an appropriate solvent for the liquid exfoliation of GCN. Yang et al. dispersed GCN nanosheets in different solvents including isopropanol (IPA), N-methyl-pyrrolidone (NMP), water, ethanol, and acetone. Notably, IPA and NMP exhibited excellent potentials (even better than water) to disperse g-C_3N_4 nanosheets and to exfoliate bulk GCN due to their appropriate surface energy of around 40 mJ m^{-2}. The results showed that increasing the sonication time could lead to the formation of thinner nanosheets. Compared with NMP, IPA could take advantages of its lower raw material cost and boiling point.[101-103] It is notable that since slow evaporation of the solvent could enhance the aggregation possibility of exfoliated GCN nanosheets, IPA could be more preferable than NMP (owing to its easier removal).[101] Schematic illustration of the fabrication process of GCN nanosheets from bulk GCN by liquid exfoliation process (using IPA and NMP), photographs of bulk GCN and suspension of GCN nanosheets, and perfect crystal structure of the GCN nanosheets (along the z axis) are shown in Figure 4. It is worth mentioning that heteroatom-mediated and template-assisted methods are among common bottom-up approaches.[65]

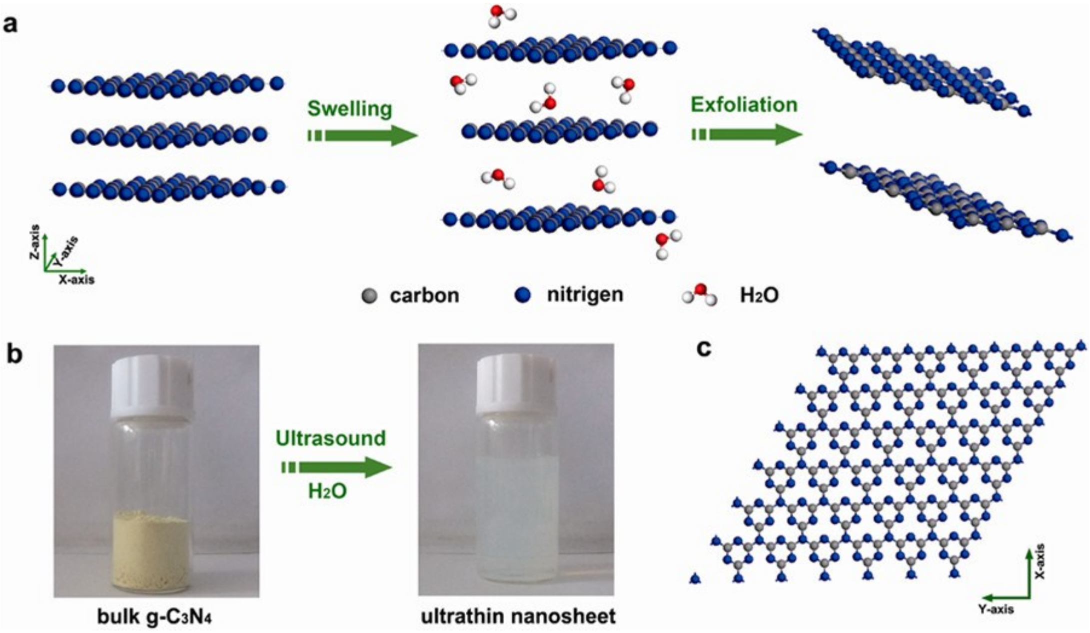

Figure 4. (a) Schematic illustration of the fabrication process of g-C_3N_4 nanosheets from bulk g-C_3N_4 powder using liquid exfoliation. Reprinted with permission from Ref. [89] Copyright 2013 American Chemical Society. (b) Photograph of suspension of g-C_3N_4 nanosheets and bulk g-C_3N_4. Reprinted with permission from Ref. [89] Copyright 2013 American Chemical Society. (c) Perfect crystal structure of g-C_3N_4 nanosheets along the z-axis. Reprinted with permission from Ref. [89] Copyright 2013 American Chemical Society.

3.3.2. High-shear mixing and ball milling

Although sonication of bulk GCN in appropriate solvents could result in the formation of defect-free GCN nanosheets, the existence of planar hydrogen bonding between C-N layers of GCN and the low energy of ultrasonication might limit its yield and scalability.[104] Liquid exfoliation techniques tend to yield either no-defect (or low-defect) contents or high production rates.[105] Besides, some methods could break the chemical structure, consequently, providing low quality nanosheets.[104] Thus, shear mixing has been extensively used for the dispersion of nanoparticles in liquids. Overall, high-shear mixing could be considered as a substantial alternative to sonication for exfoliation of layered materials.[105] Yan et al. used high-shear mixing for exfoliation of bulk g-C_3N_4 for the first time (water was used as the dispersion agent).[104] Although the thickness of g-C_3N_4 nanosheets provided by sonication has been higher than 2 nm in some cases,[41, 106, 107] high-shear mixing can lead to the formation of nanosheets with the uniform thickness of ~0.7 nm.[104] Since the theoretical thickness of one C-N layer is ~0.325 nm,[90] it could be concluded that high-shear mixing is capable of producing GCN nanosheets (with approximately one or two C-N layers), providing much more reactive sites and higher specific surface area for photocatalytic purposes compared with general methods including sonication. Due to the possibility of fabrication of defect-free and extremely thin nanosheets, high-shear mixing could be considered a promising method for exfoliation of GCN. Furthermore, it can be easily scaled-up to industrial levels.[104] Owing to its low cost and facile operation, ball milling (mechanical milling) has also been employed as a simple method for the synthesis of large quantities of some 2D materials (e.g. graphene and boron nitride).[108] Overall, it is considered an efficient strategy to produce ultrathin GCN with plentiful porosity (due to the mechanical forces).[109] Ball milling process could be performed at dry or wet condition. However, the properties of the final products could be different. Ma et al. used wet ball milling to exfoliate GCN for the photocatalytic decomposition of organic pollutants,[110] while Zhu et al. used dry ball milling for the scalable production of g-C_3N_4 nanosheets.[108] In milling process, the friction and shear force of grinding balls gradually weakens the van der Waals interactions,[108-110] whereas the strong sp^2 bonded in-plane structure could remain stable.[108] The schematic illustration of the mechanical exfoliation of bulk g-C_3N_4 using ball milling process is shown in Figure 5(a).

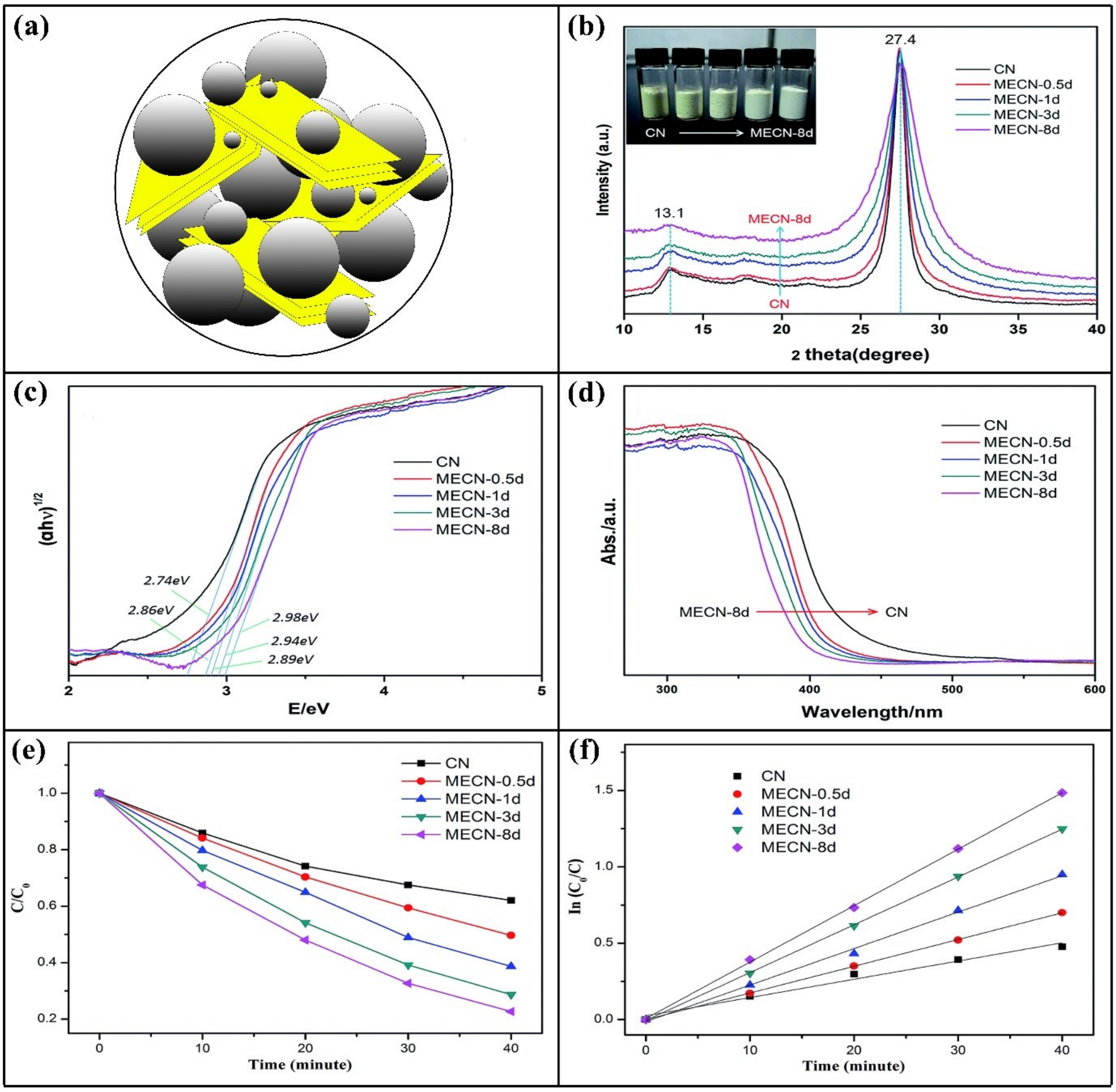

Figure 5. (a) Schematic illustration of the mechanical exfoliation of bulk g-C_3N_4 using ball milling process. Redrawn from Ref. [108] Copyright 2015 The Royal Society of Chemistry (https://pubs.rsc.org/en/content/articlelanding/2015/ra/c5ra09040g). (b) XRD patterns of GCN nanosheets after milling for 0.5, 1, 3 and 8 days. Reproduced with permission from Ref. [108] Copyright 2015 The Royal Society of Chemistry (https://pubs.rsc.org/en/content/articlelanding/2015/ra/c5ra09040g). (c) Photo-adsorption ability of GCN nanosheets after milling for 0.5, 1, 3 and 8 days. Reproduced with permission from Ref. [108] Copyright 2015 The Royal Society of Chemistry (https://pubs.rsc.org/en/content/articlelanding/2015/ra/c5ra09040g). (d) Band gap energies of

GCN nanosheets after milling for 0.5, 1, 3 and 8 days. Reproduced with permission from Ref. [108] Copyright 2015 The Royal Society of Chemistry (https://pubs.rsc.org/en/content/articlelanding/2015/ra/c5ra09040g). Effect of milling time on the photocatalytic activity of GCN in terms of (e) C/C_0 and (f) ln (C_0/C) vs t (min). Reproduced with permission from Ref. [108] Copyright 2015 The Royal Society of Chemistry (https://pubs.rsc.org/en/content/articlelanding/2015/ra/c5ra09040g).

The XRD patterns and color of g-C_3N_4 nanosheets after milling for 0.5, 1, 3, and 8 days are shown in Figure 5(b). Increasing the milling time led to change of the color of g-C_3N_4 from yellow to white, signifying change of the photo-absorption ability. Besides, increasing the milling time has broaden widths of the diffraction peaks which can be attributed to either the induced-strain or change of the crystallite size. The band gap energy and photo-absorption ability of g-C_3N_4 at different milling times are shown in Figures 5(c) and 5(d), respectively. As evident, the photo-absorption ability decreased by increasing the milling time. On the other hand, the band gap energy increased which could be attributed to the quantum confinement effect originated from the shift of conduction band and valence band edges in different directions (due to change in the density of electronic states).[108] Yang et al. also observed the same trend for g-C_3N_4 nanosheets synthesized by ultrasonication.[101] The effect of milling time on the photocatalytic activity of GCN is shown in Figures 5(e) and 5(f). The longer the milling time, the higher photocatalytic activity is observed. Although ball milling led to a decrease in the photo-absorption ability, the higher specific surface area of GCN nanosheets yielded a higher photocatalytic activity than bulk GCN, clarifying the crucial importance of the surface area in photocatalytic reactions.[108]

Taking advantage of the layered structure of both MoS_2 and g-C_3N_4, Ansari et al. used dry mechanical milling for the synthesis of large scale 2D MoS_2-GCN heterostructures for the photocatalytic degradation of RhB under visible-light irradiation.[116] The 2D MoS_2(10%)-GCN heterostructure showed much higher photo-absorption ability than that of bare bulk g-C_3N_4. Although the PL intensity of MoS_2(10%)-g-C_3N_4 heterostructure was lower than that of bulk g-C_3N_4, the emission band of MoS_2(10%)-g-C_3N_4 heterostructure remarkably reduced (compared with bare bulk g-C_3N_4). Overall, MoS_2(10%)-g-C_3N_4 heterostructure showed much higher photocatalytic activity than both bare bulk g-C_3N_4 and bare g-C_3N_4 nanosheets.[111]

3.3.3. Chemical exfoliation

Although ultrasonication has been widely used for the exfoliation of GCN, it suffers from its low energy input and unsatisfactory efficiency, consequently. Overall, liquid phase exfoliation using ultrasonication could not be considered as a potential method for mass production of nanosheets.[112] Besides, it usually results in the formation of GCN nanosheets with larger thicknesses than 2 μm.[41, 106, 107] Compared with liquid phase exfoliation using ultrasonication, chemical exfoliation has considerable advantages including the incorporation of guests between the layers, and the formation of thinner nanosheets (unilamellar nanosheets). Besides, it can take advantage of high efficiency of exfoliation and its cost-effectiveness.[90] H_2SO_4 is considered a potential candidate for such a purpose owing to its mild oxidation effect (unlike $KMnO_4$ as a strong oxidant).[113-115] Although $KMnO_4$ has been used for exfoliation of graphite in the Hummers method, generally, it cannot be used for exfoliation of GCN due to the weak stability of GCN against strong oxidation effect of $KMnO_4$.[113] Niu et al. showed that Hummers method can only be used for the production of g-C_3N_4 with thickness of several hundred nanometers (rather than nanosheets).[116] Both diluted and concentrated sulfuric acid have been used for chemical exfoliation of GCN. Although diluted H_2SO_4 was introduced as an "efficient knife" to create large-aspect-ratio nanosheets, it provided the final yield of ~60%. Using concentrated H_2SO_4 led to the formation of g-C_3N_4 nanosheets in a short time (< 30 min) with the final yield of ~70%. Notably, this method is scalable and can be used for the fabrication of uniform g-C_3N_4 nanosheets. Schematic illustration of the synthetic strategy of production of GCN nanosheets using concentrated H_2SO_4 is shown in Figure 6.[115] Although chemical oxidation could be effectively used for exfoliation of g-C_3N_4, the thickness of GCN nanosheets could be significantly affected by the procedure. For example, using H_2SO_4 for chemical exfoliation of g-C_3N_4, as reported by Tong et al., led to the production of g-C_3N_4 nanosheets with a thickness of ~80 nm.[115] While Xu et al. produced monolayer GCN nanosheets by chemical oxidation using H_2SO_4.[113] Although chemical exfoliation is a rapid and facile method for the production of GCN nanosheets, even after a short time around 1 min, it could suffer from its low yield in some cases like that reported by Zou et al (i.e. ~30%).[114] In addition, the acid treatment involved could be cumbersome.[115] On the other hand, ultrasonic exfoliation in polar solvents takes a long time[115] and its dispersion efficiency is low.[117]

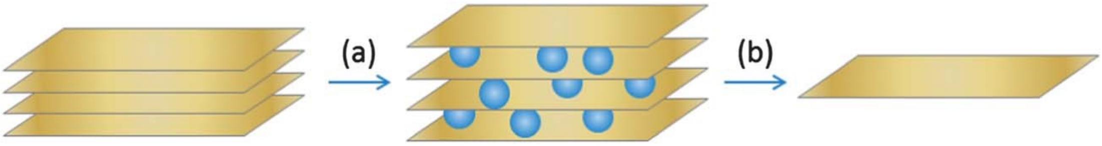

Figure 6. Synthetic strategy of production of g-C_3N_4 nanosheets using concentrated H_2SO_4: (a) Intercalation of H_2SO_4 (98 wt%) in the interplanar space of g-C_3N_4 and (b) Exfoliation of intercalated g-C_3N_4 into a single layer. Reproduced with permission from Ref. [113] Copyright 2013 The Royal Society of Chemistry (https://pubs.rsc.org/en/content/articlelanding/2013/ta/c3ta13188b).

3.3.4. Thermal oxidation exfoliation

It has been shown that thermal oxidation of bulk GCN in air is another method for the fabrication of g-C_3N_4 nanosheets. Firstly, Niu et al. developed a simple method called “direct thermal oxidation etching” to create g-C_3N_4 nanosheets. Since strands of polymeric melon units are connected to each other by hydrogen bond, they are not stable enough against oxidation in air. Thus, they could be oxidized away gradually, from pristine g-C_3N_4 so that its thickness decreases to the nanometer scales. This is a low-cost method which can be easily scaled up. Besides, it takes advantage of its environmental friendliness (unlike chemical exfoliation). Notably, GCN nanosheets with a thickness of ~2 nm could be fabricated using this method.[116] The schematic illustration of the synthetic process of GCN nanosheets using thermal oxidation of pristine GCN in air is shown in Figure 7. Zhang et al. exfoliated g-C_3N_4 using various techniques. The yields of thermal, chemical, and ultrasonic exfoliation methods were 47.5%, 58.1%, and 14.7%, respectively, whereas ultrasonic exfoliation in polar solvents using a mixture of ethanol and water (25:75, v/v) provided the lowest yield of all.[118]

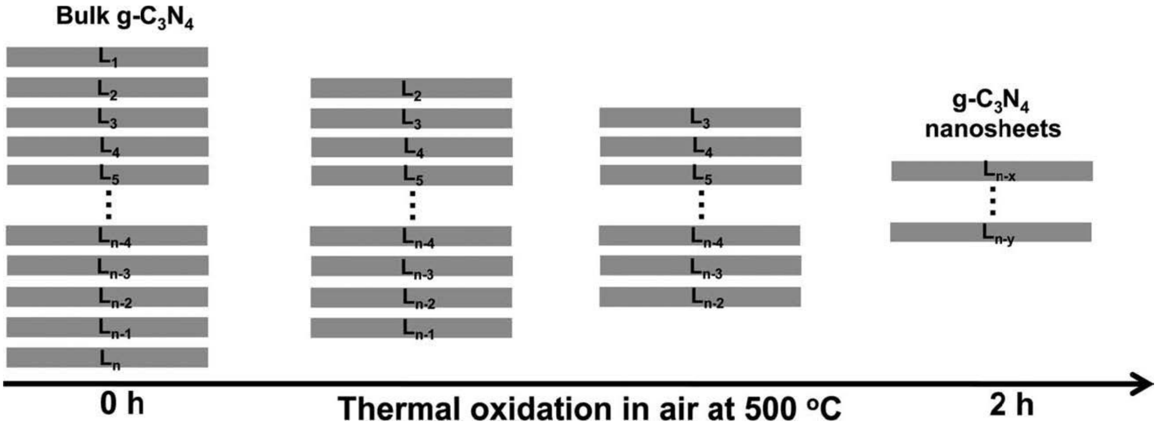

Figure 7. Schematic illustration of the synthetic process of GCN nanosheets using thermal oxidation of pristine GCN in air at 500 ˚C. Reproduced with permission from Ref. [116] Copyright 2012 John Wiley and Sons.

3.3.5. Gas bubble templating

Generally, a post-treatment such as ultrasonication, thermal oxidation, or chemical exfoliation, is required to produce GCN nanosheets from bulk GCN (Figure 8(a), pathway (I)). Besides, most of the current methods suffer from their prolonged duration, energy consumption, and low yield.[119] As shown in Figure 8(a) pathway (II), the simple one-step exfoliation of the g-C_3N_4 has been recently applied using different ammonium salts such as ammonium bromide, ammonium chloride, ammonium sulfate, ammonium phosphate, or ammonium fluoride for large-scale production of GCN nanosheets.[50, 53, 119-121] Noteworthy, the polymerization process of melamine could be modified by generation of bubbles evolved from decomposition of the additive ammonium salts, at various stages of polymerization.[53] Lu et al. used the mixture of dicyandiamide (as the GCN precursor) and ammonium chloride (as the gas bubble template) to synthesize crinkly 2D nanosheets. Notably, 2D-GCN nanosheets not only exhibited higher BET surface area than bulk GCN, but also increased the electron transport ability and improved the lifetime of charge carriers, resulting in the higher efficiency of GCN nanosheets than bulk GCN for photocatalytic hydrogen production.[120] Depending on the type of ammonium salts, their addition to the precursor of g-C_3N_4 can not only produce GCN nanosheets, but also provide Br-, Cl-, P-, and F-doped GCN simultaneously.[53, 119, 121] Notably, both Br- and Cl-doped GCN nanosheets exhibited higher photo-absorption ability in the visible-light region (wavelengths of 450-800 nm). Besides, they both yielded lower recombination rates of charge carriers than bulk GCN, resulting in their higher photocatalytic activity for the degradation of oxytetracycline antibiotic.[119] In addition, F-doped GCN nanosheets showed lower photo-absorption ability than bulk g-C_3N_4 in the visible region, signifying the partial destruction of the conjugated system of GCN by F doping. However, due to the much stronger photocurrent response of F-doped GCN nanosheets than bulk GCN, the photocatalytic production of H_2 gas over F-doped GCN nanosheets was ~4 times higher than that over bulk GCN.[121] Zhang et al. designed a multi-stage polymerization to produce GCN nanosheets using the mixture of melamine, urea, and volatile ammonium salts (ammonium phosphate, ammonium chloride, and ammonium sulfate). Compared with the bulk g-C_3N_4 synthesized by melamine (denoted as g-C_3N_4-M-600) with the BET surface area of 22.2 m^2 g^{-1} and HER rate of 432.0 μmol h^{-1} g^{-1}, the GCN nanosheets obtained by the mixture of melamine and urea with the addition of ammonium phosphate, ammonium chloride, and ammonium sulfate (denoted as g-C_3N_4-M-U-P-600, g-

C_3N_4-M-U-Cl-600, and g-C_3N_4-M-U-S-600 with large BET surface areas of 47.4, 103.3, and 53.5 m^2 g^{-1}, respectively) showed significantly higher photocatalytic activities for the production of H_2 gas (i.e. 1193.7, 1853.8, and 1167.8 μmol h^{-1} g^{-1}, respectively). Their improved surface structure could be evidenced by PL and photocurrent spectra as shown in Figures 8(b) and 8(c), consecutively. As evident, g-C_3N_4-M-U-P-600 and g-C_3N_4-M-U-Cl-600 catalysts exhibited the lowest PL intensity of all. As per g-C_3N_4-M-U-Cl-600, the creation of thin nanosheet structure has been accounted for the improved separation of e^-/h^+ pairs, but as per g-C_3N_4-M-U-P-600, the introduction of cyano groups to the structure has been considered the main reason for the reduced recombination rate of charge carriers. Notably, the surface charge distribution of the catalyst could be affected by the existence of cyano groups acting as electron-withdrawing groups.[53] TEM images of GCN synthesized by melamine, the mixture of melamine/urea (denoted as g-C_3N_4-M-U-600), and the mixture of melamine/urea/ammonium chloride are compared in Figures 8(d), 8(e) and 8(f), respectively. Unlike bulk GCN with its thick and dense layers, the addition of urea and ammonium chloride, acting as gas bubble-assisted GCN, resulted in a lower thickness and a flaky structure with irregular or bubble-like morphology. Although a mixture of melamine and urea, and a more complex mixture (melamine, urea, ammonium chloride) yielded a crinkly structure, a typical ultrathin nanosheet-like architecture was obtained by the latter mixture (melamine, urea, ammonium chloride), clarifying the key role of volatile ammonium salts in modifying the morphology of GCN obtained by thermal polymerization process. The surface charge of the g-C_3N_4-M-600, g-C_3N_4-M-U-600, g-C_3N_4-M-U-P-600, g-C_3N_4-M-U-S-600, and g-C_3N_4-M-U-Cl-600 catalysts were -31, -29, -38, -23, and -22 mv, respectively. Notably, the most negative surface charge was recorded for g-C_3N_4-M-U-P-600, indicating the high impact of the incorporation of P atom on the electronic properties of GCN. Once P is incorporated to the GCN framework, some covalent bonds are formed between N neighbors and P atom (using four of its total five electrons). The remained sole e^- of P atom could delocalize into the π-conjugated triazine ring, generating an electron-rich state of the P-doped GCN. Considering the negative values of zeta potentials, the repulsion interaction or electrostatic attraction could decrease the adsorption of anionic organic dyes (like MO) and improve the adsorption of cationic organic dyes (like MB) on the surface of catalysts as confirmed by evaluation of the organic dyes removal by adsorption, where the removal efficiency of MB was significantly higher than that of MO by using all catalysts. Based on their findings, the synergy of surface charge state and BET surface area played an important role in the promoted decomposition performance (for MB, MO, and RhB) and absorption of the synthesized GCN composites, i.e. g-C_3N_4-M-U-P-600, g-C_3N_4-M-U-S-600, and g-C_3N_4-M-U-Cl-600, than g-C_3N_4-M-600.[53]

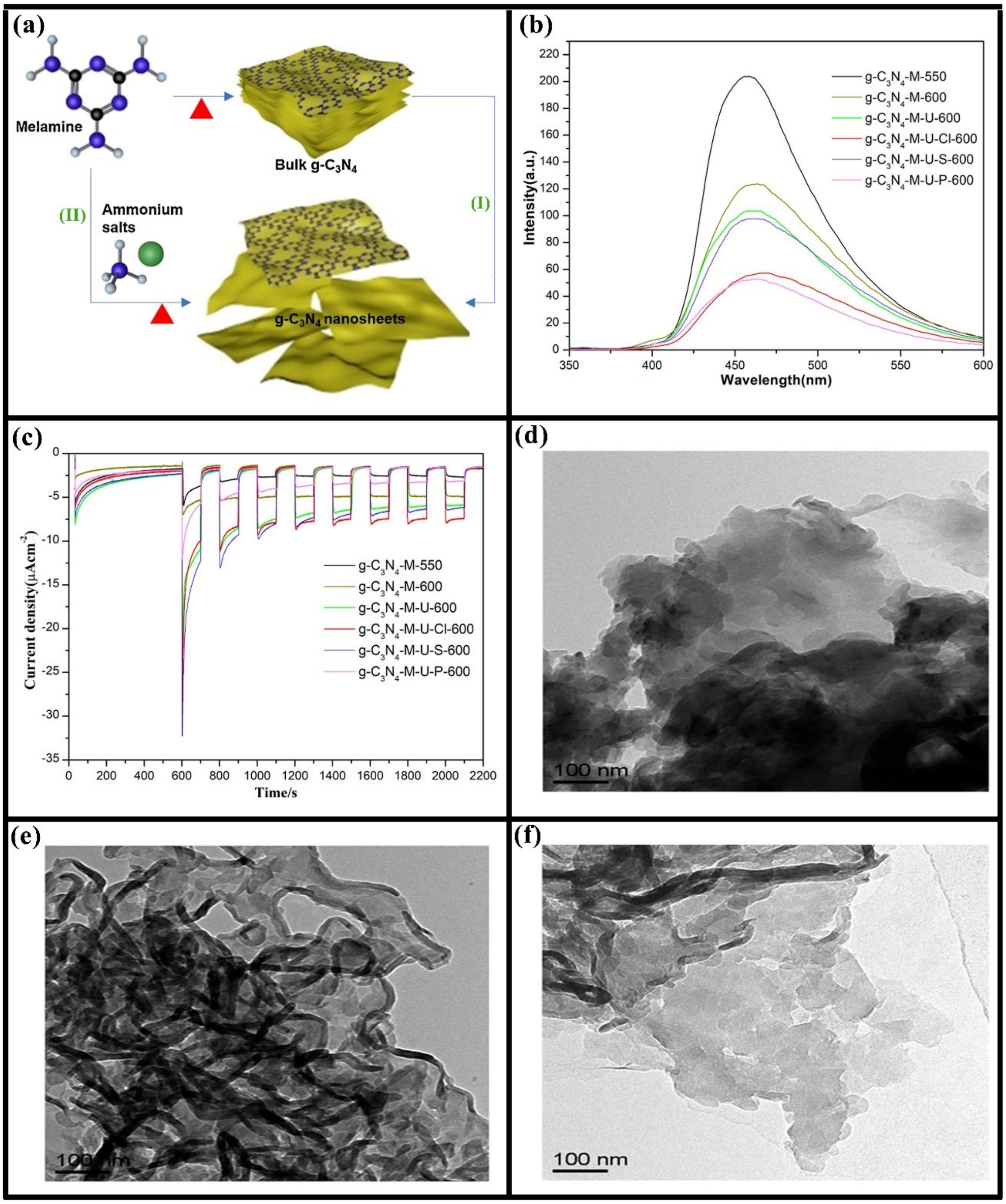

Figure 8. (a) Schematic illustration of the synthesis of GCN nanosheets by (I) post-treatment processes such as ultrasonication, thermal oxidation, or acid treatment of bulk GCN, and (II) single-step exfoliation by the addition of ammonium salts. Reprinted with permission from Ref. [119] Copyright 2019 Elsevier. (b) PL of GCN samples synthesized by melamine, the mixture of melamine/urea, and the mixture of melamine/urea/ammonium salts. Reprinted with permission from Ref. [53] Copyright 2019 American Chemical Society

(https://pubs.acs.org/doi/10.1021/acsomega.9b01510). (c) Photocurrent spectra of GCN samples synthesized by melamine, the mixture of melamine/urea, and the mixture of melamine/urea/ammonium salts. Reprinted with permission from Ref. [53] Copyright 2019 American Chemical Society (https://pubs.acs.org/doi/10.1021/acsomega.9b01510). TEM images of GCN samples synthesized by (d) melamine, (e) the mixture of melamine/urea, and (f) the mixture of melamine/urea/ammonium salts. Reprinted with permission from Ref. [53] Copyright 2019 American Chemical Society (https://pubs.acs.org/doi/10.1021/acsomega.9b01510).

3.4. One-dimensional g-C_3N_4 nanostructures

One dimensional (1D) GCN nanostructures refer to GCN nanotubes, GCN nanowires, GCN nanobelts, and GCN nanorods.[65, 122] Due to their high light harvesting, appropriate mass transfer properties, and high specific surface area, these nanostructures are promising for electrochemical and electronic applications.[65] Various methods have been used to fabricate these nanostructures. Although template assisted methods are among common methods employed for the fabrication of g-C_3N_4 nanorods (due to their ease), they need strong alkali/acid to remove the templates.[123] Bai et al. used a simple reflux method to synthesize g-C_3N_4 nanorods (without template). Notably, g-C_3N_4 nanorods showed remarkably higher photocatalytic activity (~1.5 times) than that of g-C_3N_4 nanosheets, due to the elimination of surface defects and enhancement of active lattice face.[124] Chemical vapor deposition (CVD) is among efficient methods used for synthesis of g-C_3N_4 nanotubes. Gao et al. used TiO_2 nanotubes, as appropriate templates, for synthesis of g-C_3N_4-TiO_2 nanotube arrays using chemical vapor deposition.[125] In general, CVD suffers from the toxicity of some by-products evolved during the process, and high expenses (due to the use of high temperatures).[126] Overall, using non-template methods is favored especially when removal of the template is needed.

Recently, Jiang et al. synthesized g-C_3N_4 nanotubes using thermal polymerizing reaction (without any templates). It has been concluded that tubular morphology could accelerate transfer of electrons along the axial direction which can result in the superior photocatalytic activity of GCN nanotubes than that of GCN nanosheets.[127] Apart from nanorods, template assisted method has also been used for the fabrication of GCN nanowires. Although template assisted methods are the most frequently used methods employed for production of 1D GCN, physical and chemical stimulants created by thermal treatment, ultrasonication, mechanical force, and high pressure can also be used for exfoliation and re-assembling bulk g-C_3N_4 into 1D nanostructures.[123] 1D g-C_3N_4 nanostructures could yield high photocatalytic activity, but they can suffer from the complex synthesis. Furthermore, it is worth mentioning that the compactness of films obtained by 2D structures could be higher than that achieved by 1D structures, as reported by Mohammadi et al. in the case of ZnO nanosheets and ZnO nanorods deposited by electrophoretic deposition.[128] Thus, 2D GCN nanostructures could be more promising for immobilization purposes.

3.5. Zero-dimensional g-C_3N_4 nanostructures

Zero-dimensional (0D) g-C_3N_4 nanoparticles could shorten the length of charge transfer. Besides, they exhibit more rich surface active cites for catalytic purposes.[129] 0D GCN refers to GCN quantum dots (GCN QDs) where photogenerated electron-hole pairs are not able to transfer freely.[123] GCN nanostructures with the size of below 10 nm exhibit remarkable quantum confinement effects. Moreover, they usually provide unique properties including non-toxicity, bright fluorescence, and water solubility. Both top-down and bottom-up methods have been used to synthesize g-C_3N_4 QDs.[65] In top-down methods, the synthesis of g-C_3N_4 QDs starts with macroscopic g-C_3N_4 structures which is followed by some processes including evaporation-condensation, sonication, hydrothermal treatment, and hydrolysis methods to fabricate 2D/1D GCN nanostructures and finally GCN QDs. In bottom-up methods, carbon and nitrogen rich precursors are used in some processes such as microwave-assisted methods, solid phase reactions, and quasi-chemical vapor deposition to synthesize GCN QDs.[130] Although g-C_3N_4 nanomaterials indicated great potential in the field of photocatalysis, general synthetic methods for 0D g-C_3N_4 nanoparticles suffer from tedious cleaning processes and complex oxidation-reduction reactions, usually, resulting in their low yields and prolonged synthesis. Noteworthy, 0D g-C_3N_4 nanoparticles generally have wider band gap energy than 2D/3D g-C_3N_4 materials, originated from the quantum size effect, limiting their visible-light harvest. Besides, the complex structure of 0D g-C_3N_4 nanoparticles has challenged systemic evaluation of the photocatalytic mechanism.[129]

4. Strategies to overcome the drawbacks of pristine g-C_3N_4

Despite its advantages, the photocatalytic activity of bare g-C_3N_4 is not satisfactory due to the three major reasons as follows:[131, 132]

i. Fast recombination of the photogenerated electron-hole pairs that results in low quantum efficiency,
ii. Inefficient absorption of solar light, and
iii. Low surface area (by using some precursors such as melamine) and non-textured pores due to the high degree of condensation of monomers.

The recombination rate of photogenerated e^-/h^+ pairs should be minimized to achieve high photocatalytic activity for decontamination of organic pollutants. For such a purpose, several strategies could be considered including using the mixed precursors of GCN, heterojunction structures, applying a bias potential, and element doping.

4.1. Multi-component precursors of GCN for generation of supramolecular aggregates

The formation of supramolecular aggregates is a potential approach to overcome the shortcomings of GCN.[133-136] Liao et al. tailored to the morphology of g-C_3N_4 by self-assembly and calcination using the mixtures of melamine and urea with different molar ratios of 1:3, 1:2, 1:1, 2:1, and 3:1, and the fixed amount of cyanuric acid. The SEM images of bulk GCN synthesized by melamine and GCN-x catalysts synthesized using a mixture of melamine and urea (x denotes the molar ratio of melamine to urea) are compared in Figure 9(a-f). As evident, the morphology of bulk GCN is thoroughly different from those obtained by using the mixture of melamine and urea. Notably, GCN-3:1 provided a hollow structure with BET surface area of 71.6 m^2 g^{-1}, while GCN-1:1 and GCN-1:3 yielded tube-embedded and wormlike morphologies with BET surface areas of 49.6 and 97.4 m^2 g^{-1}, consecutively. Overall, the morphology of GCN significantly varied from hollow to wormlike structure by tuning the molar ratio of melamine to urea. Noteworthy, due to the shift of the valence and conduction band edges in opposite directions, originated from the quantum confinement effect, GCN-x catalysts exhibited marginally higher band gap energies than that of bulk GCN. The photocatalytic degradation of RhB over all GNC-x catalysts was higher than that over bulk GCN with the highest apparent rate constant of 0.1746 min^{-1} for GCN-1:3, owing to its high BET surface area and low recombination rate of charge carriers evidenced by PL spectra in Figure 9(g).[137] Martha et al. have also evaluated the effect of mixing urea and melamine on the photocatalytic production of hydrogen in an aqueous solution with 10 vol% of TEA solution as sacrificial electron donor. The bandgap energies of GCN synthesized by urea, melamine, and the unimolar mixture of urea/melamine were 2.72, 2.70, and 2.71 eV; and the BET surface areas were 50, 30, and 10 m^2 g^{-1}, respectively. Compared with GCN synthesized by urea and melamine with generation of 25 and 30 μmol H_2 gas, that synthesized by the unimolar mixture of urea and melamine exhibited the highest efficiency (48 μmol), which could be highly related to the significantly reduced recombination rate of charge carriers as confirmed by PL (Figure

9(h)) and photocurrent spectra (Figure 9(i)). Further improvement was carried out by loading Pt (1 wt%), as a co-catalyst, on the surface of catalysts where the evolution rate of H_2 increased from 48 µmol to 135 µmol over the Pt-loaded GCN catalyst synthesized by the unimolar mixture of melamine and urea. It should be noted that the layers of GCN sheets were well separated using the mixture of urea and melamine. Hence, TEA solution could easily penetrate between the GCN layers, facilitating the reduction reaction. Upon light irradiation, the photogenerated h^+ in the VB of GCN could oxidize and decompose TEA, while the photogenerated e^- in the CB of GCN could reduce H^+ to H_2 through Pt loaded on the surface of catalyst.[82] The proposed reactions of TEA, acting as sacrificial electron donor, in H_2 generation systems as provided in equations (4)-(7):[2, 138]

$$\boldsymbol{C_6H_{15}NO_3 \rightarrow C_6H_{15}NO_3^{+} + e^{-}} \tag{4}$$

$$\boldsymbol{C_6H_{15}NO_3^{+} \rightarrow C_6H_{14}NO_3^{\bullet} + H^{+}} \tag{5}$$

$$\boldsymbol{C_6H_{14}NO_3^{\bullet} \rightarrow C_6H_{14}NO_3^{+} + e^{-}} \tag{6}$$

$$\boldsymbol{C_6H_{14}NO_3^{+} + H_2O \rightarrow C_4H_{11}NO_3 + CH_3CHO + H^{+}} \tag{7}$$

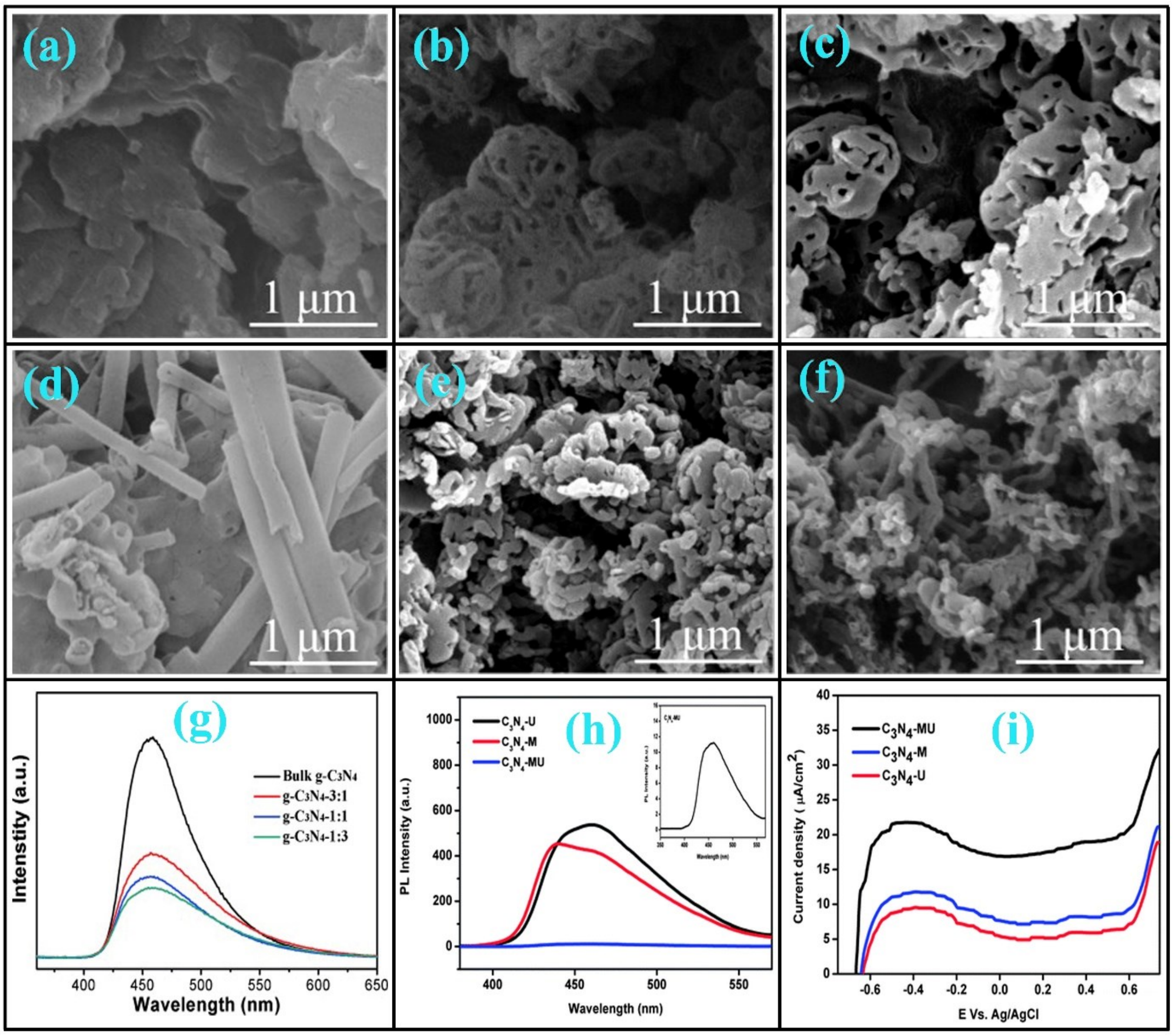

Figure 9. SEM images of (a) bulk GCN, (b) GCN-3:1, (c) GCN-2:1, (d) GCN-1:1, (e) GCN-1:2, and (f) GCN-1:3 samples. Reproduced with permission from Ref. [137] Copyright 2014 John Wiley and Sons. (g) Photoluminescence spectra of bulk GCN, GCN-3:1, GCN-1:1, and GCN-1:3 samples. Reproduced with permission from Ref. [137] Copyright 2014 John Wiley and Sons. (h) Photoluminescence spectra of GCN synthesized by urea, melamine, and their mixture. Reproduced with permission from Ref. [82] Copyright 2013 The Royal Society of Chemistry (https://pubs.rsc.org/en/content/articlelanding/2013/TA/c3ta10851a). (i) Photocurrent spectra of GCN synthesized by urea, melamine, and their mixture. Reproduced with permission from Ref. [82] Copyright 2013 The Royal Society of Chemistry (https://pubs.rsc.org/en/content/articlelanding/2013/TA/c3ta10851a).

The beneficial effect of using the combined precursors of g-C_3N_4 on the photocatalytic activity was also reported by Zhang et al. by mixing urea and thiourea where the optimal rate of HER over the GCN synthesized by the mixture (2.44% mass fraction of thiourea) was 2.60 and 6.17 times higher than those synthesized by urea and thiourea, respectively. Notably, both enlarged BET surface area and reduced recombination rate of charge carriers were responsible for the superior photocatalytic activity of GCN synthesized by the mixture of urea and thiourea.[139] It is obvious the effect of combined precursors of g-C_3N_4 on BET surface area of the final product highly depends on the type of precursors and their weight/molar ratio. In another research, the mixture of melamine and cyanuric acid (5 and 5.1 g, respectively) was used to synthesize GCN where BET surface area remarkably increased from 7 to 70 m^2 g^{-1} for the g-C_3N_4 synthesized by melamine and the mixture of melamine and cyanuric acid, consecutively, which is related to the formation of nanoporous GCN layers in the presence of cyanuric acid.[140] Recently, Zhang et al. used a mixture of urea (15 g) and melamine (6 g) to synthesize GCN for the photocatalytic production of H_2 gas. The photocatalytic production rate of hydrogen gas by using GCN synthesized from the mixture of urea and melamine (1395.4 μmol h^{-1} g^{-1}) was remarkably higher than that synthesized by melamine (432.0 μmol h^{-1} g^{-1}). For further improvement, 4g ammonium chloride was added to the mixture of urea and melamine. Furthermore, the addition of ammonium chloride significantly increased the photocatalytic production rate of H_2 gas (1853.8 μmol h^{-1} g^{-1}) which is related to the improved BET surface area (originated from the production of GCN nanosheets), surface charge state, and surface structure of the synthesized GCN nanosheets.[53]

4.2. Element doping and defects engineering

By tuning the bandgap structure, doping heteroatoms could extend the light harvest and fasten the mobility of charge transfer.[121] Therefore, to improve the photocatalytic efficiency of GCN, various metal and non-metal elements (cations and anions, respectively) have been incorporated into its lattice. However, the mechanism of tuning the bandgap structure highly depends on the type of dopant. For instance, B doping shifts the valence band towards more positive values,[141] whereas P doping shifts the valence band towards more negative values.[142] Notably, the intrinsic Lewis base sites (in the form of imine or amine groups) together with the formation of Lewis acid sites originated from the generation of P^+ centers by doping phosphorus, as illustrated in Figure 10(a), could result in delocalization of lone electrons, favoring the fast separation of charge carriers.[143] Simultaneously, creation of the defective bands within the band gap of GCN by phosphorus doping could increase the visible-light harvest and narrow its band gap energy,[144] resulting in the remarkable increase of the photocatalytic activity of P-doped GCN compared to that of bare g-C_3N_4.[142, 145, 146] In addition, phosphorus doping could significantly enhance the low yield of GCN by using urea which is of the major drawbacks associated with using this precursor (despite of its several advantages). For instance, the yield of GCN remarkably increased from 3% (for bare GCN) to 25% (for P-doped GCN) by the addition of 10wt% hexachlorocyclotriphosphazene (HCCP) as the phosphorus source.[79] Thus, it is considered a superior and ideal doping element to control the surface properties (texture) and electronic structure of GCN.[144, 147, 148] The photocatalytic production rates of H_2 gas over bare GCN and P-doped GCN are compared in Table 3.

Table 3. Comparison of the photocatalytic hydrogen production between bare g-C_3N_4 and element-doped g-C_3N_4.

Element doped	**Photocatalytic H_2 evolution (μmol h^{-1} g^{-1})**				**Light source**	**Apparent quantum yield (AQY) for element-doped GCN (%)**	**Reference**
	Bare GCN	**Element-doped GCN**	**Amount of Pt as co-catalyst (wt%)**	**Type and amount of sacrificial agent (vol%)**			
P	60	570	1	Methanol (20)	300 W Xenon lamp	-	[146]
P	107	318	1	TEA (10)	300 W Xenon lamp	-	[147]
P	~174	506	3	TEA (10)	300 W Xenon lamp	-	[143]
P	208	5128	3	TEA (10)	300 W Xenon lamp	-	[142]
P	430	2020	3	TEA (10)	300 W Xenon lamp	4.32 (λ = 420 nm)	[145]
B	330	910	1	TEA (10)	150 W Xenon lamp	-	[149]
S	330	615	1	TEA (10)	150 W Xenon lamp	-	[149]
P	330	575	1	TEA (10)	150 W Xenon lamp	-	[149]

S	449.86	1186.38	3	TEA (10)	300 W Xenon lamp	10.2 (λ = 420 nm)	150
S	68	572	3	TEA (10)	300 W Xenon lamp	0.39[*] (λ = 420 nm)	151
S	20.3	121.6	1	Methanol (25)	300 W Xenon lamp	2.6 (λ = 420 nm)	152
Ni	98.67	155.71	~3	TEA (10)	300 W Xenon lamp	-	153
Zn	27.5	297.5	0.5	Methanol (~18.5)	200 W Xenon lamp	3.2 (λ = 420 nm)	154
Co	190	560	3	TEA (10)	300 W Xenon lamp	-	155
Na	96	~144	3	TEA (10)	300 W Xenon lamp	-	156
K	96	~606	3	TEA (10)	300 W Xenon lamp	-	156
Mo	0	0	0	Methanol (10)	300 W Xenon lamp	-	157
S	0	0	0	Methanol (10)	300 W Xenon lamp	-	157
Mo and S	0	294	0	Methanol (10)	300 W Xenon lamp	0.24 (λ = 420 nm)	157
P and O	86	159	0[**]	TEA (~14.3)	300 W Xenon lamp	-	158

[*]: Extracted from the publication by Plot Digitizer

[**]: 5 mg of Erythrosin B was added to the initial aquatic solution as sensitizer

As evident, phosphorus doping has significantly improved the photocatalytic evolution rate of hydrogen gas in all cases. Guo et al. fabricated P-doped tubular GCN for photocatalytic production of hydrogen using several phosphorus sources including sodium pyrophosphate, ammonium phosphate, sodium hypophosphite, and sodium phosphite. Notably, all synthesized P-doped GCN catalysts by these phosphates (CN-SP, CN-AP, CN-SH, CN-SPh, respectively) showed higher photocatalytic activity than that of bare GCN (Figure 10(b)). Among these phosphates, the highest efficiency was obtained by sodium pyrophosphate which has been attributed to the high amount of phosphorus doped. Furthermore, the separation of charge carriers increased and the visible-light harvest improved by using sodium pyrophosphate as confirmed by UV-vis DRS spectra and Electrochemical Impedance Spectroscopy (EIS) Nyquist plots in Figures 10(c) and 10(d), respectively. Considering computational results, projected density of states (PDOSs) changed a lot by P-doping, and the CB shifted to a position with a lower energy, resulting to the reduction of the band gap energy confirmed by UV-vis DRS spectra. Based on their calculations, both introduction of phosphorus to the CB and the formation of surface carbon defects could be responsible for the reduced band gap energy by P-doping. The bulk C/N mass ratios of bulk GCN and CN-SP (obtained by the Element Analyzer) were both 0.68, while the corresponding surface C/N atomic ratios (obtained by XPS) were 0.74 and 0.69, clarifying the formation of carbon defects only on the surface of GCN. The co-introduction of surface carbon defects and P-doping with enlarged BET surface area (28.2 m^2 g^{-1} against 8.6 m^2 g^{-1}) have been accounted for the considerably higher photocatalytic activity of CN-SP than bulk GCN.[146] Recently, Yang et al. synthesized 3D flower-like P-doped GCN (Figure 10(e)) with a high content of porosity and surface area using the mixture of cyanuric acid and melamine as the supramolecular precursor of g-C_3N_4 and phosphoric acid as the phosphorus source. The beneficial effects of combined precursors for synthesis of GCN were explained in the previous section. BET specific surface area of bulk

GCN (synthesized by melamine) and P-doped GCN catalysts (synthesized by the mixture of cyanuric acid and melamine and different amounts of phosphoric acid from 0 to 0.5, 1.0, 1.5, and 2.0 g) were 9.87, 96.12, 126.25, 235.85, 222.12, and 152.00 m^2 g^{-1}, consecutively. Notably, using the combined precursor significantly increased BET surface area from 9.87 (for GCN synthesized by melamine) to 96.12 m^2 g^{-1} (for GCN synthesized by the mixture of melamine and cyanuric acid). Furthermore, phosphorus doping using phosphoric acid remarkably increased BET surface area compared to bare GCN. The unique structure associated with phosphorus doping resulted in the improved visible-light harvest (Figure 10(f)) and the increased separation efficiency of charge carries (Figure 10(g)), remarkably promoting the H_2 evolution rate over the optimal P-doped g-C_3N_4 catalyst, fabricated by the addition of 1.5 g phosphoric acid, compared with bare g-C_3N_4 (almost 24-fold). Notably, Pt nanoparticles (3 wt%) were deposited on the surface of the as-prepared GCN samples (as co-catalyst). The remarkably higher surface reactivity and surface area provided by the distinctive hierarchical structure containing ultrathin porous nanosheets resulted in the much higher photocatalytic activity of the optimal P-doped g-C_3N_4 than bare GCN.[142] It should be noted that the effect of phosphorus doping on BET surface area largely depends on the type of precursors used for synthesis of GCN and the phosphorus source. Bellardita et al. used ammonium dihydrogen phosphate to synthesize P-doped GCN using three different precursors of urea, melamine, and thiourea. The BET surface areas of GCN synthesized by urea, melamine, and thiourea were 28, 7 and 5 m^2 g^{-1}, which were changed to 16, 4 and 28 m^2 g^{-1} respectively with phosphorus doping. Notably, depending on the type of precursor, doping phosphorus could affect the textural properties of the obtained GCN. It has been proposed that the effects of evolution of H_2S and CS_2 gases during condensation of thiourea is not similar to the effect of evolution of CO_2 during condensation of urea which is responsible for the superior BET surface area of g-C_3N_4 synthesized by urea compared to that synthesized by thiourea. Thus, the probable reaction of

H_2S and CS_2 with oxygen of the phosphorus source at high temperatures might generate volatile gases, initializing production of pores during synthesis of P-doped GCN using thiourea. In addition to BET surface area, the recombination rates of charge carriers are highly dependent on the type of precursor of g-C_3N_4. As evidenced by PL spectra in Figure 10(h-j), among P-doped GCN catalysts obtained by urea, melamine, and thiourea, only that synthesized by melamine significantly quenched the recombination rate of charge carries.[140]

More recently, Lin et al. synthesized P-doped g-C_3N_4 nanosheets using sodium hypophosphite (as the phosphorus source) for the photocatalytic hydrogen production. Pt nanoparticles (1 wt%) were deposited on the surface of the as-prepared samples (as co-catalyst). As expected, all P-doped GCN catalysts with different phosphorus contents exhibited higher efficiencies than bare GCN. Furthermore, it has been concluded that phosphorus doping could result in the formation of carbon defects by cleavage of the N-C bond of C=N-C, suppressing the recombination rate of photogenerated e^-/h^+ pairs and improving the separation of conjugated π electrons in the structure of g-C_3N_4.[147] Creation of surface carbon defects and their beneficial effects on the photocatalytic activity of P-doped g-C_3N_4 has also been reported by other researchers.[146] The reduced crystallinity of P-doped GCN compared to bare GCN is evidenced by XRD patterns shown in Figure 10(k). The significantly improved photocatalytic H_2 production of the optimal P-doped GCN compared to bare g-C_3N_4 (318 against 107 μmol h^{-1} g^{-1}, respectively) was attributed to the beneficial effects of both phosphorus doping and carbon defects. It has been proposed that P atoms replaced C atoms in C-N bond, though partially, during P doping (considering XPS analysis).[147] Schematic structures of GCN and P-doped GCN with and without the existence of carbon defects are compared in Figure 10(l).

In addition to the photocatalytic evolution of H_2 gas, P-doped g-C_3N_4 has been used for the photocatalytic degradation of organic pollutants (e.g. RhB) where the photocatalytic degradation efficiency of P-doped g-C_3N_4 was nearly 3 times higher than that of bare GCN. It is thought that the sole e$^-$ of P could delocalize to the π-conjugated triazine ring once C is replaced by P in the GCN framework during P doping. Finally, P$^+$ centers could be formed as the result of the sole e$^-$ delocalization and the built-in P-N bond polarization. Hence, the fast separation of charge carriers could be achieved by the existence of P$^+$ centers acting as Lewis acid sites (in addition to the inherent Lewis base sites in GCN as imine or amine groups), improving the photocatalytic performance in either HER or RhB decomposition.[143]

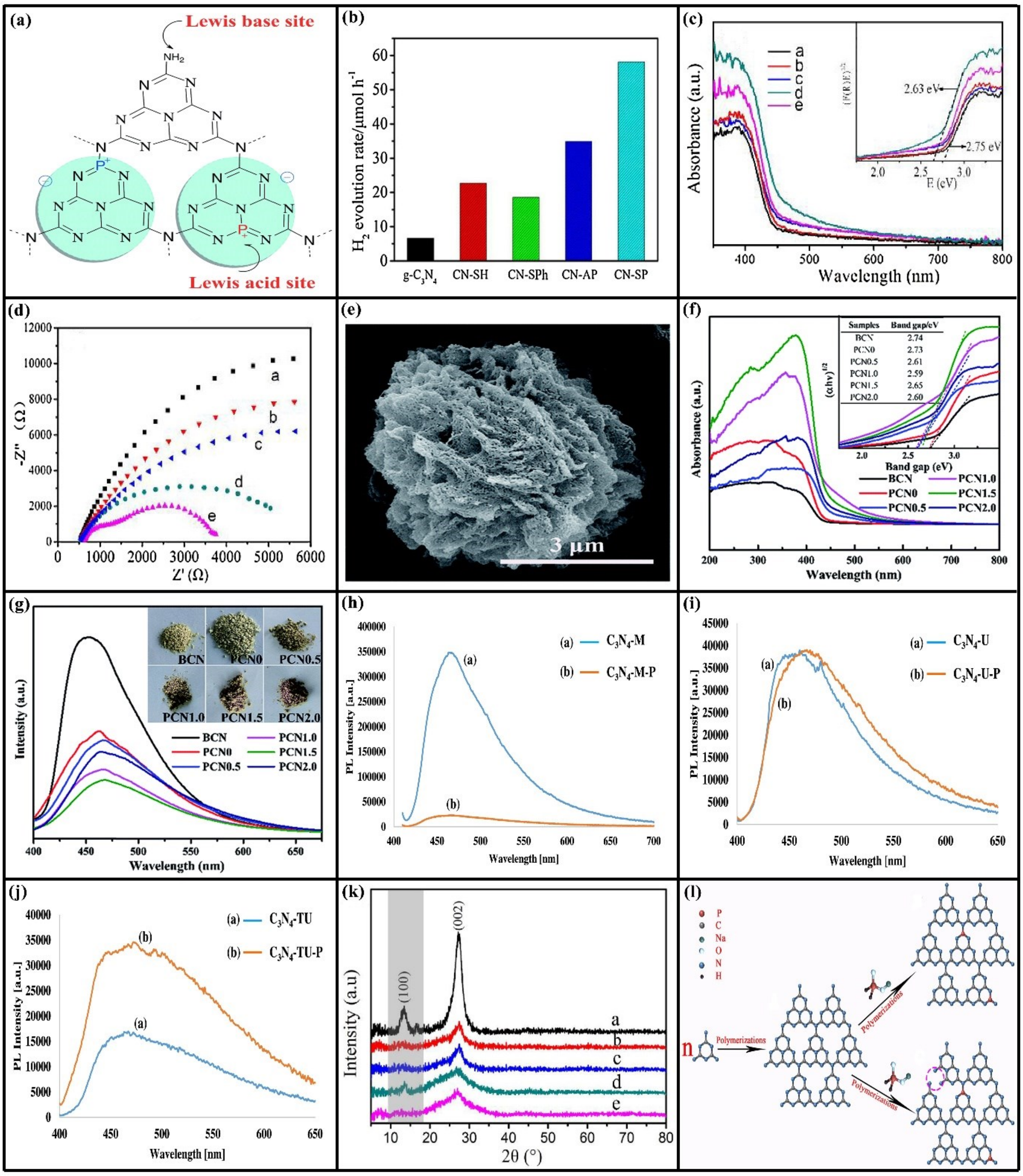

Figure 10. (a) Effects of phosphorus doping on the chemical and electronic properties of GCN. Reproduced with permission from Ref. [143] Copyright 2015 The Royal Society of Chemistry (https://pubs.rsc.org/en/content/articlelanding/2015/ta/c4ta05292g). (b) Photocatalytic activity of bulk GCN and P-doped GCN synthesized by various phosphorus sources. Reprinted with permission from Ref. [146] Copyright 2017 Elsevier. (c) UV-vis DRS spectra of bulk GCN and P-doped GCN synthesized by various phosphorus sources (a: GCN bulk, b: CN-SH, c: CN-SPH, d: CN-AP, and e: CN-SP). Reprinted with permission from Ref. [146] Copyright 2017 Elsevier. (d) EIS Nyquist plots of bulk GCN and P-doped GCN synthesized by various phosphorus sources (a: GCN bulk, b: CN-SH, c: CN-SPH, d: CN-AP, and e: CN-SP). Reprinted with permission from Ref. [146] Copyright 2017 Elsevier. (e) SEM image of 3D flower-like P-doped GCN. Reproduced with permission from Ref. [142] Copyright 2018 The Royal Society of Chemistry (https://pubs.rsc.org/en/content/articlelanding/2018/ta/c8ta05723k). Comparison of (f) UV-vis DRS and (g) PL spectra of bulk GCN (BCN) and P-doped GCN (PCNx where x clarifies the amount of phosphoric acid). Reproduced with permission from Ref. [142] Copyright 2018 The Royal Society of Chemistry (https://pubs.rsc.org/en/content/articlelanding/2018/ta/c8ta05723k). PL spectra of GCN and P-doped GCN synthesized by (h) melamine, (i) urea, and (j) thiourea. Reprinted with permission from Ref. [140] Copyright 2018 Elsevier. (k) XRD patterns of bulk GCN and P-doped GCN synthesized by various phosphorus sources (a: GCN bulk, b: CN-SH, c: CN-SPH, d: CN-AP, and e: CN-SP). Reprinted with permission from Ref. [146] Copyright 2017 Elsevier. (l) Schematic structures of GCN and P-doped GCN with and without the existence of carbon defects. Reprinted with permission from Ref. [147] Copyright 2020 Elsevier.

Overall, the introduction of non-metals to GCN could break its symmetry, resulting in the faster separation rate of charge carriers.[159] Recently, halogen doping (F, Cl, Br, and I) has been effectively used to improve the photocatalytic activity of GCN. It is notable that all halogen-doped GCN exhibited superior efficiencies than bare GCN for atrazine removal, which can distribute electrons nonuniformly and form hydrophobic sites on GCN (in addition to the reduction of band gap energy and the increase of electrons migration space). Moreover, halogen doping could either downshift VB (F and Cl) or upshift CB (I) to improve the oxidation function of holes or hydroxyl radicals.[160] Mishra et al. synthesized B-, S-, and P-doped GCN nanosheets by solid-state calcination of melamine followed by chemical exfoliation using HCl for photocatalytic HER. The band gap energies of bare GCN, S-doped GCN, B-doped GCN, and P-doped GCN were 2.70, 2.76, 2.69, and 2.77 eV, respectively. Not only B-doped GCN exhibited the minimal band gap energy, but also boron doping improved light absorption. Notably, B, S, and P doping considerably reduced the recombination rate of charge carriers (compared to bare GCN) where the minimal PL intensity was observed for B-doped GCN. Besides, B doping could reduce the charge transfer resistance (compared to bare GCN) as confirmed by photo-electrochemical measurements. They were all responsible for the significantly higher evolution rate of H_2 over B-doped GCN than bare GCN (18.2 μmol h^{-1} against 6.6 μmol h^{-1}).

It is worth mentioning that S-doped GCN also showed higher photocatalytic H_2 generation (12.3 μmol h^{-1}) than bare GCN.[149] However, the effect of S doping could be significantly improved by using mesoporous GCN structures with nitrogen defects (vacancies).[161] In general, several types of defects could exist in GCN.[162] Notably, defect engineering by the creation of vacancy defect is considered a promising strategy to boost the photocatalytic activity of GCN through different mechanisms.[163-166] Vacancy defect could include nitrogen vacancies, carbon vacancies, or dual vacancies.[164] It is notable that the electronic structure could be effectively tuned by vacancy defect which could act as the special capture centers for electrons (in parallel).[163] In addition, the lattice disorders initiated by the creation of vacancy defect could adjust VB and CB towards each other, simultaneously, reducing the band gap energy.[166] Numerous methods including multi-step calcination in a reducing environment (H_2),[164, 167] pretreatment in concentrated HNO_3,[168] and post treatment with salts (e.g. eutectic mixture KCl and LiCl)[169] have been used for the generation of nitrogen vacancies in GCN. Liu et al. synthesized S-doped and N defect co-modified mesoporous GCN for the photocatalytic H_2 generation. A high specific surface area (153.8 m^2 g^{-1}) was achieved by the mesoporous structure. In addition, S doping and N defect optimized the band structure, and reduced the band gap energy. A surplus CB energy level was also created, improving migration and separation of charge carriers. They all resulted in the extremely higher hydrogen generation rate over S-doped and N defect co-modified mesoporous GCN than S-doped GCN (4441 μmol g^{-1} h^{-1} against 91 μmol g^{-1} h^{-1}), clarifying the crucial role of nitrogen vacancy in improvement of the photocatalytic activity of GCN. At the same time, it exhibited a superior activity for the photocatalytic degradation of several organic pollutants including tetracycline hydrochloride, crystal violet, MB, and RhB.[161] He et al. synthesized C-doped and defects co-modified GCN using one-pot polycondensation of urea with the addition of ethylenediaminetetraacetic acid disodium salt (EDTA-2Na) as modifier for the photocatalytic degradation of bisphenol A (BPA) under visible light irradiation. It has been concluded that co-modification of C doping and defects could reduce the band gap energy and increase the mobility of charge carriers, consequently, resulting in the remarkably higher kinetic constant of BPA photocatalytic removal over C-doped and defects co-modified GCN (with 0.02 g EDTA-2Na) than pristine GCN (0.0269 min^{-1} against 0.0031 min^{-1}).[170]

Cation doping or metal doping is another interesting modification method of GCN to promote its photocatalytic performance.[19, 171, 172] Notably, due to the strong attraction between negatively charged nitrogen atoms and metal cations, GCN is easily capable of capturing metal cations. Moreover, cation doping could improve the photocatalytic activity of GCN.[159] Hence, in addition to non-metal doping, cation-doped g-C_3N_4 photocatalysts have received extensive attention due to their promising potential for environmental and energy-related applications. For example, Oh et al. reported that Co- and Fe-doped GCN can significantly improve the selective sulfathiazole degradation compared to pristine GCN.[173] Deng et al. found that Ni-doped GCN can increase the photocatalytic hydrogen generation up to 155.71 μmol g^{-1} h^{-1} (approximately 1.6 times higher than bare GCN). In addition, 10-fold increase in the constant rate was obtained for the photodegradation of MO. Based on their findings, higher visible light harvest, lower band gap energy, and suppressed recombination rate of charge carriers could account for the superior efficiency of Ni-doped GCN than bare GCN.[153] Other kinds of metal elements like Zn,[174] K,[156] Na,[156] Li,[175] V,[176] Cu,[176] and Ag [177] have been effectively used to enhance the photocatalytic activity of bare GCN. It has been suggested that the cation size effect could play an important role in the variation of structure and electronic/optical properties ion-doped g-C_3N_4, and consequently the improved photocatalytic H_2 generation.[156] It should be noted that delocalizability of unpaired electrons and their high concentration (initiated by cation doping) could provide high conductivity, favoring the transport and separation of charge carriers.[178] Lee et al. synthesized Mg-doped GCN, by the addition of Mg precursor ($Mg.Cl_2.6H_2O$) during the thermal condensation of urea. Then, Mg-doped GCN was suspended in ethylene glycol, with the addition of NaOH, while stirred for 2 h and heated at 160 °C for 12 h in an autoclave to synthesize nitrogen vacancy-rich GCN. The calculated band gap energies of Mg-doped GCN, pristine GCN, and nitrogen vacancy-rich GCN were 2.89, 2.79, and 2.73 eV, respectively. Unlike Mg-doped GCN, nitrogen vacancy-rich GCN reduced the band gap energy, though slightly, clarifying that N defects could improve the photo absorption ability of GCN. Moreover, nitrogen vacancy-rich GCN provided the lowest recombination rate of charge carriers and the highest mobility of charge carriers. Due to its superior properties, nitrogen vacancy-rich GCN exhibited the highest photocatalytic activity for the degradation of oxytetracycline with the efficiency of ~92% compared to that of ~46% and ~81% (after 135 min) for bare GCN and Mg-doped GCN, respectively.[165]

Despite of its several advantages, cation doping is generally accompanied with the generation of some new energy levels in the electronic structure of GCN. It changes the transition state and charge density of the initial structure. On the upside, it could increase the visible light absorption and reduce the recombination speed of electron-hole pairs. However, on the downside, the new defect energy levels could serve as recombination centers for charge carriers, leading to the decrease of quantum efficiency.[162]

Noteworthy, the metal-free character of GCN could be preserved by non-metal doping. In addition, non-metal elements are easily capable of the formation of covalent bonds with other compounds (because of high electronegativity and ionization energies) by receiving electrons during processes.[159] Actually, nitrogen triangles with six lone-pair electrons are present in the GCN framework, enabling its efficient use for nonmetal doping.[162]

In summary, both cation and anion doping can be effectively used to modify the properties of GCN while element doping followed by vacancy defect could be more promising. Notably, further detailed research is needed to fully understand the effects of cation and anion doping, and to determine the optimal approach for specific applications.

4.3. Construction of heterostructures

In general, coupling g-C_3N_4 with other semiconductors could improve the separation of charge carriers and could increase its photocatalytic efficiency, consequently. Overall, based on the relative energy band location between the two semiconductors, heterojunction structures are classified into three different groups.[179] In Type-A heterostructures, the position of the CB of photosystem I (PS I) is more negative than that of photosystem II (PS II). Besides, the position of the VB of PS II is more positive than that of PS I. Under these circumstances, the CB of PS II is positioned between the CB and the VB of PS I. By lowering the CB edge potential, the photoexcited electrons of PS I migrate to the CB of PS II (due to its lower energy). In Type-B heterostructures, the CB of PS II is more negative than that of PS I. Besides, the VB of PS I is more positive than that of PS II. By raising the VB edge potential, the VB of PS II is located between the VB and the CB of PS I (unlike Type-A). Thus, the photo-generated holes of PS I migrate to the VB of PS II.[179, 180] In Type-C heterostructures, the position of the CB of PS II is more negative than that of PS I. In addition, the position of the VB of PS II is more positive than that of PS I. Under these circumstances, although photo-generated electrons of PS I could migrate for its VB to CB, neither holes nor electrons are transferred from PS I to PS II (due to their higher energies). Noteworthy, most of the heterojunctions are categorized in Type-A system.[179]

Typically, Type-A and Type-B systems could be considered Type-II heterostructures (staggered lineup).[181] Type-II heterojunctions are the most desirable systems for photocatalytic applications.[180, 181] Type-C system is considered Type-I heterostructure (straddling alignment).[181] In order to drive a visible-light activated Type-II heterostructure, two prerequisite conditions should be considered. Firstly, the coupled semiconductor should possess strong visible light absorption. Secondly, the energy band alignment between the semiconductors should satisfy the conditions of Type-II heterojunctions.[182]

Recently, direct Z-scheme heterostructures, known as 3rd generation Z-scheme heterostructures, have received much attention due to their potential impact on photocatalytic performance compared with Type–II heterojunction photocatalysts.[180, 183-186] Schematic illustration of the typical separation routes of charge carries are compared in Figure 11 (E_f stands for Fermi level). It should be noted that the Schottky junction is constructed by a metal-like material and a semiconductor. Due to the difference in work function, the photoexcited electrons can quickly transfer from the semiconductor to the metal-like material at their interface, resulting in alignment of the Fermi energy levels and reducing the recombination rate of charge carriers, remarkably.[187, 188]

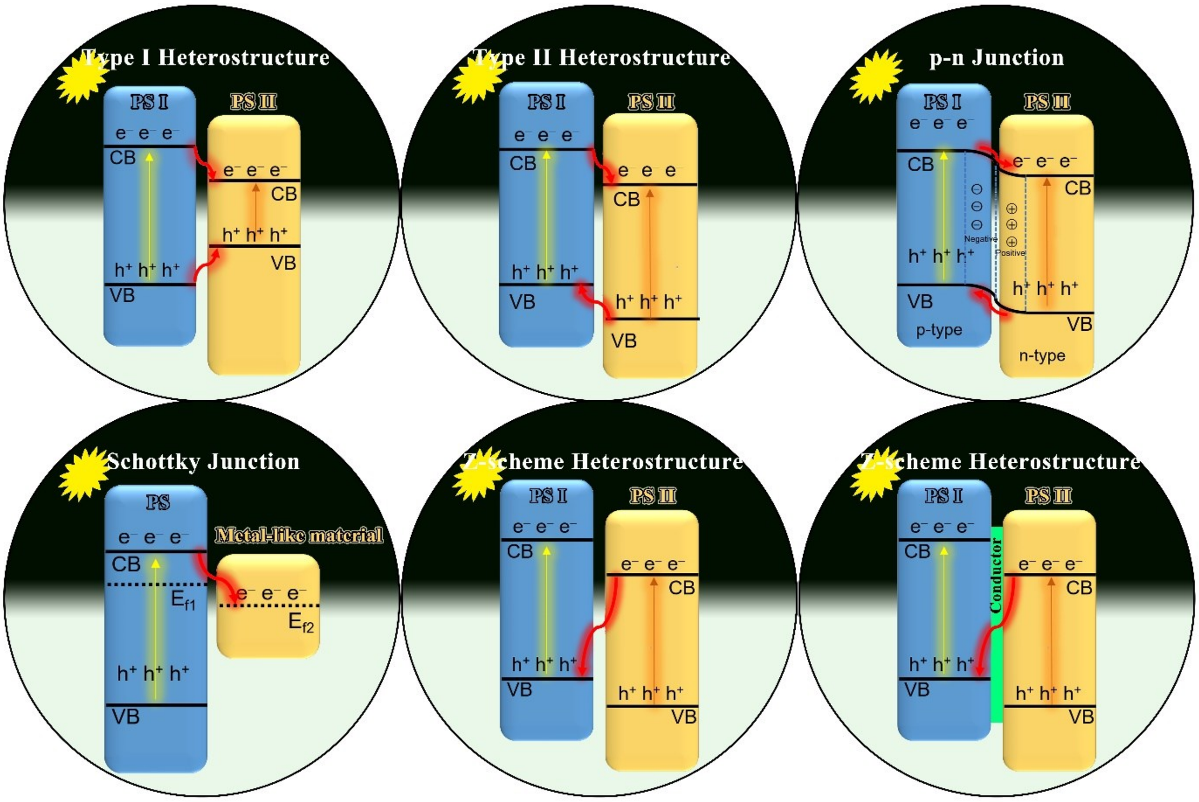

Figure 11. Schematic representation of the typical separation routes of charge carrier. Redrawn from Ref. [187] Copyright 2019 Elsevier.

In order to construct direct Z-scheme heterostructures, several key factors should be considered. Firstly, one of the semiconductors should possess a higher Fermi level, smaller work function, and higher CB and VB positions than the other one. Secondly, these heterojunctions are generally composed of a reduction photocatalyst and an oxidation photocatalyst.[185] Upon irradiation, in a typical Type–II heterojunction system, photo-generated holes transfer from the VB of PS II to that of PS I, while the photo-generated electrons move from the CB of PS I to that of PS II (Figure 11). When it comes to the direct Z-scheme heterostructures, the photo-induced electrons in PS II combine with the photo-induced holes in the VB of PS I. Thus, holes and electrons with higher oxidation and reduction potentials are accumulated in the VB of PS II and CB of PS I, respectively (Figure 11). This spatial separation of photo-generated e^-/h^+ pairs could improve redox capabilities.[180] Precipitation/deposition processes and immobilization of one component on the surface of another one, are effective methods to construct direct Z-scheme heterostructures. The effects of the formation of heterostructures are briefly explained in the following section by providing some examples.

4.3.1. Type I heterojunction

Jing et al. synthesized SnS_2-GCN composites using different morphologies of SnS_2 (3D flower-like, nanoparticles, and nanosheets) for photocatalytic H_2 generation under visible light irradiation. Among those, SnS_2-GCN nanocomposites produced by SnS_2 nanoparticles with no noble metal serving as co-catalyst showed the highest evolution rate of H_2, i.e. 6305.18 μmol h^{-1} g^{-1}, while the photocatalytic generation rate of H_2 over pure GCN (containing 3 wt% Pt) and SnS_2 nanoparticles (without Pt) was 106.82 and 371.27 μmol h^{-1} g^{-1}, respectively. The interaction between GCN and SnS_2 has been accounted for the low recombination rate and efficient charge transfer of photogenerated carriers in SnS_2-GCN nanocomposites, resulting in their promising photocatalytic activity. Noteworthy, The VB and CB positions of GCN could straddle those of SnS_2 nanoparticles when exposed to visible light, generating the Type I heterojunction.[189] Dong et al. synthesized GCN-GCN isotype heterostructures by using a composite precursor produced by mixing 6 g each of melamine and urea in water (30 mL) followed by heating at 550 °C for 3 h. Finally, a Type I GCN-GCN metal-free heterojunction was obtained where the photogenerated electrons could transport from the CB of the GCN synthesized by urea to that synthesized by melamine, but the photogenerated holes could not be transferred from one side to the other. It has been accounted for the improved separation of charge carriers, playing a direct role in the higher photocatalytic NO removal in air over GCN-GCN heterojunction than that over GCN synthesized by either melamine or urea (despite of the remarkably lower specific surface area of GCN-GCN heterojunction, 32 m^2 g^{-1}, than GCN synthesized by urea (91 m^2 g^{-1})).[190]

In fact, charge carriers are usually gathered on one semiconductor in the Type I heterostructures (upon light irradiation), whereas the spatial separation of charge carriers could by effectively achieved by the Type II heterostructures, providing considerable improvement of the photocatalytic activity.[187]

4.3.2. Type II heterojunction

The distinctive staggered band structures between the two semiconductors in Type II heterostructures may greatly improve the spatial separation of charge carriers. The internal field could finally encourage the charge carrier's separation and migration. Notably, appropriate band positions to separate charge carriers could be efficiently provided by Type II alignment. Due to the potential advantages of Type II heterostructures in photocatalysis, they are the most widely studied in the literature.[187] For instance, Rapit et al. synthesized GCN-MoS_2 heterostructures for the photocatalytic removal of phenol and Cr(VI). In detail, MoS_2-decorated GCN heterostructures (containing 0.5, 1, 3, and 10 wt% MoS_2) were synthesized by mixing colloidal solutions of bulk GCN (suspended in isopropanol) and MoS_2 nanoparticles (suspended in a water/isopropanol solution) followed by sonication, centrifuge, and calcination. Notably, MoS_2-decorated GCN heterojunctions showed higher photo absorption ability in the visible light region than bare GCN. The optimal nanocomposite (containing 1 wt% MoS_2 nanoparticles) exhibited superior efficiency than both MoS_2 and pristine C_3N_4 in photocatalytic reduction/oxidation processes under simulated solar light (through a Type II mechanism considering the scavenging experiments).[191] Kalidasan et al.

synthesized Nd-doped WO_3@GCN heterojunction (Type II) using a calcination method where GCN (0.86 g) was ground with Nd-doped WO_3 (0.144 g) followed by calcination at 450 °C for 2 h. The synthesized heterojunction showed lower recombination rate of charge carriers than both bare GCN and Nd-doped WO_3, and considerably higher photocatalytic activity (84.51%) for MB degradation than both pristine GCN and Nd-doped WO_3 (57.52% and 60.32%, respectively) under visible light irradiation after 2 h. The results were attributed to the tight contact at the assembly of the n-n heterostructure, facilitating the interfacial transfer of charge carriers between GCN and Nd-doped WO_3, and the appropriate light harvest.[192]

Overall, Type II heterostructures could provide a pathway for the effective spatial separation of charge carriers. Notably, the high apparent quantum efficiency of GCN-CeO_2 Type II heterojunction with rich oxygen vacancies, i.e. 17.1%, has been accounted for its higher photocatalytic CO_2 reduction than pristine GCN and CeO_2.[193] However, further improvement of the photocatalytic activity could be obtained using p-n heterostructures, combined by n-type and p-type semiconductors, providing an extra electrical field to facilitate the transfer of charge carries and accelerate the separation of charge carriers compared to that obtained by Type II heterostructures.[187]

4.3.3. p-n heterojunction

Generally, the location of Fermi level of n-type and p-type semiconductors is close to their CB and VB, respectively. It has been proposed that the holes could move from the p-type to the n-type semiconductor prior to light irradiation. Notably, the diffusion of charge carriers persists until an equilibrium condition is achieved in the Fermi level system. Finally, the effective separation of charge carriers could occur as the result of the formation of an electrical field at the interface of n-type and p-type semiconductors.[187] Ng et al. used Cu_2O and nitrogen-deficient GCN (as p-type and n-type semiconductors, respectively) to synthesize Cu_2O@g-

C_3N_{4-x} nanocomposites for the photocatalytic generation of H_2. Based on their estimation, the p-n junction could accelerate the directional transfer of charge carriers, due to the formation of electric field, and yield the accommodation of holes and electrons at separated positions of Cu_2O and nitrogen-deficient GCN, consecutively, improving the separation of charge carriers and increasing their lifetime where the optimal nanocomposite (containing 3wt% Cu_2O) exhibited 1.8 and 2.7 times higher photocatalytic H_2 generation rate than g-C_3N_{4-x} and Cu_2O, respectively. Noteworthy, g-C_3N_{4-x} showed much higher efficiency than bare g-C_3N_4 (227.3 against 129.7 μmol g^{-1} h^{-1}),[194] demonstrating the vital role of engineering defects in improvement of the photocatalytic activity of GCN as discussed previously. Liu et al. also used Cu_2O to synthesize Cu_2O-GCN heterostructures. GCN immobilized on the surface of Cu_2O formed a tight heterojunction. The built-in electric field generated at the interface of heterostructure has been accounted for the migration and effective separation of charge carriers. As the result, construction of the p-n heterostructure has been accounted for the considerably higher (3-7 times) quantum yield of Cu_2O-GCN than that obtained by the single counterparts.[195] However, pure GCN could suffer from its low quantum yield, resulting in lower photocatalytic activity compared to heterojunctions.[193] Overall, the 90.7% photocatalytic degradation of tetracycline over the optimal Cu_2O-GCN p-n heterostructure was significantly higher than that over single Cu_2O and GCN (39.5% and 47.8%, respectively).[195]

4.3.4. Schottky junction

The Schottky junction, generally composed of a semiconducting material and a metal-like material serving as co-catalyst, could be effectively used to construct a space-charge separation area. The formation of such a junction could initiate the fast movement of electrons from one component to the other at the interface of counterparts. Hence, the Fermi energy levels could be aligned and the separation of charge carriers is greatly improved, increasing photocatalytic activity.[187] Ni_2S,[196] MoB,[197] Co_2P,[198] and $Ti_3C_2T_x$ (MXenes)[199-202] are among numerous metal-like materials used for the construction of Schottky junctions. Notably, MXenes are new 2D nanostructure materials with the general formula of $M_{n+1}X_nT_x$ (n=1-3) where M, X, and T_x are early transition metals (Ta, Ti, Mo, Nb or V), nitrogen and/or carbon, and surface termination groups (including –F, –O, and –OH), respectively.[202] It should be noted that the terminal surface groups of MXene is capable of tuning its work function, enhancing the density of electrons on the surface.[199] Among MXene materials, Ti_3C_2 (titanium carbide) is considered a typical MXene has been extensively used as co-catalyst to promote photocatalytic activity due to its promising properties including acceptable structural stability, excellent metal-like conductivity, and high visible light harvest.[199-201]. Interestingly, Ti_3C_2 has been effectively used as a co-catalyst to achieve the high AQY of 40.1% at 420 nm and an extremely high HER rate of 14342 μmol h^{-1} g^{-1} by using CdS as the photocatalyst.[203] Noteworthy, the AQY (which is used to evaluate the photon conversion efficiency)[202] could be calculated using equation (8) in a photocatalytic HER:[202-205]

$$\mathrm{AQY}\,(\%) = \frac{\text{Number of reacted electrons}}{\text{Number of incident photons}} \times 100 = \frac{\text{Number of evolved } \mathrm{H_2} \text{ molecules} \times 2}{\text{Number of incident photons}} \times 100 \qquad (8)$$

In a case study, Sun et al. used $Ti_3C_2T_x$ to synthesize GCN-$Ti_3C_2T_x$ composites for efficient photocatalytic hydrogen production under visible light irradiation. To prepare the composites, bare GCN and black $Ti_3C_2T_x$ powders were physically mixed at different mass ratios using a mortar and pestle. Then, the composites were annealed at 200 °C in air or under nitrogen protection to modify the surface termination groups of Ti_3C_2. Notably, the presence of $Ti_3C_2T_x$ in the composites with 30% Ti_3C_2 (mass ratio of $Ti_3C_2T_x$ to GCN) increased the photo-absorption ability and reduced the recombination rate of charge carriers compared to bare GCN. Among different samples, the greatest photocatalytic H_2 generation obtained by the composite containing 190% Ti_3C_2 (mass ratio of Ti_3C_2 to GCN) annealed in air with the H_2 production rate of 88 μmol h^{-1} g^{-1}. To clarify the crucial effect of $Ti_3C_2T_x$, different amounts of Pt, as another co-catalyst, from 1% to 5% (H_2PtCl_6, mass ratio to GCN) were loaded on GCN where the highest photocatalytic activity was achieved at 3% Pt with the H_2 production rate of 56.2 μmol h^{-1} g^{-1} which was lower than that obtained by the addition of $Ti_3C_2T_x$. Notably, the AQY reached to 1.27% for the optimal GCN-$Ti_3C_2T_x$ composite. Overall, the addition of MXenes to GCN could increase HER rate by improving the separation of charge carriers, due to the negative shift of Fermi level, resulted by the accumulation of photogenerated electrons from GCN on Ti_3C_2 through the ohmic contact between metallic MXenes and GCN semiconductor. The dependency of various surface termination groups on the photocatalytic HER activity was estimated by density functional theory (DFT) calculations. The top and side views of the Ti_3C_2 structure are illustrated in Figure 12(a). The termination group sites on the Ti_3C_2 surface are represented by a (on top of the C atoms), b (over the surface of Ti atoms), and c (over the mid-layer Ti atoms). The –O and –F termination groups occupy the C sites, whereas the –OH termination groups are ignored since they are only indirectly related to the major step in the HER process. The –O and –F termination groups fill the C sites, whereas the –OH termination groups are ignored since they are not directly related to the primary step in the photocatalytic HER. DFT calculations exhibited that Ti_3C_2 with oxygen surface termination groups covered by H atoms (25%) provided the minimal free energy at 0.011 eV. Considering the experimental results, Ti_3C_2 with –O surface termination groups (as co-catalyst) provided the best photocatalytic activity confirmed by DFT calculations.[202]

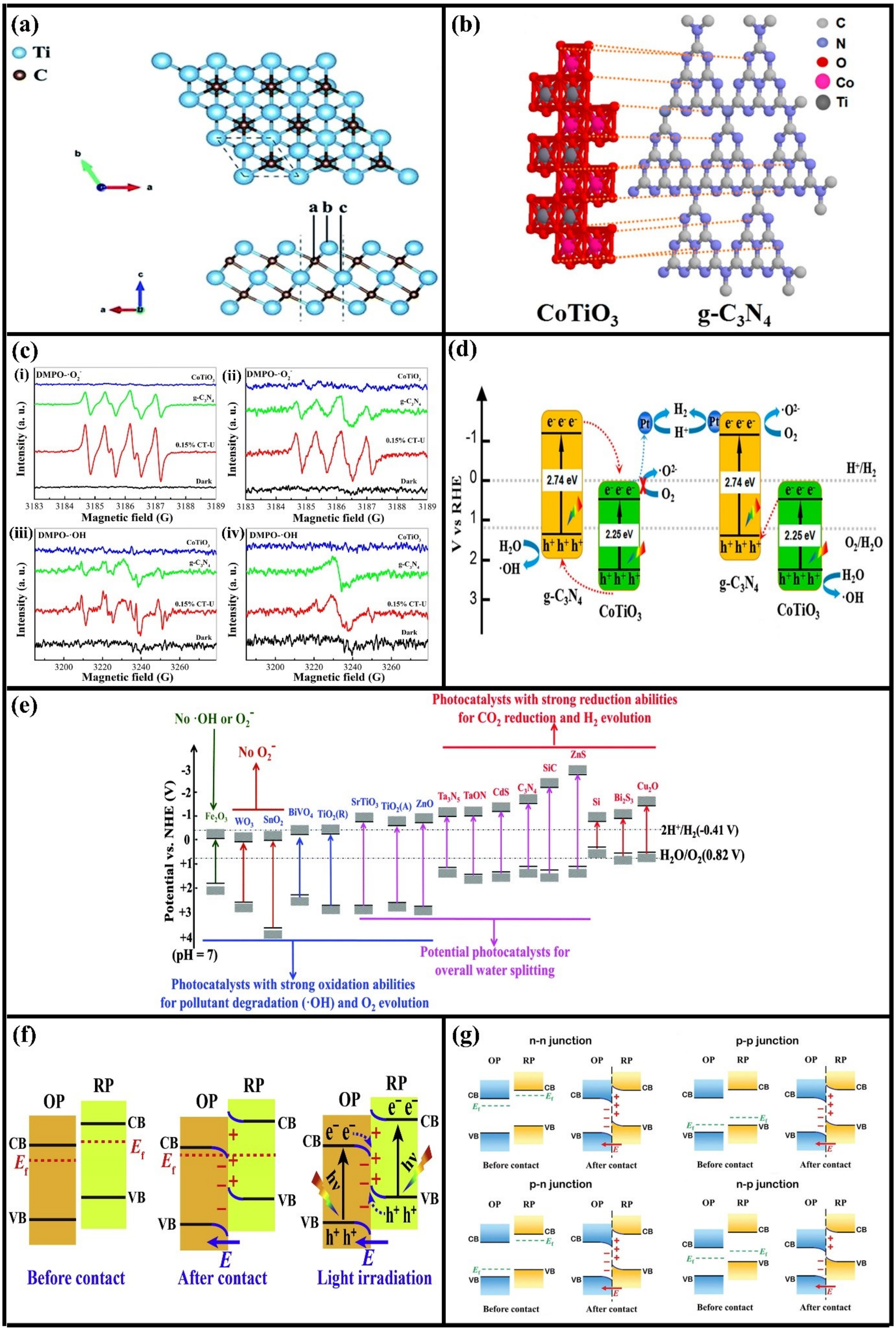
(a)
Ti
C
b
a
a b c
c
(b)
C
N
O
Co
Ti
CoTiO$_3$
g-C$_3$N$_4$
(c)
(i) DMPO-·O$_2^-$
(ii) DMPO-·O$_2^-$
(iii) DMPO-·OH
(iv) DMPO-·OH
CoTiO$_3$
g-C$_3$N$_4$
0.15% CT-U
Dark
Intensity (a. u.)
Magnetic field (G)
(d)
V vs RHE
2.74 eV
2.25 eV
H$^+$/H$_2$
O$_2$/H$_2$O
H$_2$O
·OH
O$_2$
·O^{2-}
H$_2$
H$^+$
Pt
g-C$_3$N$_4$
CoTiO$_3$
(e)
Photocatalysts with strong reduction abilities for CO$_2$ reduction and H$_2$ evolution
No ·OH or O$_2^-$
No O$_2^-$
Potential vs. NHE (V)
(pH = 7)
Fe$_2$O$_3$
WO$_3$
SnO$_2$
BiVO$_4$
TiO$_2$(R)
SrTiO$_3$
TiO$_2$(A)
ZnO
Ta$_3$N$_5$
TaON
CdS
C$_3$N$_4$
SiC
ZnS
Si
Bi$_2$S$_3$
Cu$_2$O
2H$^+$/H$_2$(-0.41 V)
H$_2$O/O$_2$(0.82 V)
Photocatalysts with strong oxidation abilities for pollutant degradation (·OH) and O$_2$ evolution
Potential photocatalysts for overall water splitting
(f)
OP
RP
CB
VB
E$_f$
E
hν
Before contact
After contact
Light irradiation
(g)
n-n junction
p-p junction
p-n junction
n-p junction
OP
RP
CB
VB
E$_f$
E
Before contact
After contact

Figure 12. (a) The top and side views of the Ti_3C_2 structure. Reproduced with permission from Ref. [202] Copyright 2018 The Royal Society of Chemistry (https://pubs.rsc.org/en/content/articlelanding/2018/TA/C8TA02706D). (b) Schematic interaction of tri-s-triazine GCN and $CoTiO_3$ via the generation of chemical bonds. Reprinted with permission from Ref. [206] Copyright 2016 American Chemical Society. (c) ESR signals of DMPO-$^{\bullet}O_2^-$ in methanol dispersion under (i) UV and (ii) visible light, and signals of DMPO-$^{\bullet}OH$ in aqueous dispersion under (iii) UV and (iv) visible light. Reprinted with permission from Ref. [206] Copyright 2016 American Chemical Society. (d) Comparing Type-II and Z-scheme charge carrier transfer routes for $COTiO_3$/GCN hybrid photocatalysts. Reprinted with permission from Ref. [206] Copyright 2016 American Chemical Society. (e) Potential applications and band positions of some particular semiconductors (pH = 7 in aqueous media). Reproduced with permission from Ref. [207] Copyright 2016 The Royal Society of Chemistry (https://pubs.rsc.org/en/content/articlelanding/2016/cs/c5cs00838g). (f) Schematic illustration of charge-transfer processes in S-scheme heterojunctions. Reprinted with permission from Ref. [208] Copyright 2020 Elsevier. This article has been published under an Elsevier user license (https://www.elsevier.com/about/policies/open-access-licenses/elsevier-user-license). (g) Four probable types of S-scheme heterojunctions. Reproduced with permission from Ref. [209] Copyright 2022 John Wiley and Sons.

4.3.5. Z-scheme heterojunction

As mentioned previously, construction of Type I, Type II, and p-n heterostructures could all be considered effective approaches to reduce the recombination rate of charge carries. However, on the downside, since reduction and oxidation reactions usually occur on the semiconducting material with lower reduction and oxidation potentials, respectively, the redox sites of above heterostructures are less active than their single counterparts, encouraging the application of Z-scheme heterojunctions with their unique properties in photocatalytic systems where both separation of charge carriers and high redox potentials could be achieved simultanously.[187, 210]

It is of high importance to carefully nominate PS I, PS II, and a redox electron mediator for the construction of artificial photosynthesis systems (traditional liquid-phase Z-scheme photocatalytic system as first generation Z-scheme heterostructures in which there is no direct contact between semiconductors) by imitating natural photosynthesis. Noteworthy, the electron acceptor-donor pair (A/D pair) could react with the photogenerated e^- and h^+ (in the CB of PS I and in the VB of PS II), respectively. Unfortunately, artificial Z-scheme systems suffer from several disadvantages including backward reactions, light absorption by the mediator that could adversely affect the amount of light absorbed by the semiconductors, and being used only for liquid phase reactions.[208, 210]

Hence, all-solid-state Z-scheme photocatalytic systems (or indirect Z-scheme photocatalytic systems) as second generation Z-scheme heterostructures (without the liquid A/D pair and by using a solid conductive medium connecting semiconductors) were proposed.[208, 210] Various materials including noble metal particles (such as Au, Pt, and Ag)[211-213] and carbon spheres[214] have been used as electron mediators in such Z-scheme systems. Although replacement of the shuttle ion pairs (used in traditional liquid-phase Z-scheme photocatalytic systems) by a solid conductive medium (used in all-solid-state Z-scheme photocatalytic systems) could broaden the application scope of Z-scheme systems, there are still several drawbacks.[209] Firstly, as shown in Figure 11, the reduction potential of electrons in PS I is higher than that in PS II, meanwhile, the oxidation potential of holes in PS II is higher than that in PS I. From thermodynamic viewpoint, it could facilitate the transfer of electrons from the CB of Semiconductor 1 to the VB of Semiconductor 2 (rather than what is proposed to be transferred from the CB of Semiconductor 2 to the VB of Semiconductor 1).[208, 209] Secondly, the proposed charge carrier route in all-solid-state Z-scheme systems could not be easily achieved by taking the CdS-Au-TiO_2 junction as an example where the photogenerated electrons in the CB of CdS and TiO_2 could migrate to Au (since it has the lowest Fermi level in this system), while simultaneously, a Schottky barrier could be formed due to the band bending at the interface of CdS/Au and Au/TiO_2, suppressing the electron flow from TiO_2 and CdS to Au.[208, 209] Thirdly, considering materials preparation, placing the conductor exactly in the interface of semiconductors is not easy.[208, 209] Fourthly, the conductor could compete with semiconductors to absorb light, leading to low light harvest.[208, 209]

Mediator-free Z-scheme systems, typically called direct Z-scheme photocatalytic systems, could initiate the direct transfer of charge carriers between the closely contacted semiconductors without a redox medium.[215] Hence, a higher photocatalytic activity is expected due to the shortened transmission distance. Overall, direct Z-scheme heterostructures could take unique advantages of the quick separation of charge carriers, cost-effectiveness (no need to expensive redox mediators), and good redox potential, resulting in their wide applications in either liquid or gas phase reactions (unlike the traditional liquid-phase Z-scheme photocatalytic systems which could be only used for the liquid phase reactions).[210] Ye et al. synthesized $CoTiO_3$-GCN hybrid photocatalysts using an in situ growth approach for the photocatalytic HER from water splitting. They mixed urea (10 g) and $CoTiO_3$ powders which were ground in an agate mortar where the weight ratios of $CoTiO_3$ to urea were 0.1, 0.15, 0.2, 0.3, 0.5, and 5 wt%. The composites, made of 2D GCN nanosheets and 1D $CoTiO_3$, were successfully produced by heating the resultant mixture at 500 °C for 2 h and 520 °C for another 2 h, followed by rinsing with water/ethanol and drying at 60 °C (in vacuum). Notably, before photocatalytic experiments, the as-synthesized samples were loaded by Pt (3 wt%) as co-catalyst. The optimal composite (weight ratio of $CoTiO_3$ to urea: 0.15%) yielded considerably higher photocatalytic H_2 generation rate (858 $\mu mol\ h^{-1}\ g^{-1}$) than pure GCN (422 $\mu mol\ h^{-1}\ g^{-1}$) under artificial sunlight irradiation. It also provided superior H_2 generation rate than pure GCN under visible light irradiation (22.2 μmol h^{-1} g^{-1} against 16.6 μmol h^{-1} g^{-1}) which could be related to the close interfacial contact and heterojunction interaction between $CoTiO_3$ and GCN. Figure 12(b) shows the schematic interaction of tri-s-triazine GCN and $CoTiO_3$ via the generation of chemical bonds. These interactions, which involve chemical bonds like Co−O−N or Ti− O−N, have been integrated using XPS data. Notably, the optimal hybrid photocatalyst yielded the apparent quantum efficiencies of 3.23% and 38.4% at 420 ± 20 nm and 365 nm, respectively, which were remarkably higher than that obtained by pure GCN (0.83% and 16.0% at 420 ± 20 nm at 365 nm, respectively). The generation of $^{\bullet}O_2^-$ and $^{\bullet}OH$ radicals over the optimal nanocomposite and pure GCN irradiated by both UV and visible light were compared using electron spin resonance (ESR) analysis. Overall, as shown in Figure 12(c), the intensity of $^{\bullet}O_2^-$ and $^{\bullet}OH$ signals for the hybrid photocatalyst was clearly higher than that for pure GCN, clarifying that using the hybrid photocatalyst could improve the generation of $^{\bullet}O_2^-$ and $^{\bullet}OH$ radicals. The probable mechanisms for the separation of charge carriers over $CoTiO_3$-GCN hybrid photocatalyst are compared in Figure 12(d). By considering Type II heterojunction as the mechanism of charge separation, the formation of $^{\bullet}O_2^-$ and H_2 could be hindered (without Pt co-catalyst). Furthermore, the oxidizability of holes will decrease by their transfer to the VB of GCN. Hence, Type II heterojunction was unfavorable for the generation of active species over $CoTiO_3$-GCN hybrid photocatalyst. Overall, considering the results of photocatalytic activity and ESR analysis, direct Z-scheme heterojunction has been considered the probable charge carriers transfer route. Notably, compared with pure GCN, the recombination rate of charge carriers increased by using the optimal composite as confirmed by the PL spectra. Hence, the interfacial recombination of holes from the VB of GCN and electrons from the CB of $CoTiO_3$ has been facilitated, boosting the effective separation of charge carriers and increasing the redox potentials responsible for the improved H_2 generation.[206] However, it should be noted that the mechanism for the electron transfer in direct Z-scheme heterojunctions (as the third generation of Z-scheme systems) is still unclear since the initial generations of Z-scheme systems (i.e. traditional liquid-phase and all-solid-state) could be considered problematic and not mature (direct Z-scheme heterojunctions could be considered from all-solid-state Z-scheme systems).[208]

4.3.6. S-scheme heterojunction

Type-II and Z-scheme heterojunctions have been nominated as the probable charge carriers transfer routes in hundreds of publications, while they both could suffer from several shortcomings. For instance, thermodynamically, the transfer mechanism of charge carriers in Type-II heterostructures reduces the redox potential, which is not favored in photocatalysis. In addition, from dynamics point of view, the proposed pathway could be hindered by the repulsion of similar charge carries (i.e. h^+/h^+ and e^-/e^-). Moreover, considering the energy usage, some energy (VB or CB energy difference in each photocatalyst counterpart) is lost without participating in photocatalytic reactions (Figure 11). Overall, the proposed charge transfer route in Type-II heterostructures needs further clarification.[209]

To overcome the drawbacks of Type-II heterojunctions, while combining extensive research in Z-scheme photocatalytic systems, S-scheme heterojunctions have been proposed by Fu et al. as a new concept to clarify the probable route of charge carriers in heterostructures.[208, 216] Considering the band positions, semiconductors are divided to reductive and oxidative photocatalysts (RP and OP) with more negative CB positions and more positive VB positions, respectively,[207] as illustrated in Figure 12(e). S-scheme heterojunctions are usually made of oxidative and reductive semiconductors with staggered band structures which are comparable to Type-II heterojunctions, but the charge transfer pathways are totally different. It has been proposed that not all the photogenerated charge carriers contribute to the photocatalytic reactions. Notably, in S-scheme heterojunctions, idle photogenerated e^- and h^+

are recombined whereas the powerful ones are held in the CB of RP and the VB of OP, respectively.[208] The "S" figure-like transfer pathway of the photogenerated e^-/h^+ pairs at the interface of S-scheme heterojunctions could provide the highest redox potential.[217] Schematic illustration of charge transfer pathways in S-scheme heterojunctions is shown in Figure 12(f). Such a charge transfer route could be driven by three major factors as follows:[208]

i. Internal electric field:

   After close contact of semiconductors, due to the higher Fermi level of reductive photocatalyst than oxidative photocatalyst (as shown in Figure 12(f)), electrons in the RP are inclined to diffuse to the OP spontaneously, resulting in the formation of layers depleted from electrons in the RP and accumulated by electrons in the OP. Consequently, an internal electric field is formed at the junction, directed from the RP to OP, accelerating the transfer of photogenerated e^- from the OP to RP.[208]

ii. Band bending:

   After close contact of semiconductors to align Fermi energy, Fermi levels of the RP and OP shift oppositely (downward and upward, respectively). Band bending encourages the recombination of photogenerated e^- (in the CB of OP) and h^+ (in the VB of RP) at the junction.[208]

iii. Coulombic attraction:

   After close contact of semiconductors, the recombination of photogenerated e^- (in the CB of OP) and h^+ (in the VB of RP) at the junction is likely due to the Coulombic attraction between e^- and h^+.[208]

Overall, charge transfer pathways in S-scheme photocatalytic systems are basically different from those for Type-II and Z-scheme systems, as evidenced both theoretically and experimentally.[208] Similar to other types of heterojunctions, S-scheme systems also have some limitations. Firstly, they are mainly for powder photocatalysts, while not applying to photoelectrochemical processes using an external circuit. Secondly, the photocatalyst counterparts are mainly n-type semiconductors and should have considerable Fermi level differences and appropriate band structures.[208] However, from a more general viewpoint, S-scheme heterostructures could be constructed by a p-type or an n-type semiconductor once a comprehensive requirement is satisfied. The specific requirement is that the Fermi level and CB of OP should be lower than those of RP at the same time (OP or RP could be either p-type or n-type semiconductors).[209] All such probabilities for the constriction of S-scheme heterostructures are shown in Figure 12(g). Recently, ex/in situ irradiated XPS, EPR, and AFM (with potential mode) characterization techniques have been effectively used to confirm the formation of S-scheme photocatalytic systems.[208]

Kisch et al. suggested that only quantum yields (not rate constants) could be compared in either heterogeneous or homogeneous photochemical reactions.[218] The adjustment of structure and/or morphology is considered an effective approach to improve the quantum efficiency.[145] The effects of wavelength and modification of GCN structure (by either element doping or production of heterostructures) on AQY of the photocatalytic H_2 production or pollutant degradation are shown in Table 4. For instance, S doping increased the AQY from 4.06% for bare GCN to 10.2% for S-doped GCN. Meanwhile, the heterojunction composed of B-doped GCN nanodots and S-doped GCN nanosheets increased the AQY to 22.7%,[150] clarifying the crucial role of both element doping and fabrication of heterojunctions in improving AQY. It is also obvious that the AQY of H_2 production/pollutant removal is highly dependent on wavelength, due to the relationship between photo-absorption ability and wavelength.[145]

Table 4. Effects of wavelength and modification of GCN structure on AQY.

Modification method of g-C_3N_4	**AQY (%)**		**Wavelength (nm)**	**Light intensity**	**Reference**
	Bare g-C_3N_4	**Modified g-C_3N_4**			
S doping	4.06	10.2	420	1.6 mW cm^{-2}	150
Heterojunction (B-doped GCN/S-doped GCN)	4.06	22.7	420	1.6 mW cm^{-2}	150
P doping	-	4.32	420	4.1 mW cm^{-2}	145
P doping	-	3.58	450	3.5 mW cm^{-2}	145
P doping	-	1.28	500	4.3 mW cm^{-2}	145
Heterojunction (Ag/g-C_3N_4)	10.7×10^{-4}	14.3×10^{-4}	-	-	219
S doping	$\sim 0.03^{*}$	$\sim 0.39^{*}$	420	-	151
Heterojunction (V_2O_5/N-deficient g-C_3N_4)	-	6.5	420	100 mW cm^{-2}	220
Heterojunction (V_2O_5/N-deficient g-C_3N_4)	-	5.1	460	100 mW cm^{-2}	220
Heterojunction (V_2O_5/N-deficient g-C_3N_4)	-	0.5	500	100 mW cm^{-2}	220
Heterojunction (g-C_3N_4/SnO_2)	4.44×10^{-4}	5.73×10^{-4}	-	-	221
Heterojunction (g-C_3N_4/Ti_3C_2)	0.141	3.654	-	-	222

Heterojunction (Co_3O_4/g-C_3N_4)	0	0.053	420	-	223
P doping	0.66	1.78	420	-	224
Heterojunction (ReS_2/g-C_3N_4)	-	4.10	365	31.81 mW cm^{-2}	225
Heterojunction (ReS_2/g-C_3N_4)	-	2.82	420	22.30 mW cm^{-2}	225
Heterojunction (ReS_2/g-C_3N_4)	-	1.17	450	19.10 mW cm^{-2}	225
Heterojunction (ReS_2/g-C_3N_4)	-	0.29	485	15.77 mW cm^{-2}	225
Heterojunction (ReS_2/g-C_3N_4)	-	0	535	6.92 mW cm^{-2}	225

*: Extracted from the publication by Plot Digitizer

4.4. Applying a bias potential for pollutant degradation

The recombination of charge carriers is a vital factor affecting the efficiency of semiconducting materials in PC applications. It is well understood that the modification of PC systems by the addition of electrochemical systems can significantly increase the efficiency of PC systems by controlling the redox reactions occurring separately at the anode and cathode.[226, 227] Noteworthy, applying a bias potential could provide a driving force to accelerate the transfer of photogenerated electrons from the photoanode to the cathode through the external circuit, promoting the separation efficiency of the photogenerated electron-hole pairs in photoelectrocatalytic (PEC) processes. Therefore, the aggregated effects of electrocatalytic (EC) and PC processes could result in the higher efficiency of PEC process than both conventional EC and PC processes.[228] Furthermore, PEC process can not only increase the efficiency, but also enhance the decomposition capacity of recalcitrant pollutants.[229] Overall, PEC system is known as an efficient, promising, sustainable, and environmentally friendly process (without secondary pollution) for decomposition of organic pollutants in aqueous solution.[226, 230] Hence, PEC process has found applications in water splitting[231] and solar cells[232] (in addition to photocatalysis). The photocatalytic and PEC activity of some composites synthesized by the addition of GCN for decomposition of various organic pollutants is compared in Table 5. The results demonstrate that the PEC process yielded a higher efficiency than PC process in all cases.

In a typical PEC system, the semiconducting material is immobilized on a conductive substrate which serves as the photoanode.[229] Various photoanodes have been produced using TiO_2,[233] $ZnFe_2O_4$,[234] ZnO,[235] $BiVO_4$,[236] $MoSe_2$,[237] PbO_2,[238] and graphite[239] for H_2 generation or the degradation of organic pollutants. Considering the synergetic effect of PC and EC, using photoanodes with appropriate band gap energies and suitable charge-carrier conductivities is desired to achieve high PEC performances.[240, 241] Besides, using visible-light activated photoanodes with high stability is desired.[242] Owing to its unique properties, g-C_3N_4 has recently gained wide attention for the production of the photoanodes to promote the degradation efficiency of organic pollutants.

Table 5. Comparison of photocatalytic and photoelectrocatalytic activity of the GCN composites for the degradation of organic pollutants.

Photoelectrode	**Pollutant (concentration)**	**Source of light**	**Photoelectrocatalytic activity**	**Photocatalytic activity**	**Reference**
PbO_2/GCN	Reactive brilliant blue KN-R (60 mg/L)	175 W Xe lamp	~91% (120 min)	~18% (120 min)	[243]
CQDs/GCN	Methylene blue (5 mg/L)	500 W Xe lamp	97.2% (180 min)	57.02% (180 min)	[228]
GCN/TiO_2	Phenol (5 mg/L)	500 W Xe lamp	~99% (150 min)	~26% (150 min)	[244]
GCN/TiO_2	Tetracycline (10 mg/L)	300 W Xe lamp	95% (60 min)	65% (60 min)	[229]
Fe_2O_3/GCN	Clofibric acid (30 mg/L)	NA	99.7% (300 min)	40.6% (300 min)	[230]
GCN/$BiVO_4$	Diclofenac sodium (10 mg/L)	300 W Xe lamp	31.2% (120 min)	7.0% (120 min)	[240]
POM/GCN	Rhodamine B (NA)	NA	88.2% (120 min)	23.2% (120 min)	[241]
TiO_2/GCN/CQDs	1,4-dioxane (10 mg/L)	LED lamps	78.0% (360 min)	33.2% (360 min)	[245]
TiO_2/GCN	1,4-dioxane (10 mg/L)	LED lamps	~49% (360 min)	~23% (360 min)	[245]
Co_3O_4/GCN	Clofibric acid (30 mg/L)	300 W Xe lamp	95.3% (360 min)	~6% (360 min)	[242]

Note: POM (polyoxometalate)

Li et al. evaluated the effect of the addition of GCN to PbO_2 on the PC and PEC degradation of reactive brilliant blue KN-R. The PC and PEC degradation percentages of brilliant blue KN-R over the PbO_2 photoanode were 8% and 63%, respectively, while the PC and PEC degradation percentages of brilliant blue KN-R over the GCN-modified PbO_2 photoanode were 18% and 91%, respectively. Firstly, PEC process exhibited much higher efficiency than PC process over both photoanodes. Secondly, the introduction of GCN into PbO_2 film has significantly improved the degradation efficiency of KN-R in both PC and PEC processes that was attributed to the change of morphology, hydrophobicity, and surface hydrophilicity of the electrodes which improve the photoelectrochemical active sites. Furthermore, GCN improved the carrier density and oxygen evolution potential of PbO_2 film.[243] Wang et al. fabricated GCN-wrapped TiO_2 nanotube arrays for phenol degradation under simulated sunlight. The as-prepared photoanode showed promising PEC activity which was related to the improved light harvesting and separation efficiency of charge carriers originated from the introduction of g-C_3N_4 to TiO_2. Compared to pure TiO_2, the optimum amount of GCN resulted in a 4-fold increase in the photocurrent density.[244]

In addition to heterojunction structures, the decoration of GCN with conductive materials is another approach which can significantly improve PEC activity. Recently, carbon quantum dots (CQDs) have received considerable attention duo to good biocompatibility, unique electrical conductivity, reliable stability, low toxicity, excellent up-converted photoluminescence feature, chemical inertness, suitable catalytic and optical properties, and easy functionalization.[246-248] Specifically, due to its unique electron-accepting and donating properties, it is considered a potential photosensitizer for the production of semiconductor nanocomposites with efficient capability of separation of charge carriers.[246] Zhang et al. fabricated g-C_3N_4 nanosheets decorated with CQDs for PEC degradation of MB. SEM and EDX mapping images of the optimal CQDs/GCN nanocomposite are shown in Figure 13(a).

Notably, the uniform distribution of O and C elements clarify well decoration of GCN with CQDs. Photo-absorption ability and PL spectra of CQDs/GCN nanocomposites are illustrated in Figures 13(b) and 13(c), respectively. As evident, all CQDs/GCN nanocomposites exhibited significantly superior visible-light harvest than GCN. Furthermore, the PL intensity of the optimal CQDs/GCN nanocomposite is remarkably lower than that of GCN. Moreover, the optimal CQDs/GCN nanocomposite exhibited strong florescence up-conversion properties. The modified properties resulted in the significantly higher PEC activity of the optimal CQDs/GCN nanocomposite (97.2%) than GCN (11.1%) for the decomposition of MB. Noteworthy, the PC activity of the nanocomposite was 57.02% that signifies the crucial role of the applied bias potential on degradation of organic pollutants.[228]

In another research, Su et al. used GCN to improve the PEC degradation of 1,4-dioxane over TiO_2 nanorod arrays. Further improvement was carried out by the decoration of the TiO_2/GCN film with CQDs. Notably, TiO_2/GCN/CQDs (TCNC NRAs) showed narrower band gap energy and longer lifetime of photogenerated charge carries than both TiO_2 nanorod arrays (TiO_2 NRAs) and TiO_2/GCN nanorod arrays (TCN NRAs). PL spectra of GCN, TiO_2 NRAs, TCN NRAs, and TCNC NRAs are compared in Figure 13(d), clarifying the low recombination rate of charge carries for TCNC NRAs. In addition, compared to TiO_2 NRAs and TCN NRAs, TCNC NRAs exhibited much higher photo-current responses (Figure 13(e)). The corresponding EIS Nyquist plots are shown in Figure 13(f). The arc radius of TiO_2 NRAs was larger than that of TCN NRAs and TCNC NRAs under both dark condition and visible-light irradiation, indicating faster electrode reactions and easier transfer of electrons on the fabricated photoanodes in the order of TCNC>TCN>TiO_2 nanorod arrays. PEC, EC, and PC activity of these photoanodes for the degradation of 1,4-dioane is compared in Figure 13(g). As evident, PEC process was more efficient than both EC and PC processes over all photoanodes. Besides, the introduction of GCN to TiO_2 followed by decoration with CQDs remarkably improved the degradation efficiency of 1,4-dioane in both PEC and PC processes. These findings clearly show the crucial role of recombination rate of charge carriers in the higher efficiency of PEC than PC process, and in the improved degradation efficiency of 1,4-dioxane over TiO_2/GCN/CQDs nanocomposites.[245] Zhang et al. constructed Co_3O_4/GCN photoanodes for the degradation of clofibric acid. Photo-adsorption ability, PL spectra, and photo-current response of bare GCN and Co_3O_4/GCN nanocomposites with different amounts of Co_3O_4 from 2% to 15%, relative to melamine used for synthesis of GCN, are shown in Figures 13(h), 13(i) and 13(j), respectively. Overall, the introduction of Co_3O_4 increased both photo-adsorption ability and photo-current response, and decreased PL intensity compared with bare GCN. Noteworthy, both higher photo-adsorption ability and lower recombination rate of charge carriers were responsible for the superior PEC activity of the optimal nanocomposite (15%-Co_3O_4/GCN) than that of GCN for the degradation of clofibric acid. The effect of applying different bias potentials on the PEC activity of 15%-Co_3O_4/GCN nanocomposite is shown in Figure 13(k). It is evident that the more the bias voltage, the higher the degradation efficiency was obtained which was related to the reduced recombination rate of charge carriers at increased bias potentials (up to 2 V). Further increase of the voltage from 2 V to 2.5 V did not significantly affect the PEC degradation of clofibric acid due to the saturated efficiency of charge separation at 2 V.[242]

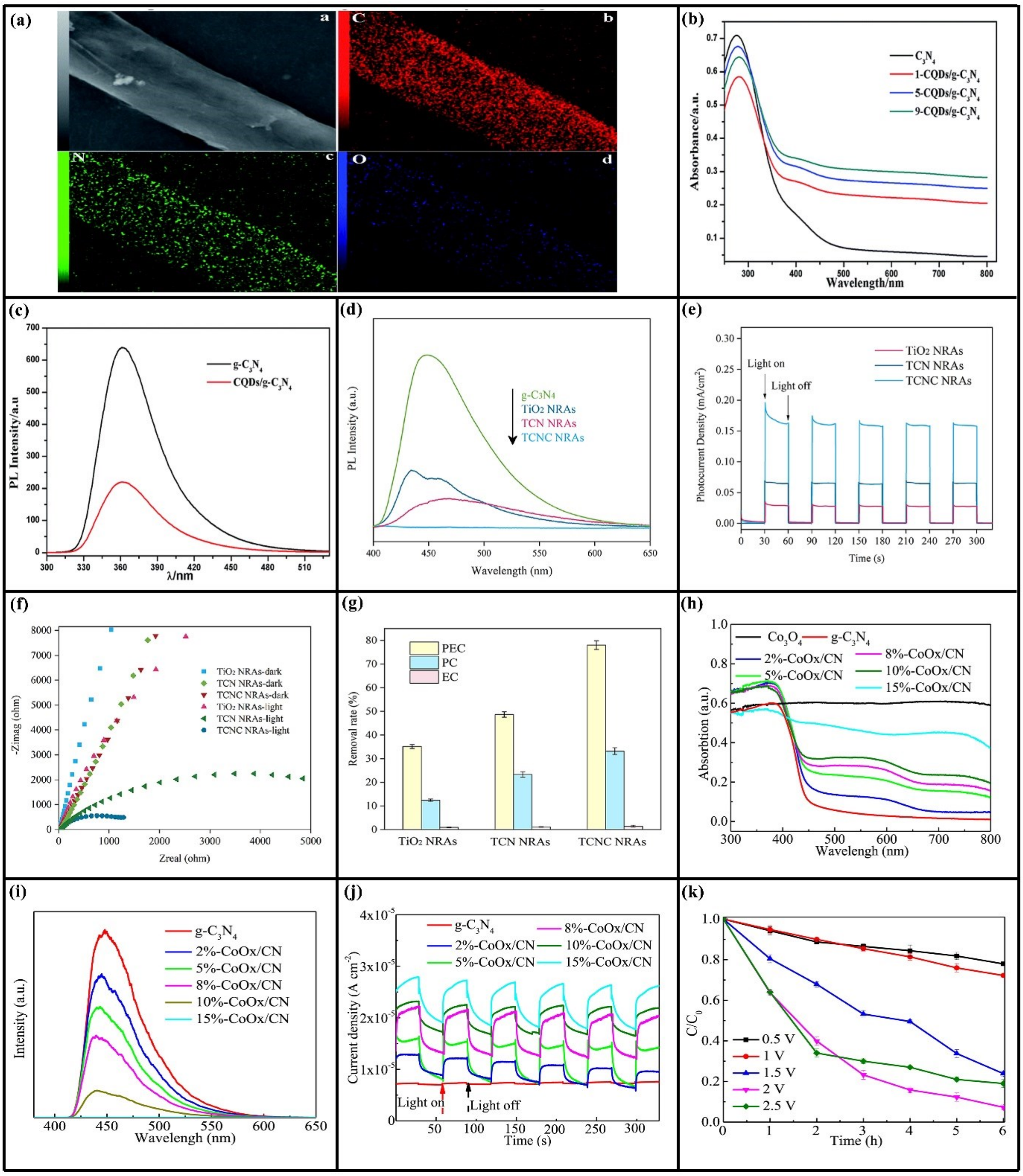

Figure 13. (a) SEM and EDX mapping images of the CQDs/GCN nanocomposite. Reproduced with permission from Ref. [228] Copyright 2017 The Royal Society of Chemistry (https://pubs.rsc.org/en/content/articlelanding/2017/ra/c7ra11205j). This article is licensed under a Creative Commons Attribution-NonCommercial 3.0 Unported Licence (https://creativecommons.org/licenses/by-nc/3.0/). (b) UV-vis diffuse reflectance of the CQDs/GCN nanocomposites and bare GCN. Reproduced with permission from Ref. [228]

Copyright 2017 The Royal Society of Chemistry (https://pubs.rsc.org/en/content/articlelanding/2017/ra/c7ra11205j). This article is licensed under a Creative Commons Attribution-NonCommercial 3.0 Unported Licence (https://creativecommons.org/licenses/by-nc/3.0/). (c) PL spectra of the CQDs/GCN nanocomposites and bare GCN. Reproduced with permission from Ref. [228] Copyright 2017 The Royal Society of Chemistry (https://pubs.rsc.org/en/content/articlelanding/2017/ra/c7ra11205j). This article is licensed under a Creative Commons Attribution-NonCommercial 3.0 Unported Licence (https://creativecommons.org/licenses/by-nc/3.0/). (d) PL spectra of TiO_2 NRAs, TCN NRAs, and TCNC NRAs. Reprinted with permission from Ref. [245] Copyright 2020 Elsevier. (e) Photo-current response of TiO_2 NRAs, TCN NRAs, and TCNC NRAs. Reprinted with permission from Ref. [245] Copyright 2020 Elsevier. (f) EIS Nyquist plots of TiO_2 NRAs, TCN NRAs, and TCNC NRAs. Reprinted with permission from Ref. [245] Copyright 2020 Elsevier. (g) PC, EC, and PEC activity of TiO_2 NRAs, TCN NRAs, and TCNC NRAs. Reprinted with permission from Ref. [245] Copyright 2020 Elsevier. (h) Photo-adsorption ability of bare GCN and Co_3O_4/GCN nanocomposites. Reprinted with permission from Ref. [242] Copyright 2021 Elsevier. (i) PL spectra of bare GCN and Co_3O_4/GCN nanocomposites. Reprinted with permission from Ref. [242] Copyright 2021 Elsevier. (j) Photo-current response of bare GCN and Co_3O_4/GCN nanocomposites. Reprinted with permission from Ref. [242] Copyright 2021 Elsevier. (k) Effects of different bias potentials on the PEC activity of 15%-Co_3O_4/GCN nanocomposite. Reprinted with permission from Ref. [242] Copyright 2021 Elsevier.

5. Conclusions and future perspectives

With unique physical, chemical and electronic properties, g-C_3N_4 is a promising semiconductor for photocatalytic applications especially under visible light irradiation. Among different methods used for the synthesis of g-C_3N_4, thermal polymerization is considered a promising approach owing to its advantages such as simplicity, low cost, and absence of impurities. Notably, ammonium salts could be effectively used for the simultaneous synthesis of GCN nanosheets and element doping. Although immobilization might reduce the specific surface area, the immobilized catalysts can be effectively used as the photoanode in photoelectrocatalysis with its superior efficiency than either electrocatalysis or photocatalysis for pollutant remediation due to the significantly reduced recombination rate of charge carriers. In addition, some major drawbacks of photocatalysis such as the agglomeration of the photocatalysts and the issues relating to their recovery could be resolved.

Further research should explore industrial and cost-effective methods to synthesize and deposit GCN composites, which is essential to bridge the gap between laboratory experiments and commercial-scale applications of photocatalysis. Great research opportunities also exist in using ammonium salts for the large-scale production of elements-doped GNC nanosheets, followed by defect engineering and decoration with economical and promising metal oxides to fabricate S-scheme heterostructures, which can be used for efficient photocatalytic H_2 generation and degradation of emerging and persistent organic pollutants in different environments.

Acknowledgements

This work is supported by the University Technology Sydney.

Conflict of Interest

The authors declare no conflict of interest.

References

1. Zhang, Y.; Heo, Y.-J.; Lee, J.-W.; Lee, J.-H.; Bajgai, J.; Lee, K.-J.; Park, S.-J. Photocatalytic Hydrogen Evolution via Water Splitting: A Short Review. *Catalysts* 2018, 8 (12), 655.

2. Kumaravel, V.; Imam, M. D.; Badreldin, A.; Chava, R. K.; Do, J. Y.; Kang, M.; Abdel-Wahab, A. Photocatalytic Hydrogen Production: Role of Sacrificial Reagents on the Activity of Oxide, Carbon, and Sulfide Catalysts. *Catalysts* 2019, 9 (3), 276.

3. Salzl, S.; Ertl, M.; Knör, G. Evidence for Photosensitised Hydrogen Production from Water in the Absence of Precious Metals, Redox-Mediators and co-Catalysts. *Phys. Chem. Chem. Phys.* 2017, 19 (12), 8141-8147.

4. Tao, X.; Zhao, Y.; Wang, S.; Li, C.; Li, R. Recent Advances and Perspectives for Solar-Driven Water Splitting Using Particulate Photocatalysts. *Chem. Soc. Rev.* 2022, 51 (9), 3561-3608.

5. Sahu, A. K.; Zhao, X. S.; Upadhyayula, S. Ceria-Based Photocatalysts in Water-Splitting for Hydrogen Production and Carbon Dioxide Reduction. *Catal. Rev.* 2023, 1-78.

6. Seckler, D.; Barker, R.; Amarasinghe, U. Water Scarcity in the Twenty-first Century. *Int. J. Water Resour. Dev.* 1999, 15 (1-2), 29-42.

7. Navidpour, A. H.; Hosseinzadeh, A.; Huang, Z.; Li, D.; Zhou, J. L. Application of Machine Learning Algorithms in Predicting the Photocatalytic Degradation of Perfluorooctanoic Acid. *Catal. Rev.* 2022, 1-26.

8. Ong, C. B.; Ng, L. Y.; Mohammad, A. W. A Review of ZnO Nanoparticles as Solar Photocatalysts: Synthesis, Mechanisms and Applications. *Renew. Sustain. Energy Rev.* 2018, 81, 536-551.

9. Chen, C. Q.; Zheng, L.; Zhou, J. L.; Zhao, H. Persistence and Risk of Antibiotic Residues and Antibiotic Resistance Genes in Major Mariculture Sites in Southeast China. *Sci. Total Environ.* 2017, 580, 1175-1184.

10. Tao, X.; Zhao, Y.; Wang, S.; Li, C.; Li, R. Correction: Recent Advances and Perspectives for Solar-Driven Water Splitting Using Particulate Photocatalysts. *Chem. Soc. Rev.* 2022, 51 (24), 10120-10122.

11. Paździor, K.; Bilińska, L.; Ledakowicz, S. A Review of the Existing and Emerging Technologies in the Combination of AOPs and Biological Processes in Industrial Textile Wastewater Treatment. *Chem. Eng. J.* 2019, 376, 120597.

12. Lama, G.; Meijide, J.; Sanromán, A.; Pazos, M. Heterogeneous Advanced Oxidation Processes: Current Approaches for Wastewater Treatment. *Catalysts* 2022, 12 (3), 344.

13. Sabri, M.; Habibi-Yangjeh, A.; Rahim Pouran, S.; Wang, C. Titania-Activated Persulfate for Environmental Remediation: The-State-of-the-Art. *Catal. Rev.* 2023, 65 (1), 118-173.

14. Coenen, T.; Logist, F.; Van de Moortel, W.; Luyten, J.; Van Impe, J.; Degrève, J. Geometry Optimization of Photochemical Reactors for Advanced Oxidation Processes. In *Computer Aided Chemical Engineering*, Kraslawski, A.; Turunen, I., Eds. Elsevier: 2013; Vol. 32, pp 829-834.

15. Deng, Y.; Zhao, R. Advanced Oxidation Processes (AOPs) in Wastewater Treatment. *Curr. Pollut. Rep.* 2015, 1 (3), 167-176.

16. Priyadarshini, M.; Das, I.; Ghangrekar, M. M.; Blaney, L. Advanced Oxidation Processes: Performance, Advantages, and Scale-up of Emerging Technologies. *J. Environ. Manage.* 2022, 316, 115295.

17. Parrino, F.; Loddo, V.; Augugliaro, V.; Camera-Roda, G.; Palmisano, G.; Palmisano, L.; Yurdakal, S. Heterogeneous Photocatalysis: Guidelines on Experimental Setup, Catalyst Characterization, Interpretation, and Assessment of Reactivity. *Catal. Rev.* 2019, 61 (2), 163-213.

18. Zhu, S.; Wang, D. Photocatalysis: Basic Principles, Diverse Forms of Implementations and Emerging Scientific Opportunities. *Adv. Energy Mater.* 2017, 7 (23), 1700841.

19. Wen, J.; Xie, J.; Chen, X.; Li, X. A Review on g-C_3N_4-Based Photocatalysts. *Appl. Surf. Sci.* 2017, 391, 72-123.

20. Ohtani, B. Preparing Articles on Photocatalysis-Beyond the Illusions, Misconceptions, and Speculation. *Chem. Lett.* 2008, 37, 216-229.

21. Navidpour, A. H.; Abbasi, S.; Li, D.; Mojiri, A.; Zhou, J. L. Investigation of Advanced Oxidation Process in the Presence of TiO_2 Semiconductor as Photocatalyst: Property, Principle, Kinetic Analysis, and Photocatalytic Activity. *Catalysts* 2023, 13 (2), 232.

22. Navidpour, A. H.; Kalantari, Y.; Salehi, M.; Salimijazi, H. R.; Amirnasr, M.; Rismanchian, M.; Azarpour Siahkali, M. Plasma-Sprayed Photocatalytic Zinc Oxide Coatings. *J. Therm. Spray Technol.* 2017, 26 (4), 717-727.

23. Navidpour, A. H.; Fakhrzad, M.; Tahari, M.; Abbasi, S. Novel Photocatalytic Coatings Based on Tin Oxide Semiconductor. *Surf. Eng.* 2019, 35 (3), 216-226.

24. Navidpour, A. H.; Fakhrzad, M. Photocatalytic Activity of Zn_2SnO_4 Coating Deposited by Air Plasma Spraying. *Appl. Surf. Sci. Adv.* 2021, 6, 100153.

25. Fakhrzad, M.; Navidpour, A. H.; Tahari, M.; Abbasi, S. Synthesis of Zn_2SnO_4 Nanoparticles Used for Photocatalytic Purposes. *Mater. Res. Express* 2019, 6 (9), 095037.

26. Navidpour, A. H.; Salehi, M.; Amirnasr, M.; Salimijazi, H. R.; Azarpour Siahkali, M.; Kalantari, Y.; Mohammadnezhad, M. Photocatalytic Iron Oxide Coatings Produced by Thermal Spraying Process. *J. Therm. Spray Technol.* 2015, 24 (8), 1487-1497.

27. Amirulsyafiee, A.; Khan, M. M.; Harunsani, M. H. Ag_3PO_4 and Ag_3PO_4–Based Visible Light Active Photocatalysts: Recent Progress, Synthesis, and Photocatalytic Applications. *Catal. Commun.* 2022, 172, 106556.

28. Milani, M.; Mazzanti, M.; Caramori, S.; Di Carmine, G.; Magnacca, G.; Molinari, A. Composite CdS/TiO_2 Powders for the Selective Reduction of 4-Nitrobenzaldehyde by Visible

Light: Relation between Preparation, Morphology and Photocatalytic Activity. *Catalysts* 2023, 13 (1), 74.

29. Lou, Z.; Kim, S.; Fujitsuka, M.; Yang, X.; Li, B.; Majima, T. Anisotropic Ag_2S–Au Triangular Nanoprisms with Desired Configuration for Plasmonic Photocatalytic Hydrogen Generation in Visible/Near-Infrared Region. *Adv. Funct. Mater.* 2018, 28 (13), 1706969.

30. Tsay, C.-Y.; Chung, C.-Y.; Chen, C.-Y.; Chang, Y.-C.; Chang, C.-J.; Wu, J. J. Enhanced Photocatalytic Performance of Visible-Light-Driven $BiVO_4$ Nanoparticles through W and Mo Substituting. *Catalysts* 2023, 13 (3), 475.

31. Mohana Roopan, S.; Khan, M. A. MoS_2 Based Ternary Composites: Review on Heterogeneous Materials as Catalyst for Photocatalytic Degradation. *Catal. Rev.* 2021, 1-74.

32. Navidpour, A. H.; Salehi, M.; Salimijazi, H. R.; Kalantari, Y.; Azarpour Siahkali, M. Photocatalytic Activity of Flame-Sprayed Coating of Zinc Ferrite Powder. *J. Therm. Spray Technol.* 2017, 26 (8), 2030-2039.

33. Navidpour, A. H.; Fakhrzad, M. Photocatalytic and Magnetic Properties of $ZnFe_2O_4$ Nanoparticles Synthesised by Mechanical Alloying. *Int. J. Environ. Anal. Chem.* 2022, 102 (3), 690-706.

34. Zhai, B.; Chen, Y.; Liang, Y.; Gao, Y.; Shi, J.; Zhang, H.; Li, Y. Modifying Ag_3VO_4 with Metal-Organic Frameworks for Enhanced Photocatalytic Activity under Visible Light. *Mater. Chem. Phys.* 2020, 239, 122078.

35. Mishra, M.; Chun, D.-M. α-Fe_2O_3 as a Photocatalytic Material: A Review. *Appl. Catal. A: Gen.* 2015, 498, 126-141.

36. Kolivand, A.; Sharifnia, S. Enhanced Photocatalytic Hydrogen Evolution from Water Splitting by Z-scheme CdS/$BiFeO_3$ Heterojunction without Using Sacrificial Agent. *Int. J. Energy Res.* 2021, 45 (2), 2739-2752.

37. Di, L.; Xian, T.; Sun, X.; Li, H.; Zhou, Y.; Ma, J.; Yang, H. Facile Preparation of CNT/Ag_2S Nanocomposites with Improved Visible and NIR Light Photocatalytic Degradation Activity and Their Catalytic Mechanism. *Micromachines* 2019, 10 (8), 503.

38. Sonu; Sharma, S.; Dutta, V.; Raizada, P.; Hosseini-Bandegharaei, A.; Thakur, V.; Nguyen, V.-H.; VanLe, Q.; Singh, P. An Overview of Heterojunctioned $ZnFe_2O_4$ Photocatalyst for Enhanced Oxidative Water Purification. *J. Environ. Chem. Eng.* 2021, 9 (5), 105812.

39. Tolod, K. R.; Hernández, S.; Russo, N. Recent Advances in the $BiVO_4$ Photocatalyst for Sun-Driven Water Oxidation: Top-Performing Photoanodes and Scale-Up Challenges. *Catalysts* 2017, 7 (1), 13.

40. Chanda, N.; Koteshwar, D.; Gonuguntla, S.; Bojja, S.; Pal, U.; Giribabu, L. Efficient Visible-Light-Driven Hydrogen Production by Zn–Porphyrin Based Photocatalyst with Engineered Active Donor–Acceptor Sites. *Mater. Adv.* 2021, 2 (14), 4762-4771.

41. Yuan, Y.-J.; Shen, Z.; Wu, S.; Su, Y.; Pei, L.; Ji, Z.; Ding, M.; Bai, W.; Chen, Y.; Yu, Z.-T.; Zou, Z. Liquid Exfoliation of g-C_3N_4 Nanosheets to Construct 2D-2D MoS_2/g-C_3N_4 Photocatalyst for Enhanced Photocatalytic H_2 Production Activity. *Appl. Catal. B: Environ.* 2019, 246, 120-128.

42. Mishra, A.; Mehta, A.; Basu, S.; Shetti, N. P.; Reddy, K. R.; Aminabhavi, T. M. Graphitic Carbon Nitride (g–C_3N_4)–Based Metal-Free Photocatalysts for Water Splitting: A Review. *Carbon* 2019, 149, 693-721.

43. Low, J.; Cheng, B.; Yu, J.; Jaroniec, M. Carbon-Based Two-Dimensional Layered Materials for Photocatalytic CO_2 Reduction to Solar Fuels. *Energy Storage Mater.* 2016, 3, 24-35.

44. Hao, Q.; Xie, C. a.; Huang, Y.; Chen, D.; Liu, Y.; Wei, W.; Ni, B.-J. Accelerated Separation of Photogenerated Charge Carriers and Enhanced Photocatalytic Performance of g-C_3N_4 by Bi_2S_3 Nanoparticles. *Chinese J. Catal.* 2020, 41 (2), 249-258.

45. Zhang, C.; Li, Y.; Shuai, D.; Shen, Y.; Xiong, W.; Wang, L. Graphitic Carbon Nitride (g-C_3N_4)-Based Photocatalysts for Water Disinfection and Microbial Control: A Review. *Chemosphere* 2019, 214, 462-479.

46. Yuan, Y.; Zhang, L.; Xing, J.; Utama, M. I. B.; Lu, X.; Du, K.; Li, Y.; Hu, X.; Wang, S.; Genç, A.; et al. High-Yield Synthesis and Optical Properties of g-C_3N_4. *Nanoscale* 2015, 7 (29), 12343-12350.

47. Kumar, S.; Karthikeyan, S.; Lee, A. F. g-C_3N_4-Based Nanomaterials for Visible Light-Driven Photocatalysis. *Catalysts* 2018, 8 (2), 74.

48. Akhundi, A.; Habibi-Yangjeh, A.; Abitorabi, M.; Rahim Pouran, S. Review on Photocatalytic Conversion of Carbon Dioxide to Value-Added Compounds and Renewable Fuels by Graphitic Carbon Nitride-Based Photocatalysts. *Catal. Rev.* 2019, 61 (4), 595-628.

49. Ye, S.; Wang, R.; Wu, M.-Z.; Yuan, Y.-P. A Review on g-C_3N_4 for Photocatalytic Water Splitting and CO_2 Reduction. *Appl. Surf. Sci.* 2015, 358, 15-27.

50. Iqbal, W.; Qiu, B.; Lei, J.; Wang, L.; Zhang, J.; Anpo, M. One-Step Large-Scale Highly Active g-C_3N_4 Nanosheets for Efficient Sunlight-Driven Photocatalytic Hydrogen Production. *Dalton Trans.* 2017, 46 (32), 10678-10684.

51. Rashidizadeh, A.; Ghafuri, H.; Rezazadeh, Z. Improved Visible-Light Photocatalytic Activity of g-C_3N_4/$CuWO_4$ Nanocomposite for Degradation of Methylene Blue. *Proceedings* 2020, 41 (1), 43.

52. Ge, L.; Han, C.; Liu, J. Novel Visible Light-Induced g-C_3N_4/Bi_2WO_6 Composite Photocatalysts for Efficient Degradation of Methyl Orange. *Appl. Catal. B: Environ.* 2011, 108-109, 100-107.

53. Zhang, C.; Liu, J.; Huang, X.; Chen, D.; Xu, S. Multistage Polymerization Design for g-C_3N_4 Nanosheets with Enhanced Photocatalytic Activity by Modifying the Polymerization Process of Melamine. *ACS Omega* 2019, 4 (17), 17148-17159.

54. Chang, C.; Fu, Y.; Hu, M.; Wang, C.; Shan, G.; Zhu, L. Photodegradation of Bisphenol A by Highly Stable Palladium-Doped Mesoporous Graphite Carbon Nitride (Pd/mpg-C_3N_4) under Simulated Solar Light Irradiation. *Appl. Catal. B: Environ.* 2013, 142-143, 553-560.

55. Samsudin, M. F. R.; Bacho, N.; Sufian, S.; Ng, Y. H. Photocatalytic Degradation of Phenol Wastewater over Z-Scheme g-C_3N_4/CNT/$BiVO_4$ Heterostructure Photocatalyst under Solar Light Irradiation. *J. Mol. Liq.* 2019, 277, 977-988.

56. Xu, T.; Zou, R.; Lei, X.; Qi, X.; Wu, Q.; Yao, W.; Xu, Q. New and Stable g-C_3N_4/HAp Composites as Highly Efficient Photocatalysts for Tetracycline Fast Degradation. *Appl. Catal. B: Environ.* 2019, 245, 662-671.

57. Gao, B.; Wang, J.; Dou, M.; Xu, C.; Huang, X. Enhanced Photocatalytic Removal of Amoxicillin with Ag/TiO_2/Mesoporous g-C_3N_4 under Visible Light: Property and Mechanistic Studies. *Environ. Sci. Pollut. Res.* 2020, 27 (7), 7025-7039.

58. Truc, N. T. T.; Duc, D. S.; Van Thuan, D.; Tahtamouni, T. A.; Pham, T.-D.; Hanh, N. T.; Tran, D. T.; Nguyen, M. V.; Dang, N. M.; Le Chi, N. T. P.; et al. The Advanced Photocatalytic Degradation of Atrazine by Direct Z-Scheme Cu Doped ZnO/g-C_3N_4. *Appl. Surf. Sci.* 2019, 489, 875-882.

59. Kesarla, M. K.; Fuentez-Torres, M. O.; Alcudia-Ramos, M. A.; Ortiz-Chi, F.; Espinosa-González, C. G.; Aleman, M.; Torres-Torres, J. G.; Godavarthi, S. Synthesis of g-C_3N_4/N-Doped CeO_2 Composite for Photocatalytic Degradation of an Herbicide. *J. Mater. Res. Technol.* 2019, 8 (2), 1628-1635.

60. Thomas, A.; Fischer, A.; Goettmann, F.; Antonietti, M.; Müller, J.-O.; Schlögl, R.; Carlsson, J. M. Graphitic Carbon Nitride Materials: Variation of Structure and Morphology and Their Use as Metal-Free Catalysts. *J. Mater. Chem.* 2008, 18 (41), 4893-4908.

61. Zhu, J.; Xiao, P.; Li, H.; Carabineiro, S. A. C. Graphitic Carbon Nitride: Synthesis, Properties, and Applications in Catalysis. *ACS Appl. Mater. Interfaces* 2014, 6 (19), 16449-16465.

62. Xu, Y.; Gao, S.-P. Band Gap of C_3N_4 in the GW Approximation. *Int. J. Hydrog. Energy* 2012, 37 (15), 11072-11080.

63. Praus, P.; Svoboda, L.; Ritz, M.; Troppová, I.; Šihor, M.; Kočí, K. Graphitic Carbon Nitride: Synthesis, Characterization and Photocatalytic Decomposition of Nitrous Oxide. *Mater. Chem. Phys.* 2017, 193, 438-446.

64. Alaghmandfard, A.; Ghandi, K. A Comprehensive Review of Graphitic Carbon Nitride (g-C_3N_4)–Metal Oxide-Based Nanocomposites: Potential for Photocatalysis and Sensing. *Nanomaterials* 2022, 12 (2), 294.

65. Wang, A.; Wang, C.; Fu, L.; Wong-Ng, W.; Lan, Y. Recent Advances of Graphitic Carbon Nitride-Based Structures and Applications in Catalyst, Sensing, Imaging, and LEDs. *Nanomicro Lett.* 2017, 9 (4), 47.

66. Ong, W.-J.; Tan, L.-L.; Ng, Y. H.; Yong, S.-T.; Chai, S.-P. Graphitic Carbon Nitride (g-C_3N_4)-Based Photocatalysts for Artificial Photosynthesis and Environmental Remediation: Are We a Step Closer To Achieving Sustainability? *Chem. Rev.* 2016, 116 (12), 7159-7329.

67. Mousavi, M.; Habibi-Yangjeh, A.; Pouran, S. R. Review on Magnetically Separable Graphitic Carbon Nitride-Based Nanocomposites as Promising Visible-Light-Driven Photocatalysts. *J. Mater. Sci.: Mater. Electron.* 2018, 29 (3), 1719-1747.

68. Wang, X.; Blechert, S.; Antonietti, M. Polymeric Graphitic Carbon Nitride for Heterogeneous Photocatalysis. *ACS Catal.* 2012, 2 (8), 1596-1606.

69. Samsudin, M. F. R.; Bacho, N.; Sufian, S. Recent Development of Graphitic Carbon Nitride-Based Photocatalyst for Environmental Pollution Remediation. 2019; pp 1-15.

70. Suyana, P.; Ganguly, P.; Nair, B. N.; Pillai, S. C.; Hareesh, U. S. Structural and Compositional Tuning in g-C_3N_4 Based Systems for Photocatalytic Antibiotic Degradation. *Chem. Eng. J. Adv.* 2021, 8, 100148.

71. Wang, X.; Chen, X.; Thomas, A.; Fu, X.; Antonietti, M. Metal-Containing Carbon Nitride Compounds: A New Functional Organic-Metal Hybrid Material. *Adv. Mater.* 2009, 21 (16), 1609-1612.

72. Shi, L.; Liang, L.; Wang, F.; Ma, J.; Sun, J. Polycondensation of Guanidine Hydrochloride into a Graphitic Carbon Nitride Semiconductor with a Large Surface Area as a Visible Light Photocatalyst. *Catal. Sci. Technol.* 2014, 4 (9), 3235-3243.

73. Zhao, Z.; Fan, J.; Yongqiang, X.; Chang, H.; Masubuchi, Y.; Yin, S. Synthesis of Graphitic Carbon Nitride from Different Precursors by Fractional Thermal Polymerization Method and Their Visible Light Induced Photocatalytic Activities. *J. Alloys Compd.* 2018, 735, 1297-1305.

74. Zhang, Y.; Zhao, H.; Hu, Z.; Chen, H.; Zhang, X.; Huang, Q.; Wo, Q.; Zhang, S. Protic Salts of High Nitrogen Content as Versatile Precursors for Graphitic Carbon Nitride: Anion Effect on the Structure, Properties, and Photocatalytic Activity. *ChemPlusChem* 2015, 80 (7), 1139-1147.

75. Xin, G.; Meng, Y. Pyrolysis Synthesized g-C_3N_4 for Photocatalytic Degradation of Methylene Blue. *J. Chem.* 2013, 2013, 1-5.

76. Zhang, W.; Zhang, Q.; Dong, F.; Zhao, Z. The Multiple Effects of Precursors on the Properties of Polymeric Carbon Nitride. *Int. J. Photoenergy* 2013, 2013, 1-9.

77. Alwin, E.; Kočí, K.; Wojcieszak, R.; Zieliński, M.; Edelmannová, M.; Pietrowski, M. Influence of High Temperature Synthesis on the Structure of Graphitic Carbon Nitride and Its Hydrogen Generation Ability. *Materials* 2020, 13 (12), 2756.

78. Zheng, Y.; Zhang, Z.; Li, C. A Comparison of Graphitic Carbon Nitrides Synthesized from Different Precursors through Pyrolysis. *J. Photochem. Photobiol. A: Chem.* 2017, 332, 32-44.

79. Matějka, V.; Škuta, R.; Foniok, K.; Novák, V.; Cvejn, D.; Martaus, A.; Michalska, M.; Pavlovský, J.; Praus, P. The Role of the g-C_3N_4 Precursor on the P Doping Using HCCP as a Source of Phosphorus. *J. Mater. Res. Technol.* 2022, 18, 3319-3335.

80. Panneri, S.; Ganguly, P.; Nair, B. N.; Mohamed, A. A. P.; Warrier, K. G. K.; Hareesh, U. N. S. Role of Precursors on the Photophysical Properties of Carbon Nitride and Its Application for Antibiotic Degradation. *Environ. Sci. Pollut. Res.* 2017, 24 (9), 8609-8618.

81. Wu, P.; Wang, J.; Zhao, J.; Guo, L.; Osterloh, F. E. Structure Defects in g-C_3N_4 Limit Visible Light Driven Hydrogen Evolution and Photovoltage. *J. Mater. Chem. A* 2014, 2 (47), 20338-20344.

82. Martha, S.; Nashim, A.; Parida, K. M. Facile Synthesis of Highly Active g-C_3N_4 for Efficient Hydrogen Production under Visible Light. *J. Mater. Chem. A* 2013, 1 (26), 7816-7824.

83. Xu, J.; Wang, Y.; Zhu, Y. Nanoporous Graphitic Carbon Nitride with Enhanced Photocatalytic Performance. *Langmuir* 2013, 29 (33), 10566-10572.

84. Mo, Z.; She, X.; Li, Y.; Liu, L.; Huang, L.; Chen, Z.; Zhang, Q.; Xu, H.; Li, H. Synthesis of g-C_3N_4 at Different Temperatures for Superior Visible/UV Photocatalytic Performance and Photoelectrochemical Sensing of MB Solution. *RSC Adv.* 2015, 5 (123), 101552-101562.

85. Yan, S. C.; Li, Z. S.; Zou, Z. G. Photodegradation Performance of g-C_3N_4 Fabricated by Directly Heating Melamine. *Langmuir* 2009, 25 (17), 10397-10401.

86. Yousefzadeh, S. Effect of Thermal Condensation Temperature on Electrochemical Capacitive Properties of g-C_3N_4 Supported on Reduced TiO_2 Nanowires/Nanotubes Array. *J. Alloys Compd.* 2019, 785, 1-6.

87. Yuan, X.; Zhou, C.; Jin, Y.; Jing, Q.; Yang, Y.; Shen, X.; Tang, Q.; Mu, Y.; Du, A.-K. Facile Synthesis of 3D Porous Thermally Exfoliated g-C_3N_4 Nanosheet with Enhanced Photocatalytic Degradation of Organic Dye. *J. Colloid Interface Sci.* 2016, 468, 211-219.

88. Kottappara, R.; Palantavida, S.; Vijayan, B. K., Chapter 7 - Enhancing semiconductor photocatalysis with carbon nanostructures for water/air purification and self-cleaning applications. In *Carbon Based Nanomaterials for Advanced Thermal and Electrochemical Energy Storage and Conversion*, Paul, R.; Etacheri, V.; Wang, Y.; Lin, C.-T., Eds. Elsevier: 2019; pp 139-172.

89. Zhang, X.; Xie, X.; Wang, H.; Zhang, J.; Pan, B.; Xie, Y. Enhanced Photoresponsive Ultrathin Graphitic-Phase C_3N_4 Nanosheets for Bioimaging. *J. Am. Chem. Soc.* 2013, 135 (1), 18-21.

90. Dong, X.; Cheng, F. Recent Development in Exfoliated Two-Dimensional g-C_3N_4 Nanosheets for Photocatalytic Applications. *J. Mater. Chem. A* 2015, 3 (47), 23642-23652.

91. Ciesielski, A.; Samorì, P. Graphene via Sonication Assisted Liquid-Phase Exfoliation. *Chem. Soc. Rev.* 2014, 43 (1), 381-398.

92. Xu, Y.; Cao, H.; Xue, Y.; Li, B.; Cai, W. Liquid-Phase Exfoliation of Graphene: An Overview on Exfoliation Media, Techniques, and Challenges. *Nanomaterials* 2018, 8 (11), 942.

93. Sahoo, D.; Kumar, B.; Sinha, J.; Ghosh, S.; Roy, S. S.; Kaviraj, B. Cost Effective Liquid Phase Exfoliation of MoS_2 Nanosheets and Photocatalytic Activity for Wastewater Treatment Enforced by Visible Light. *Sci. Rep.* 2020, 10 (1), 10759.

94. Liu, Y.-T.; Zhu, X.-D.; Xie, X.-M. Direct Exfoliation of High-Quality, Atomically Thin $MoSe_2$ Layers in Water. *Adv. Sustain. Syst.* 2018, 2 (1), 1700107.

95. Tian, Z.; Chen, K.; Sun, S.; Zhang, J.; Cui, W.; Xie, Z.; Liu, G. Crystalline Boron Nitride Nanosheets by Sonication-Assisted Hydrothermal Exfoliation. *J. Adv. Ceram.* 2019, 8 (1), 72-78.

96. Ott, S.; Lakmann, M.; Backes, C. Impact of Pretreatment of the Bulk Starting Material on the Efficiency of Liquid Phase Exfoliation of WS_2. *Nanomaterials* 2021, 11 (5), 1072.

97. Turner, P.; Hodnett, M.; Dorey, R.; Carey, J. D. Controlled Sonication as a Route to in-situ Graphene Flake Size Control. *Sci. Rep.* 2019, 9 (1), 8710.

98. Chebanenko, M. I.; Zakharova, N. V.; Lobinsky, A. A.; Popkov, V. I. Ultrasonic-Assisted Exfoliation of Graphitic Carbon Nitride and its Electrocatalytic Performance in Process of Ethanol Reforming. *Semiconductors* 2019, 53 (16), 2072-2077.

99. Narayan, R.; Kim, S. O. Surfactant Mediated Liquid Phase Exfoliation of Graphene. *Nano Converg.* 2015, 2 (1), 20.

100. Hernandez, Y.; Nicolosi, V.; Lotya, M.; Blighe, F. M.; Sun, Z.; De, S.; McGovern, I. T.; Holland, B.; Byrne, M.; Gun'Ko, Y. K.; et al. High-Yield Production of Graphene by Liquid-Phase Exfoliation of Graphite. *Nat. Nanotechnol.* 2008, 3 (9), 563-568.

101. Yang, S.; Gong, Y.; Zhang, J.; Zhan, L.; Ma, L.; Fang, Z.; Vajtai, R.; Wang, X.; Ajayan, P. M. Exfoliated Graphitic Carbon Nitride Nanosheets as Efficient Catalysts for Hydrogen Evolution Under Visible Light. *Adv. Mater.* 2013, 25 (17), 2452-2456.

102. Bree, G.; Tong John Low, C. Full Cell Lithium-Ion Battery Manufacture by Electrophoretic Deposition. *Batteries Supercaps* 2023, 6 (2), e202200441.

103. Jiang, X.; Kang, Z.; Guo, X.; Zhuang, H. *Novel Carbon Materials and Composites: Synthesis, Properties and Applications*. Wiley: 2019.

104. Yan, T.; Liu, E.; Chu, Z.; Li, X. Scalable Synthesis of Ultrathin g-C_3N_4 Nanosheets with Enhanced Photocatalytic Activities via High Shear Exfoliation. *J. Nano Res.* 2017, 45, 49-54.

105. Paton, K. R.; Varrla, E.; Backes, C.; Smith, R. J.; Khan, U.; O’Neill, A.; Boland, C.; Lotya, M.; Istrate, O. M.; King, P.; et al. Scalable Production of Large Quantities of Defect-Free Few-Layer Graphene by Shear Exfoliation in Liquids. *Nat. Mater.* 2014, 13 (6), 624-630.

106. Wang, J.; Yang, M. 11 - Two-Dimensional Nanomaterials in Cancer Theranostics. In *Theranostic Bionanomaterials*, Cui, W.; Zhao, X., Eds. Elsevier: 2019; pp 263-288.

107. Zhang, S.; Hang, N.; Zhang, Z.; Yue, H.; Yang, W. Preparation of g-C_3N_4/Graphene Composite for Detecting NO_2 at Room Temperature. *Nanomaterials* 2017, 7 (1), 12.

108. Zhu, K.; Wang, W.; Meng, A.; Zhao, M.; Wang, J.; Zhao, M.; Zhang, D.; Jia, Y.; Xu, C.; Li, Z. Mechanically Exfoliated g-C_3N_4 Thin Nanosheets by Ball Milling as High Performance Photocatalysts. *RSC Adv.* 2015, 5 (69), 56239-56243.

109. Liu, W.; Sun, M.; Ding, Z.; Zeng, Q.; Zheng, Y.; Sun, W.; Meng, X. Ball Milling Synthesis of Porous g-C_3N_4 Ultrathin Nanosheets Functionalized with Alkynyl Groups for Strengthened Photocatalytic Activity. *Sep. Purif. Technol.* 2022, 282, 120097.

110. Ma, Z.; Zhou, P.; Zhang, L.; Zhong, Y.; Sui, X.; Wang, B.; Ma, Y.; Feng, X.; Xu, H.; Mao, Z. g-C_3N_4 Nanosheets Exfoliated by Green Wet Ball Milling Process for Photodegradation of Organic Pollutants. *Chem. Phys. Lett.* 2021, 766, 138335.

111. Ansari, S. A.; Cho, M. H. Simple and Large Scale Construction of MoS_2-g-C_3N_4 Heterostructures Using Mechanochemistry for High Performance Electrochemical Supercapacitor and Visible Light Photocatalytic Applications. *Sci. Rep.* 2017, 7 (1), 43055.

112. Cai, X.; Jiang, Z.; Zhang, X.; Zhang, X. Effects of Tip Sonication Parameters on Liquid Phase Exfoliation of Graphite into Graphene Nanoplatelets. *Nanoscale Res. Lett.* 2018, 13 (1), 241.

113. Xu, J.; Zhang, L.; Shi, R.; Zhu, Y. Chemical Exfoliation of Graphitic Carbon Nitride for Efficient Heterogeneous Photocatalysis. *J. Mater. Chem. A* 2013, 1, 14766-14772.

114. Zou, L.-R.; Huang, G.-F.; Li, D.-F.; Liu, J.-H.; Pan, A.-L.; Huang, W.-Q. A Facile and Rapid Route for Synthesis of g-C_3N_4 Nanosheets with High Adsorption Capacity and Photocatalytic Activity. *RSC Adv.* 2016, 6 (89), 86688-86694.

115. Tong, J.; Zhang, L.; Li, F.; Wang, K.; Han, L.; Cao, S. Rapid and High-Yield Production of g-C_3N_4 Nanosheets via Chemical Exfoliation for Photocatalytic H_2 Evolution. *RSC Adv.* 2015, 5 (107), 88149-88153.

116. Niu, P.; Zhang, L.; Liu, G.; Cheng, H.-M. Graphene-Like Carbon Nitride Nanosheets for Improved Photocatalytic Activities. *Adv. Funct. Mater.* 2012, 22 (22), 4763-4770.

117. Long, W.-J.; Xu, P.; Yu, Y.; Xing, F.; He, C. Scalable Preparation of High-Dispersion g-C_3N_4 via GQDs-Assisted Ultrasonic Exfoliation for Accelerating Cement Hydration. *Cem. Concr. Compos.* 2022, 134, 104782.

118. Zhang, M.; Yang, Y.; An, X.; Zhao, J.; Bao, Y.; Hou, L.-a., Exfoliation Method Matters: The Microstructure-Dependent Photoactivity of g-C_3N_4 Nanosheets for Water Purification. *J. Hazard. Mater.* 2022, 424, 127424.

119. Hong, J.; Hwang, D. K.; Selvaraj, R.; Kim, Y. Facile Synthesis of Br-Doped g-C_3N_4 Nanosheets via One-Step Exfoliation Using Ammonium Bromide for Photodegradation of Oxytetracycline Antibiotics. *J. Ind. Eng. Chem.* 2019, 79, 473-481.

120. Lu, X.; Xu, K.; Chen, P.; Jia, K.; Liu, S.; Wu, C. Facile One Step Method Realizing Scalable Production of g-C_3N_4 Nanosheets and Study of Their Photocatalytic H_2 Evolution Activity. *J. Mater. Chem. A* 2014, 2 (44), 18924-18928.

121. Ma, F.; Sun, C.; Shao, Y.; Wu, Y.; Huang, B.; Hao, X. One-Step Exfoliation and Fluorination of g-C_3N_4 Nanosheets with Enhanced Photocatalytic Activities. *New J. Chem.* 2017, 41 (8), 3061-3067.

122. Tahir, M.; Cao, C.; Mahmood, N.; Butt, F. K.; Mahmood, A.; Idrees, F.; Hussain, S.; Tanveer, M.; Ali, Z.; Aslam, I. Multifunctional g-C_3N_4 Nanofibers: A Template-Free Fabrication and Enhanced Optical, Electrochemical, and Photocatalyst Properties. *ACS Appl. Mater. Interfaces* 2013, 6 (2), 1258-1265.

123. Hao, Q.; Jia, G.; Wei, W.; Vinu, A.; Wang, Y.; Arandiyan, H.; Ni, B.-J. Graphitic Carbon Nitride with Different Dimensionalities for Energy and Environmental Applications. *Nano Res.* 2020, 13 (1), 18-37.

124. Bai, X.; Wang, L.; Zong, R.; Zhu, Y. Photocatalytic Activity Enhanced via g-C_3N_4 Nanoplates to Nanorods. *J. Phys. Chem. C* 2013, 117 (19), 9952-9961.

125. Gao, Z.-D.; Qu, Y. F.; Zhou, X.; Wang, L.; Song, Y. Y.; Schmuki, P. Pt-Decorated g-C_3N_4/TiO_2 Nanotube Arrays with Enhanced Visible-Light Photocatalytic Activity for H_2 Evolution. *ChemistryOpen* 2016, 5, 197-200.

126. Hamedani, Y.; Macha, P.; Bunning, T. J.; Naik, R. R.; Vasudev, M. C. Plasma-Enhanced Chemical Vapor Deposition: Where We Are and the Outlook for the Future. In *Chemical Vapor Deposition - Recent Advances and Applications in Optical, Solar Cells and Solid State Devices*, 2016.

127. Jiang, Z.; Zhang, X.; Chen, H.-S.; Hu, X.; Yang, P. Formation of g-C_3N_4 Nanotubes towards Superior Photocatalysis Performance. *ChemCatChem* 2019, 11 (18), 4558-4567.

128. Mohammadi, E.; Aliofkhazraei, M.; Rouhaghdam, A. S. In-Situ Study of Electrophoretic Deposition of Zinc Oxide Nanosheets and Nanorods. *Ceram. Int.* 2018, 44 (2), 1471-1482.

129. Wang, L.; Zhou, G.; Tian, Y.; Yan, L.; Deng, M.; Yang, B.; Kang, Z.; Sun, H. Hydroxyl Decorated g-C_3N_4 Nanoparticles with Narrowed Bandgap for High Efficient Photocatalyst Design. *Appl. Catal. B: Environ.* 2019, 244, 262-271.

130. Wang, T.; Nie, C.; Ao, Z.; Wang, S.; An, T. Recent Progress in g-C_3N_4 Quantum Dots: Synthesis, Properties and Applications in Photocatalytic Degradation of Organic Pollutants. *J. Mater. Chem. A* 2020, 8 (2), 485-502.

131. Xu, B.; Ahmed, M. B.; Zhou, J. L.; Altaee, A.; Xu, G.; Wu, M. Graphitic Carbon Nitride Based Nanocomposites for the Photocatalysis of Organic Contaminants under Visible Irradiation: Progress, Limitations and Future Directions. *Sci. Total Environ.* 2018, 633, 546-559.

132. Patnaik, S.; Martha, S.; Parida, K. M. An Overview of the Structural, Textural and Morphological Modulations of g-C_3N_4 towards Photocatalytic Hydrogen Production. *RSC Adv.* 2016, 6 (52), 46929-46951.

133. Jun, Y.-S.; Lee, E. Z.; Wang, X.; Hong, W. H.; Stucky, G. D.; Thomas, A. From Melamine-Cyanuric Acid Supramolecular Aggregates to Carbon Nitride Hollow Spheres. *Adv. Funct. Mater.* 2013, 23 (29), 3661-3667.

134. Ge, G.; Guo, X.; Song, C.; Zhao, Z. Reconstructing Supramolecular Aggregates to Nitrogen-Deficient g-C_3N_4 Bunchy Tubes with Enhanced Photocatalysis for H_2 Production. *ACS Appl. Mater. Interfaces* 2018, 10 (22), 18746-18753.

135. Wu, K.; Chen, D.; Lu, S.; Fang, J.; Zhu, X.; Yang, F.; Pan, T.; Fang, Z. Supramolecular Self-Assembly Synthesis of Noble-Metal-Free (C, Ce) co-Doped g-C_3N_4 with Porous Structure for Highly Efficient Photocatalytic Degradation of Organic Pollutants. *J. Hazard. Mater.* 2020, 382, 121027.

136. Wang, X.; Liu, Q.; Yang, Q.; Zhang, Z.; Fang, X. Three-Dimensional g-C_3N_4 Aggregates of Hollow Bubbles with High Photocatalytic Degradation of Tetracycline. *Carbon* 2018, 136, 103-112.

137. Liao, Y.; Zhu, S.; Ma, J.; Sun, Z.; Yin, C.; Zhu, C.; Lou, X.; Zhang, D. Tailoring the Morphology of g-C_3N_4 by Self-Assembly towards High Photocatalytic Performance. *ChemCatChem* 2014, 6 (12), 3419-3425.

138. Wang, M.; Na, Y.; Gorlov, M.; Sun, L. Light-Driven Hydrogen Production Catalysed by Transition Metal Complexes in Homogeneous Systems. *Dalton Trans.* 2009, (33), 6458-6467.

139. Zhang, Y.; Gong, H.; Li, G.; Zeng, H.; Zhong, L.; Liu, K.; Cao, H.; Yan, H. Synthesis of Graphitic Carbon Nitride by Heating Mixture of Urea and Thiourea for Enhanced Photocatalytic H_2 Production from Water under Visible Light. *Int. J. Hydrog. Energy* 2017, 42 (1), 143-151.

140. Bellardita, M.; García-López, E. I.; Marcì, G.; Krivtsov, I.; García, J. R.; Palmisano, L. Selective Photocatalytic Oxidation of Aromatic Alcohols in Water by Using P-Doped g-C_3N_4. *Appl. Catal. B: Environ.* 2018, 220, 222-233.

141. Thorat, N.; Yadav, A.; Yadav, M.; Gupta, S.; Varma, R.; Pillai, S.; Fernandes, R.; Patel, M.; Patel, N. Ag Loaded B-Doped-g C_3N_4 Nanosheet with Efficient Properties for Photocatalysis. *J. Environ. Manage.* 2019, 247, 57-66.

142. Yang, H.; Zhou, Y.; Wang, Y.; Hu, S.; Wang, B.; Liao, Q.; Li, H.; Bao, J.; Ge, G.; Jia, S. Three-Dimensional Flower-Like Phosphorus-Doped g-C_3N_4 with a High Surface Area for Visible-Light Photocatalytic Hydrogen Evolution. *J. Mater. Chem. A* 2018, 6 (34), 16485-16494.

143. Zhou, Y.; Zhang, L.; Liu, J.; Fan, X.; Wang, B.; Wang, M.; Ren, W.; Wang, J.; Li, M.; Shi, J. Brand New P-Doped g-C_3N_4: Enhanced Photocatalytic Activity for H_2 Evolution and Rhodamine B Degradation under Visible Light. *J. Mater. Chem. A* 2015, 3 (7), 3862-3867.

144. Feng, J.; Zhang, D.; Zhou, H.; Pi, M.; Wang, X.; Chen, S. Coupling P Nanostructures with P-Doped g-C_3N_4 As Efficient Visible Light Photocatalysts for H_2 Evolution and RhB Degradation. *ACS Sustain. Chem. Eng.* 2018, 6 (5), 6342-6349.

145. Wu, M.; Zhang, J.; He, B.-B.; Wang, H.-W.; Wang, R.; Gong, Y.-S. In-Situ Construction of Coral-Like Porous P-Doped g-C_3N_4 Tubes with Hybrid 1D/2D Architecture and High Efficient Photocatalytic Hydrogen Evolution. *Appl. Catal. B: Environ.* 2019, 241, 159-166.

146. Guo, S.; Tang, Y.; Xie, Y.; Tian, C.; Feng, Q.; Zhou, W.; Jiang, B. P-doped Tubular g-C_3N_4 with Surface Carbon Defects: Universal Synthesis and Enhanced Visible-Light Photocatalytic Hydrogen Production. *Appl. Catal. B: Environ.* 2017, 218, 664-671.

147. Lin, Q.; Li, Z.; Lin, T.; Li, B.; Liao, X.; Yu, H.; Yu, C. Controlled Preparation of P-Doped g-C_3N_4 Nanosheets for Efficient Photocatalytic Hydrogen Production. *Chin. J. Chem. Eng.* 2020, 28 (10), 2677-2688.

148. Liu, S.; Zhu, H.; Yao, W.; Chen, K.; Chen, D. One Step Synthesis of P-Doped g-C_3N_4 with the Enhanced Visible Light Photocatalytic Activity. *Appl. Surf. Sci.* 2018, 430, 309-315.

149. Mishra, B. P.; Babu, P.; Parida, K. Phosphorous, Boron and Sulfur Doped g-C_3N_4 Nanosheet: Synthesis, Characterization, and Comparative Study towards Photocatalytic Hydrogen Generation. *Mater. Today: Proc.* 2021, 35, 258-262.

150. Liu, M.; Jiao, Y.; Qin, J.; Li, Z.; Wang, J. Boron Doped C_3N_4 Nanodots/Nonmetal Element (S, P, F, Br) Doped C_3N_4 Nanosheets Heterojunction with Synergistic Effect to Boost the Photocatalytic Hydrogen Production Performance. *Appl. Surf. Sci.* 2021, 541, 148558.

151. Guo, H.; Shu, Z.; Chen, D.; Tan, Y.; Zhou, J.; Meng, F.; Li, T. One-Step Synthesis of S-Doped g-C_3N_4 Nanosheets for Improved Visible-Light Photocatalytic Hydrogen Evolution. *Chem. Phys.* 2020, 533, 110714.

152. Ge, L.; Han, C.; Xiao, X.; Guo, L.; Li, Y. Enhanced Visible Light Photocatalytic Hydrogen Evolution of Sulfur-Doped Polymeric g-C_3N_4 Photocatalysts. *Mater. Res. Bull.* 2013, 48 (10), 3919-3925.

153. Deng, P.; Xiong, J.; Lei, S.; Wang, W.; Ou, X.; Xu, Y.; Xiao, Y.; Cheng, B. Nickel Formate Induced High-Level In Situ Ni-Doping of g-C_3N_4 for a Tunable Band Structure and Enhanced Photocatalytic Performance. *J. Mater. Chem. A* 2019, 7 (39), 22385-22397.

154. Yue, B.; Li, Q.; Iwai, H.; Kako, T.; Ye, J. Hydrogen Production Using Zinc-Doped Carbon Nitride Catalyst Irradiated with Visible Light. *Sci. Technol. Adv. Mater.* 2011, 12 (3), 034401.

155. Chen, P.-W.; Li, K.; Yu, Y.-X.; Zhang, W.-D. Cobalt-Doped Graphitic Carbon Nitride Photocatalysts with High Activity for Hydrogen Evolution. *Appl. Surf. Sci.* 2017, 392, 608-615.

156. Hu, S.; Yu, A.; Lu, R. A Comparison Study of Sodium Ion- and Potassium Ion-Modified Graphitic Carbon Nitride for Photocatalytic Hydrogen Evolution. *RSC Adv.* 2021, 11 (26), 15701-15709.

157. Li, Y.; Zhu, S.; Liang, Y.; Li, Z.; Wu, S.; Chang, C.; Luo, S.; Cui, Z. One-Step Synthesis of Mo and S co-Doped Porous g-C_3N_4 Nanosheets for Efficient Visible-Light Photocatalytic Hydrogen Evolution. *Appl. Surf. Sci.* 2021, 536, 147743.

158. Zhu, X.; Yang, F.; Liu, J.; Zhou, G.; Chen, D.; Liu, Z.; Fang, J. Design and Architecture of P-O Co-Doped Porous g-C_3N_4 by Supramolecular Self-Assembly for Enhanced Hydrogen Evolution. *Catalysts* 2022, 12 (12), 1583.

159. Liu, X.; Ma, R.; Zhuang, L.; Hu, B.; Chen, J.; Liu, X.; Wang, X. Recent Developments of Doped g-C_3N_4 Photocatalysts for the Degradation of Organic Pollutants. *Crit. Rev. Environ. Sci. Technol.* 2021, 51 (8), 751-790.

160. Tan, Y.; Chen, W.; Liao, G.; Li, X.; Wang, J.; Tang, Y.; Li, L. Strategy for Improving Photocatalytic Ozonation Activity of g-C_3N_4 by Halogen Doping for Water Purification. *Appl. Catal. B: Environ.* 2022, 306, 121133.

161. Liu, Y.; Zhang, Y.; Shi, L. One-Step Synthesis of S-Doped and Nitrogen-Defects co-Modified Mesoporous g-C_3N_4 with Excellent Photocatalytic Hydrogen Production Efficiency and Degradation Ability. *Colloids Surf. A: Physicochem. Eng. Asp.* 2022, 641, 128577.

162. Li, Y.; He, Z.; Liu, L.; Jiang, Y.; Ong, W.-J.; Duan, Y.; Ho, W.; Dong, F. Inside-and-Out Modification of Graphitic Carbon Nitride (g-C_3N_4) Photocatalysts via Defect Engineering for Energy and Environmental Science. *Nano Energy* 2023, 105, 108032.

163. Zhai, H.; Tan, P.; Lu, L.; Liu, H.; Liu, Y.; Pan, J. Abundant Hydroxyl Groups Decorated on Nitrogen Vacancy-Embedded g-C_3N_4 with Efficient Photocatalytic Hydrogen Evolution Performance. *Catal. Sci. Technol.* 2021, 11 (11), 3914-3924.

164. Li, Y.; Gu, M.; Zhang, M.; Zhang, X.; Lv, K.; Liu, Y.; Ho, W.; Dong, F. C_3N_4 with Engineered Three Coordinated ($N3_C$) Nitrogen Vacancy Boosts the Production of $^1O_2$ for Efficient and Stable NO Photo-Oxidation. *Chem. Eng. J.* 2020, 389, 124421.

165. Lee, Y.-J.; Jeong, Y. J.; Cho, I. S.; Park, S.-J.; Lee, C.-G.; Alvarez, P. J. J. Facile Synthesis of N Vacancy g-C_3N_4 Using Mg-Induced Defect on the Amine Groups for Enhanced Photocatalytic •OH Generation. *J. Hazard. Mater.* 2023, 449, 131046.

166. Liao, Y.; Wang, G.; Wang, J.; Wang, K.; Yan, S.; Su, Y. Nitrogen Vacancy Induced In Situ g-C_3N_4 P-N Homojunction for Boosting Visible Light-Driven Hydrogen Evolution. *J. Colloid Interface Sci.* 2021, 587, 110-120.

167. Niu, P.; Yin, L.-C.; Yang, Y.-Q.; Liu, G.; Cheng, H.-M. Increasing the Visible Light Absorption of Graphitic Carbon Nitride (Melon) Photocatalysts by Homogeneous Self-Modification with Nitrogen Vacancies. *Adv. Mater.* 2014, 26 (47), 8046-8052.

168. Kong, L.; Mu, X.; Fan, X.; Li, R.; Zhang, Y.; Song, P.; Ma, F.; Sun, M. Site-Selected N Vacancy of g-C_3N_4 for Photocatalysis and Physical Mechanism. *Appl. Mater. Today* 2018, 13, 329-338.

169. Liu, J.; Fang, W.; Wei, Z.; Qin, Z.; Jiang, Z.; Shangguan, W. Efficient Photocatalytic Hydrogen Evolution on N-Deficient g-C_3N_4 Achieved by a Molten Salt Post-Treatment Approach. *Appl. Catal. B: Environ.* 2018, 238, 465-470.

170. He, X.; Lei, L.; Wen, J.; Zhao, Y.; Cui, L.; Wu, G. One-Pot Synthesis of C-Doping and Defects co-Modified g-C_3N_4 for Enhanced Visible-Light Photocatalytic Degradation of Bisphenol A. *J. Environ. Chem. Eng.* 2022, 10 (1), 106911.

171. Yan, W.; Yan, L.; Jing, C. Impact of Doped Metals on Urea-Derived g-C_3N_4 for Photocatalytic Degradation of Antibiotics: Structure, Photoactivity and Degradation Mechanisms. *Appl. Catal. B: Environ.* 2019, 244, 475-485.

172. Xing, Y.; Wang, X.; Hao, S.; Zhang, X.; Wang, X.; Ma, W.; Zhao, G.; Xu, X. Recent Advances in the Improvement of g-C_3N_4 Based Photocatalytic Materials. *Chin. Chem. Lett.* 2021, 32 (1), 13-20.

173. Oh, W.-D.; Chang, V. W. C.; Hu, Z.-T.; Goei, R.; Lim, T.-T. Enhancing the Catalytic Activity of g-C_3N_4 through Me Doping (Me=Cu, Co and Fe) for Selective Sulfathiazole Degradation via Redox-Based Advanced Oxidation Process. *Chem. Eng. J.* 2017, 323, 260-269.

174. Wang, Y.; Zhou, X.; Xu, W.; Sun, Y.; Wang, T.; Zhang, Y.; Dong, J.; Hou, W.; Wu, N.; Wu, L.; et al. Zn-Doped Tri-S-Triazine Crystalline Carbon Nitrides for Efficient Hydrogen Evolution Photocatalysis. *Appl. Catal. A: Gen.* 2019, 582, 117118.

175. Ge, Z.; Yu, A.; Lu, R. Preparation of Li-Doped Graphitic Carbon Nitride with Enhanced Visible-Light Photoactivity. *Mater. Lett.* 2019, 250, 9-11.

176. Vasu, D.; Keyan, A. K.; Sakthinathan, S.; Yu, C.-L.; You, Y.-F.; Chiu, T.-W.; Fan, L.; Chen, P.-C. Visible-Light-Active Vanadium and Copper Co-Doped gCN Nanosheets with Double Direct Z-Scheme Heterojunctions for Photocatalytic Removal of Monocrotophos Pesticide in Water. *Catalysts* 2022, 12 (11), 1489.

177. Dahiya, S.; Sharma, A.; Chaudhary, S. Synthesis of Phytoextract-Mediated Ag-Doped Graphitic Carbon Nitride (Ag@GCN) for Photocatalytic Degradation of Dyes. *Environ. Sci. Pollut. Res.* 2023, 30, 25650-25662.

178. Li, H.; Xia, Y.; Liang, Z.; Ba, G.; Hou, W. Energy Band Engineering of Polymeric Carbon Nitride with Indium Doping for High Enhancement in Charge Separation and Photocatalytic Performance. *ACS Appl. Energy Mater.* 2020, 3 (1), 377-386.

179. Rawal, S. B.; Bera, S.; Lee, D.; Jang, D.-J.; Lee, W. I. Design of Visible-Light Photocatalysts by Coupling of Narrow Bandgap Semiconductors and TiO_2: Effect of Their Relative Energy Band Positions on the Photocatalytic Efficiency. *Catal. Sci. Technol.* 2013, 3 (7), 1822-1830.

180. Xu, C.; Ravi Anusuyadevi, P.; Aymonier, C.; Luque, R.; Marre, S. Nanostructured Materials for Photocatalysis. *Chem. Soc. Rev.* 2019, 48 (14), 3868-3902.

181. Angel, R. D.; Durán-Álvarez, J. C.; Zanella, R. TiO_2-Low Band Gap Semiconductor Heterostructures for Water Treatment Using Sunlight-Driven Photocatalysis. In *Titanium Dioxide - Material for a Sustainable Environment*, 2018.

182. Wang, Y.; Wang, Q.; Zhan, X.; Wang, F.; Safdar, M.; He, J. Visible Light Driven Type II Heterostructures and Their Enhanced Photocatalysis Properties: A Review. *Nanoscale* 2013, 5 (18), 8326-8339.

183. Jiang, W.; Qu, D.; An, L.; Gao, X.; Wen, Y.; Wang, X.; Sun, Z. Deliberate Construction of Direct Z-Scheme Photocatalysts through Photodeposition. *J. Mater. Chem. A* 2019, 7 (31), 18348-18356.

184. Zhang, J.; Hu, Y.; Jiang, X.; Chen, S.; Meng, S.; Fu, X. Design of a Direct Z-Scheme Photocatalyst: Preparation and Characterization of Bi_2O_3/g-C_3N_4 with High Visible Light Activity. *J. Hazard. Mater.* 2014, 280C, 713-722.

185. Xu, Q.; Zhang, L.; Yu, J.; Wageh, S.; Al-Ghamdi, A. A.; Jaroniec, M. Direct Z-Scheme Photocatalysts: Principles, Synthesis, and Applications. *Mater. Today* 2018, 21 (10), 1042-1063.

186. Low, J.; Jiang, C.; Cheng, B.; Wageh, S.; Al-Ghamdi, A. A.; Yu, J. A Review of Direct Z-Scheme Photocatalysts. *Small Methods* 2017, 1 (5), 1700080.

187. Ren, Y.; Zeng, D.; Ong, W.-J. Interfacial Engineering of Graphitic Carbon Nitride (g-C_3N_4)-Based Metal Sulfide Heterojunction Photocatalysts for Energy Conversion: A Review. *Chinese J. Catal.* 2019, 40 (3), 289-319.

188. Qin, Y.; Lu, J.; Meng, F.; Lin, X.; Feng, Y.; Yan, Y.; Meng, M. Rationally Constructing of a Novel 2D/2D WO_3/Pt/g-C_3N_4 Schottky-Ohmic Junction towards Efficient Visible-Light-Driven Photocatalytic Hydrogen Evolution and Mechanism Insight. *J. Colloid Interface Sci.* 2021, 586, 576-587.

189. Jing, L.; Xu, Y.; Chen, Z.; He, M.; Xie, M.; Liu, J.; Xu, H.; Huang, S.; Li, H. Different Morphologies of SnS_2 Supported on 2D g-C_3N_4 for Excellent and Stable Visible Light Photocatalytic Hydrogen Generation. *ACS Sustain. Chem. Eng.* 2018, 6 (4), 5132-5141.

190. Dong, F.; Ni, Z.; Li, P.; Wu, Z. A General Method for Type I and Type II g-C_3N_4/g-C_3N_4 Metal-Free Isotype Heterostructures with Enhanced Visible Light Photocatalysis. *New J. Chem.* 2015, 39 (6), 4737-4744.

191. Rapti, I.; Bairamis, F.; Konstantinou, I. g-C_3N_4/MoS_2 Heterojunction for Photocatalytic Removal of Phenol and Cr(VI). *Photochem* 2021, 1 (3), 358-370.

192. Kalidasan, K.; Mallapur, S.; Vishwa, P.; Kandaiah, S. Type II NdWO_3/g-C_3N_4 n–n Heterojunction for Visible-Light-Driven Photocatalyst: Exploration of Charge Transfer in Nd^{3+} Ion-Doped WO_3/g-C_3N_4 Composite. *Ind. Eng. Chem. Res.* 2022, 61 (45), 16673-16688.

193. Liang, M.; Borjigin, T.; Zhang, Y.; Liu, B.; Liu, H.; Guo, H. Controlled Assemble of Hollow Heterostructured g-C_3N_4@CeO_2 with Rich Oxygen Vacancies for Enhanced Photocatalytic CO_2 Reduction. *Appl. Catal. B: Environ.* 2019, 243, 566-575.

194. Ng, B.-J.; Tang, J.-Y.; Ow, L. Y.; Kong, X. Y.; Ng, Y. H.; Putri, L. K.; Chai, S.-P. Nanoscale p–n Junction Integration via the Synergetic Hybridization of Facet-Controlled Cu_2O and Defect-Modulated g-C_3N_{4-x} Atomic Layers for Enhanced Photocatalytic Water Splitting. *Mater. Today Energy* 2022, 29, 101102.

195. Liu, H.; Zhu, X.; Han, R.; Dai, Y.; Sun, Y.; Lin, Y.; Gao, D.; Wang, X.; Luo, C. Study on the Internal Electric Field in the Cu_2O/g-C_3N_4 p–n Heterojunction Structure for Enhancing Visible Light Photocatalytic Activity. *New J. Chem.* 2020, 44 (5), 1795-1805.

196. Jourshabani, M.; Shariatinia, Z.; Achari, G.; Langford, C. H.; Badiei, A. Facile Synthesis of NiS_2 Nanoparticles Ingrained in a Sulfur-Doped Carbon Nitride Framework with Enhanced Visible Light Photocatalytic Activity: Two Functional Roles of Thiourea. *J. Mater. Chem. A* 2018, 6 (27), 13448-13466.

197. Zhuang, Z.; Li, Y.; Li, Z.; Lv, F.; Lang, Z.; Zhao, K.; Zhou, L.; Moskaleva, L.; Guo, S.; Mai, L. MoB/g-C_3N_4 Interface Materials as a Schottky Catalyst to Boost Hydrogen Evolution. *Angew. Chem. Int. Ed.* 2018, 57 (2), 496-500.

198. Ma, X.; Fu, Z.; Wang, C.; Hu, X.; Fan, J.; Tang, C.; Liu, E. Facile Strategy to Construction Co_2P/g-C_3N_4 Heterojunction with Excellent Photocatalytic Water Splitting Activity. *Mater. Lett.* 2021, 284, 128964.

199. Ma, X.; Ma, Z.; Zhang, H.; Lu, D.; Duan, J.; Hou, B. Interfacial Schottky Junction of $Ti_3C_2T_x$ MXene/g-C_3N_4 for Promoting Spatial Charge Separation in Photoelectrochemical Cathodic Protection of Steel. *J. Photochem. Photobiol. A: Chem.* 2022, 426, 113772.

200. Liu, W.; Sun, M.; Ding, Z.; Gao, B.; Ding, W. Ti_3C_2 MXene Embellished g-C_3N_4 Nanosheets for Improving Photocatalytic Redox Capacity. *J. Alloys Compd.* 2021, 877, 160223.

201. Yang, Y.; Zeng, Z.; Zeng, G.; Huang, D.; Xiao, R.; Zhang, C.; Zhou, C.; Xiong, W.; Wang, W.; Cheng, M.; et al. Ti_3C_2 Mxene/Porous g-C_3N_4 Interfacial Schottky Junction for Boosting Spatial Charge Separation in Photocatalytic H_2O_2 Production. *Appl. Catal. B: Environ.* 2019, 258, 117956.

202. Sun, Y.; Jin, D.; Sun, Y.; Meng, X.; Gao, Y.; Dall'Agnese, Y.; Chen, G.; Wang, X.-F. g-C_3N_4/$Ti_3C_2T_x$ (MXenes) Composite with Oxidized Surface Groups for Efficient Photocatalytic Hydrogen Evolution. *J. Mater. Chem. A* 2018, 6 (19), 9124-9131.

203. Ran, J.; Gao, G.; Li, F.-T.; Ma, T.-Y.; Du, A.; Qiao, S.-Z. Ti_3C_2 MXene co-Catalyst on Metal Sulfide Photo-Absorbers for Enhanced Visible-Light Photocatalytic Hydrogen Production. *Nat. Commun.* 2017, 8 (1), 13907.

204. Zeng, D.; Ong, W.-J.; Zheng, H.; Wu, M.; Chen, Y.; Peng, D.-L.; Han, M.-Y. $Ni_{12}P_5$ Nanoparticles Embedded into Porous g-C_3N_4 Nanosheets as a Noble-Metal-Free Hetero-

Structure Photocatalyst for Efficient H_2 Production under Visible Light. *J. Mater. Chem. A* 2017, 5 (31), 16171-16178.

205. Zeng, D.; Xu, W.; Ong, W.-J.; Xu, J.; Ren, H.; Chen, Y.; Zheng, H.; Peng, D.-L. Toward Noble-Metal-Free Visible-Light-Driven Photocatalytic Hydrogen Evolution: Monodisperse Sub–15nm Ni_2P Nanoparticles Anchored on Porous g-C_3N_4 Nanosheets to Engineer 0D-2D Heterojunction Interfaces. *Appl. Catal. B: Environ.* 2018, 221, 47-55.

206. Ye, R.; Fang, H.; Zheng, Y.-Z.; Li, N.; Wang, Y.; Tao, X. Fabrication of $CoTiO_3$/g-C_3N_4 Hybrid Photocatalysts with Enhanced H_2 Evolution: Z-Scheme Photocatalytic Mechanism Insight. *ACS Appl. Mater. Interfaces* 2016, 8 (22), 13879-13889.

207. Li, X.; Yu, J.; Jaroniec, M. Hierarchical Photocatalysts. *Chem. Soc. Rev.* 2016, 45 (9), 2603-2636.

208. Xu, Q.; Zhang, L.; Cheng, B.; Fan, J.; Yu, J. S-Scheme Heterojunction Photocatalyst. *Chem* 2020, 6 (7), 1543-1559.

209. Zhang, L.; Zhang, J.; Yu, H.; Yu, J. Emerging S-Scheme Photocatalyst. *Adv. Mater.* 2022, 34 (11), 2107668.

210. Qi, K.; Cheng, B.; Yu, J.; Ho, W. A Review on TiO_2-Based Z-Scheme Photocatalysts. *Chinese J. Catal.* 2017, 38 (12), 1936-1955.

211. Zhang, M.; Yin, H.-f.; Yao, J.-c.; Arif, M.; Qiu, B.; Li, P.-f.; Liu, X.-h. All-Solid-State Z-Scheme BiOX(Cl, Br)-Au-CdS Heterostructure: Photocatalytic Activity and Degradation Pathway. *Colloids Surf. A: Physicochem. Eng. Asp.* 2020, 602, 124778.

212. Wu, J.; Shen, X.; Miao, X.; Ji, Z.; Wang, J.; Wang, T.; Liu, M. An All-Solid-State Z-Scheme g-C_3N_4/Ag/Ag_3VO_4 Photocatalyst with Enhanced Visible-Light Photocatalytic Performance. *Eur. J. Inorg. Chem.* 2017, 2017 (21), 2845-2853.

213. Isimjan, T. T.; Maity, P.; Llorca, J.; Ahmed, T.; Parida, M. R.; Mohammed, O. F.; Idriss, H. Comprehensive Study of All-Solid-State Z-Scheme Photocatalytic Systems of ZnO/Pt/CdZnS. *ACS Omega* 2017, 2 (8), 4828-4837.

214. Li, N.; Fan, G.; Fan, M.; Wu, F.; Zhang, G.; Fan, D. All-Solid-State Z-Scheme Ag_3PO_4/CSs/AgBr Heterostructures for Efficient Visible-Light Photocatalysis and the Photocatalytic Mechanism. *Dalton Trans.* 2021, 50 (43), 15602-15611.

215. Fernández-Catalá, J.; Greco, R.; Navlani-García, M.; Cao, W.; Berenguer-Murcia, Á.; Cazorla-Amorós, D. g-C_3N_4-Based Direct Z-Scheme Photocatalysts for Environmental Applications. *Catalysts* 2022, 12 (10), 1137.

216. Fu, J.; Xu, Q.; Low, J.; Jiang, C.; Yu, J. Ultrathin 2D/2D WO_3/g-C_3N_4 Step-Scheme H_2-Production Photocatalyst. *Appl. Catal. B: Environ.* 2019, 243, 556-565.

217. Xu, F.; Meng, K.; Cheng, B.; Wang, S.; Xu, J.; Yu, J. Unique S-Scheme Heterojunctions in Self-Assembled TiO_2/$CsPbBr_3$ Hybrids for CO_2 Photoreduction. *Nat. Commun.* 2020, 11 (1), 4613.

218. Kisch, H.; Bahnemann, D. Best Practice in Photocatalysis: Comparing Rates or Apparent Quantum Yields? *J. Phys. Chem. Lett.* 2015, 6 (10), 1907-1910.

219. Pham, M.-T.; Nguyen, T.-M. T.; Bui, D.-P.; Wang, Y.-F.; Tran, H.-H.; You, S.-J. Enhancing Quantum Efficiency at Ag/g-C_3N_4 Interfaces for Rapid Removal of Nitric Oxide under Visible Light. *Sustain. Chem. Pharm.* 2022, 25, 100596.

220. Hassan, A. E.; Elsayed, M. H.; Hussien, M. S. A.; Mohamed, M. G.; Kuo, S.-W.; Chou, H.-H.; Yahia, I. S.; Mohamed, T. A.; Wen, Z. V_2O_5 Nanoribbons/N-Deficient g-C_3N_4 Heterostructure for Enhanced Visible-Light Photocatalytic Performance. *Int. J. Hydrog. Energy* 2023, 48 (26), 9620-9635.

221. Van Viet, P.; Nguyen, H.-P.; Tran, H.-H.; Bui, D.-P.; Hai, L. V.; Pham, M.-T.; You, S.-J.; Thi, C. M. Constructing g-C_3N_4/SnO_2 S-Scheme Heterojunctions for Efficient

Photocatalytic NO Removal and Low NO_2 Generation. *J. Sci.: Adv. Mater. Devices* 2021, 6 (4), 551-559.

222. Li, Y.; Ding, L.; Guo, Y.; Liang, Z.; Cui, H.; Tian, J. Boosting the Photocatalytic Ability of g-C_3N_4 for Hydrogen Production by Ti_3C_2 MXene Quantum Dots. *ACS Appl. Mater. Interfaces* 2019, 11 (44), 41440-41447.

223. Xu, Z.; Zhong, J.; Chen, J.; Li, M.; Zeng, L.; Yang, H. Construction of S-scheme Co_3O_4/g-C_3N_4 Heterojunctions with Boosted Photocatalytic H_2 Production Performance. *Surf. Interfaces* 2023, 38, 102838.

224. Humayun, M.; Fu, Q.; Zheng, Z.; Li, H.; Luo, W. Improved Visible-Light Catalytic Activities of Novel Au/P-Doped g-C_3N_4 Photocatalyst for Solar Fuel Production and Mechanism. *Appl. Catal. A: Gen.* 2018, 568, 139-147.

225. Wang, F.; Hu, J.; Liang, R.; Lei, W.; Lou, Z.; Pan, X.; Lu, B.; Ye, Z. Novel ReS_2/g-C_3N_4 Heterojunction Photocatalyst Formed by Electrostatic Self-Assembly with Increased H_2 Production. *Int. J. Hydrog. Energy* 2022, 47 (68), 29284-29294.

226. Wang, Y.; Zu, M.; Zhou, X.; Lin, H.; Peng, F.; Zhang, S. Designing Efficient TiO_2-Based Photoelectrocatalysis Systems for Chemical Engineering and Sensing. *Chem. Eng. J.* 2020, 381, 122605.

227. Navidpour, A. H.; Hosseinzadeh, A.; Zhou, J. L.; Huang, Z. Progress in the Application of Surface Engineering Methods in Immobilizing TiO_2 and ZnO Coatings for Environmental Photocatalysis. *Catal. Rev.* 2021, 1-52.

228. Zhang, Z.; Lin, S.; Li, X.; Li, H.; Cui, W. Metal Free and Efficient Photoelectrocatalytic Removal of Organic Contaminants over g-C_3N_4 Nanosheet Films Decorated with Carbon Quantum Dots. *RSC Adv.* 2017, 7 (89), 56335-56343.

229. Tang, H.; Shang, Q.; Tang, Y.; Yi, X.; Wei, Y.; Yin, K.; Liu, M.; Liu, C. Static and Continuous Flow Photoelectrocatalytic Treatment of Antibiotic Wastewater over Mesh of TiO_2 Nanotubes Implanted with g-C_3N_4 Nanosheets. *J. Hazard. Mater.* 2020, 384, 121248.

230. Zhang, L.; Zhang, X.; Wei, C.; Wang, F.; Wang, H.; Bian, Z. Interface Engineering of Z-Scheme α-Fe_2O_3/g-C_3N_4 Photoanode: Simultaneous Enhancement of Charge Separation and Hole Transportation for Photoelectrocatalytic Organic Pollutant Degradation. *Chem. Eng. J.* 2022, 435, 134873.

231. Li, S.; Zhang, Y.; Huang, H. Black Phosphorus-Based Heterostructures for Photocatalysis and Photoelectrochemical Water Splitting. *J. Energy Chem.* 2022, 67, 745-779.

232. Al-Attafi, K.; Nattestad, A.; Qutaish, H.; Park, M.-S.; Shrestha, L. K.; Ariga, K.; Dou, S. X.; Ho Kim, J. Solvothermally Synthesized Anatase TiO_2 Nanoparticles for Photoanodes in Dye-Sensitized Solar Cells. *Sci. Technol. Adv. Mater.* 2021, 22 (1), 100-112.

233. Xie, J.; Wen, W.; Jin, Q.; Xiang, X.-B.; Wu, J.-M. TiO_2 Nanotrees for the Photocatalytic and Photoelectrocatalytic Phenol Degradation. *New J. Chem.* 2019, 43 (28), 11050-11056.

234. Hou, Y.; Li, X.-Y.; Zhao, Q.-D.; Quan, X.; Chen, G.-H. Electrochemical Method for Synthesis of a $ZnFe_2O_4$/TiO_2 Composite Nanotube Array Modified Electrode with Enhanced Photoelectrochemical Activity. *Adv. Funct. Mater.* 2010, 20 (13), 2165-2174.

235. Reis, R. Y. N.; Lima, A. E. B.; Costa, M. J. S.; Cruz-Filho, J. F.; Moura, J. P. C.; Santos, R. S.; Luz, G. E. Enhanced Photoelectrocatalytic Performance of ZnO Films Doped with N_2 by a Facile Electrochemical Method. *Surf. Interfaces* 2020, 21, 100675.

236. Orimolade, B. O.; Arotiba, O. A. Towards Visible Light Driven Photoelectrocatalysis for Water Treatment: Application of a FTO/$BiVO_4$/Ag_2S Heterojunction Anode for the Removal of Emerging Pharmaceutical Pollutants. *Sci. Rep.* 2020, 10 (1), 5348.

237. Jia, L.; Sun, X.; Jiang, Y.; Yu, S.; Wang, C. A Novel $MoSe_2$–Reduced Graphene Oxide/Polyimide Composite Film for Applications in Electrocatalysis and Photoelectrocatalysis Hydrogen Evolution. *Adv. Funct. Mater.* 2015, 25 (12), 1814-1820.

238. Liu, X.; Min, L.; Yu, X.; Zhou, Z.; Sha, L.; Zhang, S. Changes of Photoelectrocatalytic, Electrocatalytic and Pollutant Degradation Properties During the Growth of β-PbO_2 into Black Titanium Oxide Nanoarrays. *Chem. Eng. J.* 2021, 417, 127996.

239. Orimolade, B. O.; Koiki, B. A.; Zwane, B. N.; Peleyeju, G. M.; Mabuba, N.; Arotiba, O. A. Interrogating Solar Photoelectrocatalysis on an Exfoliated Graphite–$BiVO_4$/ZnO Composite Electrode towards Water Treatment. *RSC Adv.* 2019, 9 (29), 16586-16595.

240. Sun, J.; Guo, Y.; Wang, Y.; Cao, D.; Tian, S.; Xiao, K.; Mao, R.; Zhao, X. H_2O_2 Assisted Photoelectrocatalytic Degradation of Diclofenac Sodium at g-C_3N_4/$BiVO_4$ Photoanode under Visible Light Irradiation. *Chem. Eng. J.* 2018, 332, 312-320.

241. Huo, Y.; Zhang, L.; Wang, S.; Wang, X. Polyoxometalate@g-C_3N_4 Nanocomposite for Enhancing Visible Light Photoelectrocatalytic Performance. *Chemosphere* 2021, 279, 130559.

242. Zhang, L.; Wei, C.; Tang, H.; Wang, H.; Bian, Z. Construction of Heterojunction Photoanode via Facile Synthesis of CoOx/CN Nanocomposites for Enhanced Visible-Light-Driven Photoelectrochemical Degradation of Clofibric Acid. *Chemosphere* 2021, 281, 130825.

243. Li, W.; Lyu, J.; Zhou, K.; Ma, H.; Ma, C.; Dong, X.; Fu, Y. Fabrication and Photoelectrocatalytic Performance of C_3N_4-Modified Ti/PbO_2 Anode with Surface Hydrophobicity. *J. Solid State Electrochem.* 2020, 24 (7), 1577-1585.

244. Wang, H.; Liang, Y.; Liu, L.; Hu, J.; Cui, W. Highly Ordered TiO_2 Nanotube Arrays Wrapped with g-C_3N_4 Nanoparticles for Efficient Charge Separation and Increased Photoelectrocatalytic Degradation of Phenol. *J. Hazard. Mater.* 2018, 344, 369-380.

245. Su, Y.; Liu, G.; Zeng, C.; Lu, Y.; Luo, H.; Zhang, R. Carbon Quantum Dots-Decorated TiO_2/g-C_3N_4 Film Electrode as a Photoanode with Improved Photoelectrocatalytic Performance for 1,4-Dioxane Degradation. *Chemosphere* 2020, 251, 126381.

246. Xian, T.; Sun, X.; Di, L.; Zhou, Y.; Ma, J.; Li, H.; Yang, H. Carbon Quantum Dots (CQDs) Decorated Bi_2O_{3-x} Hybrid Photocatalysts with Promising NIR-Light-Driven Photodegradation Activity for AO7. *Catalysts* 2019, 9 (12), 1031.

247. Amiri, R.; Rezaei, A.; Fattahi, N.; Pirsaheb, M.; Rodríguez-Chueca, J.; Moradi, M. Carbon Quantum Dots Decorated Ag/$CuFe_2O_4$ for Persulfate-Assisted Visible Light Photocatalytic Degradation of Tetracycline: A Comparative Study. *J. Water Process Eng.* 2022, 47, 102742.

248. Balakumar, V.; Ramalingam, M.; Sekar, K.; Chuaicham, C.; Sasaki, K. Fabrication and Characterization of Carbon Quantum Dots Decorated Hollow Porous Graphitic Carbon Nitride through Polyaniline for Photocatalysis. *Chem. Eng. J.* 2021, 426, 131739.